NEXT GENERATION OF MULTIFUNCTIONAL SCANNING PROBES

A Thesis
Presented to
The Academic Faculty

By

JONG SEOK MOON

In Partial Fulfillment
of the Requirements for the Degree
Doctor of Philosophy in Chemistry

Georgia Institute of Technology
December 2010

NEXT GENERATION OF MULTIFUNCTIONAL SCANNING PROBES

Approved by:

Dr. Boris Mizaikoff, Advisor
School of Chemistry and Biochemistry
Georgia Institute of Technology

Dr. Christine Kranz, Co-advisor
School of Chemistry and Biochemistry
Georgia Institute of Technology

Dr. Facundo M. Fernandez, Co-advisor
School of Chemistry and Biochemistry
Georgia Institute of Technology

Dr. Thomas Orlando
School of Chemistry and Biochemistry
Georgia Institute of Technology

Dr. Peter J. Hesketh
School of Mechanical Engineering
Georgia Institute of Technology

Dr. Dennis W. Hess
School of Chemical & Biomolecular Engineering
Georgia Institute of Technology

Date Approved: November 5, 2010

ACKNOWLEDGEMENTS

I would like to thank my research advisor Dr. Boris Mizaikoff and Dr. Christine Kranz for giving me the opportunity to work with them, and providing me research guidance. I could not even think of starting a PhD course and finalize the course without their endless support and their encouragements. Dr. Facundo Fernandez, Dr. Thomas Orlando, Dr. Peter Hesketh and Dr. Dennis Hess are gratefully appreciated for serving as committee members and for precious scientific advice.

I also would like to thank the former members of the Applied Sensors Laboratory for their help and support throughout the course of my thesis. A special thanks goes to Dr. Heungjoo Shin and Dr. Justyna Wiedemair for their encouragement and discussions throughout the work. Also I would like to thank Dr. Yeonho Jung, Dr. Jinwoo Park and other Georgia Tech MiRC cleanroom users and staff for their advice and assistance. Moreover I would like to thank my collaborators Dr. Balamurali Balu from the School of Chemical and Biomolecular Engineering, Dr. Janusz Kowalik from the School of Chemistry and Biochemistry, Owen Hildreth from the School of Materials Science & Engineering. I am also grateful for financial support from the National Institute of Health (NIH).

At last, special thanks go to my parents and my wife. I heartily appreciate their support, encouragement and patience.

TABLE OF CONTENTS

LIST OF TABLES

LIST OF FIGURES

LIST OF ABBREVIATIONS

AFM	Atomic force microscopy/microscope
AFM-SECM	Atomic force microscopy-scanning electrochemical microscopy
AgQRE	Silver quasi reference electrode
AIROF	Anodic iridium oxide film
CE	Counter electrode
CV	Cyclic voltammetry
DC	Direct current
EIS	Electrochemical impedance spectroscopy
FIB	Focused ion beam
GC	Generation collection
ICP	Inductively coupled plasma
IROF	Iridium oxide films
ISE	Ion-selective electrodes
ISFET	Ion-sensitive field effect transistors
LPCVD	Low-pressure chemical vapor deposition
MEMS	Microelectromechanical systems
MOSFET	Metal-oxide-semiconductor field-effect transistor
NSOM	Near field scanning optical microscopy/microscope
OCP	Open circuit potential
PFE	Pentafluoroethane (CF_3CHF_2)
PECVD	Plasma-enhanced chemical vapor deposition
RE	Reference electrode
RF	Radio frequency

RIE	Reactive ion etching
SCE	Saturated calomel electrode
SECM	Scanning electrochemical microscopy/microscope
SEM	Scanning electron microscopy/microscope
SG/TC	Sample generation/tip collection
SIROF	Sputtered iridium oxide film
SPM	Scanning probe microscopy
STM	Scanning tunneling microscopy/microscope
TG/SC	Tip generation/sample collection
UME	Ultramicroelectrodes
WE	Working electrode

SUMMARY

The goal of this thesis was the advanced design, fabrication, and application of combined atomic force microscopy - scanning electrochemical microscopy (AFM-SECM) probes for high-resolution topographical and electrochemical imaging.

The first part of the thesis describes innovative approaches for the optimization of AFM-SECM probe fabrication with recessed frame electrodes. For this purpose, commercial silicon nitride AFM cantilevers were modified using optimized critical fabrication processes including improved metallization for the deposition of the electrode layer, and novel insulation strategies for ensuring localized electrochemical signals. As a novel approach for the insulation of AFM-SECM probes, sandwiched layers of PECVD Si_xN_y and SiO_2, and plasma-deposited PFE films were applied and tested. Using sandwiched PECVD Si_xN_y and SiO_2 layers, AFM-SECM probes providing straight (unbent) cantilevers along with excellent insulation characteristics facilitating the functionality of the integrated electrode were reproducibly obtained. Alternatively, PFE thin films were tested according to their utility for serving as a mechanically flexible insulating layer for AFM-SECM probes. The electrochemical characterization of PFE-insulated AFM-SECM probes revealed excellent insulating properties at an insulation thickness of only approx. 400 nm. Finally, AFM-SECM cantilevers prepared via both insulation strategies were successfully tested during AFM-SECM imaging experiments.

In the second part of this thesis, disk-shaped nanoelectrodes were for the first time integrated into AFM probes for enabling high-resolution AFM-SECM measurements. Disk electrodes with an electrode radius < 100 nm were realized, which provides a

significantly improved lateral resolution for SECM experiments performed in synchronicity with AFM imaging. Furthermore, the developed fabrication scheme enables producing AFM-SECM probes with integrated disk nanoelectrodes at significantly reduced time and cost based on a highly reproducible semi-batch fabrication process providing bifunctional probes at a wafer scale. The development of a detailed processing strategy was accompanied by extensive simulation results for developing a fundamental understanding on the electrochemical properties of AFM-SECM probes with nanoscale electrodes, and for optimizing the associated processing parameters. Thus fabricated probes were electrochemically characterized, and their performance was demonstrated via bifunctional imaging at model samples.

The third part of this thesis describes the development and characterization of the first AFM tip-integrated potentiometric sensors based on solid-state electrodes with sub-micrometer dimensions enabling laterally resolved pH imaging. Antimony and iridium oxides were applied as the pH sensitive electrode material, and have been integrated into the AFM probes via conventional microfabrication strategies. The pH response of such AFM tip-integrated integrated pH microsensors was tested for both material systems, and first studies were performed demonstrating localized pH measurements at a model system.

1 Introduction

1.1 Thesis objective

The objective of this thesis was the advanced design, fabrication and application of combined atomic force microscopy-scanning electrochemical microscopy (AFM-SECM) probes. The advancement was implemented by improving the current AFM-SECM probes characteristics, improving the achievable electrochemical resolution in imaging and integrating potentiometric sensing into AFM-SECM probes.

1.2 Original contributions of this thesis

Improvement of conventional AFM-SECM probes fabrication (chapter 3)

- Optimization of insulating AFM-SECM probes. First application of PFE layers as insulation material for AFM-SECM probes.

Integration of disk nanoelectrodes (chapter 4)

- Development of a semi-batch fabrication process for tip-integrated disk nanoelectrodes enabling high resolution AFM-SECM imaging.

AFM tip-integrated potentiometric sensors (pH sub-microelectrode) (chapter 5)

- Establishing the fabrication process for tip-integrated solid-state pH sensors and the first application of combined AFM-SECM probe for localized pH measurements.

1.3 Motivation

Since the introduction of AFM in 1986[1], it has emerged as one of the most popular scanning probe technique applied in almost any area ranging from UHV application[2] providing atomic resolution to routine measurements in material science[3-4] and study biological entities in physiological conditions[5]. Despite its versatility, the chemical information achieved by AFM without any modification of the AFM probe is limited. In contrast, scanning electrochemical microscopy (SECM) enables the performance of microelectrochemical experiments, in which the analytic response is influenced by the morphology and electrochemical reactivity of the investigated sample surface. Although, nanoelectrodes can be fabricated and have been introduced almost 30 years ago[6-7], their use in SECM experiment scanning across the sample surface is still not reported on a routine basis[8-9]. One of the significant efforts to improve the lateral resolution achievable in SECM is introducing shear force-based constant distance SECM imaging[10-14]. However, it cannot compete in resolution with other scanning probe techniques as the topographical resolution is dependent on the size of the electrode. The size determines the absolute distance of the electrode to the sample surface and is afflicted with some uncertainty, which has to be taken into account when quantification of measured species in a SECM experiment is required.

Adding functionality in order to achieve complementary information has been shown for several hyphenated scanning probe techniques[15-19]. From the standpoint of microelectrochemical characterization, the combination of AFM-SECM utilizing integrated electrodes allows positioning of a small electroactive area close to the sample surface and for the presented probe design following the sample topography while

keeping a controlled distance between the electrode and the sample surface. Based on several approaches, which have been published over the last 10 years, the geometry of the proposed AFM-SECM probes can be categorized into two types, depending on where the electrode is defined at the AFM tip.

One approach is based on defining an electrode at the apex of the AFM tip[20-24]. This technique was first described by Macpherson and Unwin using flattened and etched Pt microwires, which were subsequently insulated exposing a conical sub-microelectrode[23]. This type of approaches enables high resolution electrochemical imaging with small conical electrodes, but this advantage is often damped with the disadvantage of sequential measurements of topography and electrochemistry.

The second approach is focused on defining the electroactive area recessed at a certain distance from the apex of the tip[25-31]. This type of approaches typically prevents abrasion of softer electrode material and contamination by the sample surface. Also, this does not require that topographical and electrochemical data are recorded in a sequential mode. However, up to now these advantages are correlated with the disadvantage of micrometer-sized electrodes.

In addition, batch fabrication approaches, which are aiming on significantly reduced time and cost for the fabrication of AFM-SECM probes have been reported[22,32-36]. Some of these approaches are in the first category in which electrodes are defined at the apex of the AFM. However, all these approaches often require sequential measurements of topography and electrochemistry as described previously. Other batch fabrication approaches are in the second category in which the electrode is recessed at certain distance from the apex of the tip. Shin et al. reported batch-fabricated platinum ring

electrodes integrated AFM probes[35-36]. The ring-shaped electrodes were recessed from apex of the tip without any FIB milling process. However, the size of the electrode was limited to micrometer size due to center-located AFM tip.

Successfully integrating a disk nanoelectrode deliberately recessed from the apex of an AFM tip will enhance the research field of combined scanning probe techniques and provide a lateral resolution of the combined complementary techniques, which is in the same dimension. The present thesis focuses on a semi wafer-level batch fabrication scheme for integrated disk nanoelectrodes with less than 100nm radius. In addition, the developed process allows a well defined electrode by defining the size of the electrode by a FIB milling step during the batch process. This is expected to be an important step towards doing fundamental studies at a microscopic to nanoscopic scale in many research areas. As an example, studies on corroding surfaces strongly demand the electrochemical imaging at a nanoscale of spatial resolution. Although the macroscopic corrosion behaviors have been widely studied using electrochemical impedance spectroscopy (EIS)[37], such macroscopic studies are intrinsically limited to the final stage of corrosion activity and it is known that the initial stage includes critical information on corrosion initiation mechanisms[38-39]. Extremely localized pitting corrosion driven by the depassivation of small area in aggressive environment is regarded as a major cause of surface degradation of passivated metal; hence nanometer scale of study is required to understand the mechanisms of initiation[40]. The initiation of pitting can be caused by a small defect in the surface and less than a few tens of nanometers of crystalline defects at a passivated metal surface play a key role in the dissolution[41-42]. Therefore, developing a probing electrode with comparable size to the features (nanometer scale) is essential and

will provide knowledge on corrosion initiation mechanisms at nanometer scale for better understanding the phenomena and improving stability of materials.

1.4 Structure of this thesis

The thesis is structured as follows:

Chapter 2 describes background of electrochemical techniques and scanning probe techniques relevant to the research presented in this thesis. In particular scanning electrochemical microscopy and atomic force microscopy are highlighted.

Chapter 3 describes efforts to improve AFM-SECM probes fabrication by establishing efficient, reproducible and performance optimization procedures.

Chapter 4 focuses on the development of a semi-batch fabrication process for reliable fabrication of disk nanoelectrodes integrated in atomic force microscopy (AFM) probes, which provide improved lateral electrochemical information for combined AFM-SECM measurements.

Chapter 5 introduces AFM tip-integrated potentiometric sensors based on sub-micro solid-state electrodes. Antimony/antimony oxides and iridium /iridium oxides were used as pH sensitive electrodes, which can be integrated in AFM probes by standard cleanroom processes. The fabricated sensors were thoroughly characterized.

Chapter 6 includes concluding remarks and an outlook.

1.5 References

1. G. Binnig, C. F. Quate, C. Gerber, Atomic Force Microscope. *Physical Review Letters* 1986, *56*. 930.

2. F. J. Giessibl, Atomic Resolution of the Silicon (111)-(7×7) Surface by Atomic Force Microscopy. *Science* 1995, *267*. 68-71.

3. T. R. Albrecht, C. F. Quate, Atomic resolution imaging of a nonconductor by atomic force microscopy. *Journal of Applied Physics* 1987, *62*. 2599-2602.

4. P. K. Hansma, V. B. Elings, O. Marti, C. E. Bracker, Scanning Tunneling Microscopy and Atomic Force Microscopy: Application to Biology and Technology. *Science* 1988, *242*. 209-216.

5. H. G. Hansma, Surface Biology of DNA by Atomic Force Microscopy. *Annual Review of Physical Chemistry* 2001, *52*. 71.

6. R. B. Morris, D. J. Franta, H. S. White, Electrochemistry at platinum bane electrodes of width approaching molecular dimensions: breakdown of transport equations at very small electrodes. *The Journal of Physical Chemistry* 1987, *91*. 3559-3564.

7. J. D. Seibold, E. R. Scott, H. S. White, Diffusional transport to nanoscopic band electrodes. *Journal of Electroanalytical Chemistry* 1989, *264*. 281-289.

8. X. Li, Q. Geng, Y. Wang, Z. Si, W. Jiang, X. Zhang, W. Jin, Micropatterning of active enzyme with a high-resolution by scanning electrochemical microscopy coupled with a nanometer-sized carbon fiber disk tip. *Electrochimica Acta* 2007, *53*. 2016-2024.

9. M. A. Mezour, R. Cornut, E. M. Hussien, M. Morin, J. Mauzeroll, Detection of Hydrogen Peroxide Produced during the Oxygen Reduction Reaction at Self-Assembled Thiol−Porphyrin Monolayers on Gold using SECM and Nanoelectrodes. *Langmuir* 2010, *26*. 13000-13006.

10. A. Hengstenberg, C. Kranz, W. Schuhmann, Facilitated Tip-Positioning and Applications of Non-Electrode Tips in Scanning Electrochemical Microscopy Using a Shear Force Based Constant-Distance Mode. *Chemistry – A European Journal* 2000, *6*. 1547-1554.

11. P. I. James, L. F. Garfias-Mesias, P. J. Moyer, W. H. Smyrl, Scanning Electrochemical Microscopy with Simultaneous Independent Topography. *Journal of The Electrochemical Society* 1998, *145*. L64-L66.

12. B. B. Katemann, A. Schulte, W. Schuhmann, Constant-distance mode scanning electrochemical microscopy (SECM)-part 1: Adaptation of a non-optical shear-force-

based positioning mode for SECM tips. *chemistry a european journal* 2003, *9*. 2025-2033.

13. M. Ludwig, C. Kranz, W. Schuhmann, H. E. Gaub, Topography feedback mechanism for the scanning electrochemical microscope based on hydrodynamic forces between tip and sample. *Review of Scientific Instruments* 1995, *66*. 2857-2860.

14. D. Oyamatsu, Y. Hirano, N. Kanaya, Y. Mase, M. Nishizawa, T. Matsue, Imaging of enzyme activity by scanning electrochemical microscope equipped with a feedback control for substrate-probe distance. *Bioelectrochemistry* 2003, *60*. 115-121.

15. B. J. Albers, M. Liebmann, T. C. Schwendemann, M. Z. Baykara, M. Heyde, M. Salmeron, E. I. Altman, U. D. Schwarz, Combined low-temperature scanning tunneling/atomic force microscope for atomic resolution imaging and site-specific force spectroscopy. *Review of Scientific Instruments* 2008, *79*. 033704.

16. J. W. Bender, M. E. Salmon, P. E. Russell, Combined atomic force microscopy and scanning tunneling microscopy imaging of cross-sectioned GaN light-emitting diodes. *Scanning* 2003, *25*. 45-51.

17. M. Fujihira, H. Monobe, N. Yamamoto, H. Muramatsu, N. Chiba, K. Nakajima, T. Ataka, Scanning near-field optical microscopy of fluorescent polystyrene spheres with a combined SNOM and AFM. *Ultramicroscopy* 1995, *61*. 271-277.

18. M. Micic, K. Radotic, M. Jeremic, D. Djikanovic, S. B. Kämmer, Study of the lignin model compound supramolecular structure by combination of near-field scanning optical microscopy and atomic force microscopy. *Colloids and Surfaces B: Biointerfaces* 2004, *34*. 33-40.

19. M. Stopka, D. Drews, K. Mayr, M. Lacher, W. Ehrfeld, T. Kalkbrenner, M. Graf, V. Sandoghdar, J. Mlynek, Multifunctional AFM/SNOM cantilever probes: Fabrication and measurements. *Microelectronic Engineering* 2000, *53*. 183-186.

20. J. Abbou, C. Demaille, M. Druet, J. Moiroux, Fabrication of Submicrometer-Sized Gold Electrodes of Controlled Geometry for Scanning Electrochemical-Atomic Force Microscopy. *Analytical Chemistry* 2002, *74*. 6355-6363.

21. D. P. Burt, N. R. Wilson, J. M. R. Weaver, P. S. Dobson, J. V. Macpherson, Nanowire Probes for High Resolution Combined Scanning Electrochemical Microscopy − Atomic Force Microscopy. *Nano Letters* 2005, *5*. 639-643.

22. R. J. Fasching, Y. Tao, F. B. Prinz, Cantilever tip probe arrays for simultaneous SECM and AFM analysis. *Sensors and Actuators B: Chemical* 2005, *108*. 964-972.

23. J. V. Macpherson, P. R. Unwin, Combined Scanning Electrochemical−Atomic Force Microscopy. *Analytical Chemistry* 2000, *72*. 276-285.

24. J. V. Macpherson, P. R. Unwin, Noncontact Electrochemical Imaging with Combined Scanning Electrochemical Atomic Force Microscopy. *Analytical Chemistry* 2001, *73*. 550-557.

25. A. Davoodi, J. Pan, C. Leygraf, S. Norgren, In Situ Investigation of Localized Corrosion of Aluminum Alloys in Chloride Solution Using Integrated EC-AFM/SECM Techniques. *Electrochemical and Solid-State Letters* 2005, *8*. B21-B24.

26. C. Kranz, G. Friedbacher, B. Mizaikoff, A. Lugstein, J. Smoliner, E. Bertagnolli, Integrating an Ultramicroelectrode in an AFM Cantilever: Combined Technology for Enhanced Information. *Analytical Chemistry* 2001, *73*. 2491-2500.

27. C. Kranz, A. Kueng, A. Lugstein, E. Bertagnolli, B. Mizaikoff, Mapping of enzyme activity by detection of enzymatic products during AFM imaging with integrated SECM-AFM probes. *Ultramicroscopy* 2004, *100*. 127-134.

28. A. Kueng, C. Kranz, A. Lugstein, E. Bertagnolli, B. Mizaikoff, Integrated AFM–SECM in Tapping Mode: Simultaneous Topographical and Electrochemical Imaging of Enzyme Activity. *Angewandte Chemie International Edition* 2003, *42*. 3238-3240.

29. A. Kueng, C. Kranz, A. Lugstein, E. Bertagnolli, B. Mizaikoff, AFM-Tip-Integrated Amperometric Microbiosensors: High-Resolution Imaging of Membrane Transport. *Angewandte Chemie* 2005, *117*. 3485-3488.

30. A. Kueng, C. Kranz, B. Mizaikoff, A. Lugstein, E. Bertagnolli, Combined scanning electrochemical atomic force microscopy for tapping mode imaging. *Applied Physics Letters* 2003, *82*. 1592.

31. A. Lugstein, E. Bertagnolli, C. Kranz, A. Kueng, B. Mizaikoff, Integrating micro- and nanoelectrodes into atomic force microscopy cantilevers using focused ion beam techniques. *Applied Physics Letters* 2002, *81*. 349.

32. T. Akiyama, M. R. Gullo, N. F. De Rooij, A. Tonin, H.-R. Hidber, P. L. T. M. Frederix, A. Engel, U. Staufer, Development of insulated conductive probes with platinum silicide tips for atomic force microscopy in cell biology. *Japanese Journal of Applied Physics, Part 1* 2004, *43*. 3865-3867.

33. P. S. Dobson, J. M. R. Weaver, M. N. Holder, P. R. Unwin, J. V. Macpherson, Characterization of Batch-Microfabricated Scanning Electrochemical-Atomic Force Microscopy Probes. *Analytical Chemistry* 2004, *77*. 424-434.

34. Y. Hirata, S. Yabuki, F. Mizutani, Application of integrated SECM ultra-micro-electrode and AFM force probe to biosensor surfaces. *Bioelectrochemistry* 2004, *63*. 217-224.

35. H. Shin, P. J. Hesketh, B. Mizaikoff, C. Kranz, Batch Fabrication of Atomic Force Microscopy Probes with Recessed Integrated Ring Microelectrodes at a Wafer Level. *Analytical Chemistry* 2007, *79*. 4769-4777.

36. H. Shin, P. J. Hesketh, B. Mizaikoff, C. Kranz, Development of wafer-level batch fabrication for combined atomic force-scanning electrochemical microscopy (AFM-SECM) probes. *Sensors and Actuators B: Chemical* 2008, *134*. 488-495.

37. P. R. Roberge, Handbook of Corrosion Engineering; McGraw-Hill: New York. 2000.

38. A. Bastos, O. Karavai, M. Zheludkevich, K. Yasakau, M. Ferreira, Localised Measurements of pH and Dissolved Oxygen as Complements to SVET in the Investigation of Corrosion at Defects in Coated Aluminum Alloy. *Electroanalysis* 2010, *22*. 2009-2016.

39. L. Niu, Y. Yin, W. Guo, M. Lu, R. Qin, S. Chen, Application of scanning electrochemical microscope in the study of corrosion of metals. *Journal of Materials Science* 2009, *44*. 4511-4521.

40. P. Schmuki, S. Virtanen, Electrochemistry at the nanoscale, Springer, New York, 1st edn, 2009. 2009.

41. V. Maurice, L. H. Klein, P. Marcus, Atomic Structure of Metastable Pits Formed on Nickel. *Electrochemical and Solid-State Letters* 2001, *4*. B1-B3.

42. V. Maurice, L. H. Klein, P. Marcus, Atomic-scale investigation of the localized corrosion of passivated nickel surfaces. *Surface and Interface Analysis* 2002, *34*. 139-143.

2 Background

This chapter introduces the background of electrochemical techniques and scanning probe techniques relevant to the research presented in this thesis. In particular, atomic force microscopy and scanning electrochemical microscopy are highlighted.

2.1 Microelectrochemistry

2.1.1 Properties of miniaturized electrodes

Although miniaturized electrodes have been used in physiological applications for a long time[1-4], efforts to use and theoretically describe miniaturized electrodes, which are a key element in modern electrochemistry, were introduced in the 1980`s[5-6]. Small electrodes are typically denoted as microelectrodes or ultramicroelectrodes (UME); with dimensions in the nanometer range they are frequently named as "nanodes" or nanoelectrodes. Generally, per definition a microelectrode is an electrode with less than 100 μm^2 of surface area[7] and a UME is an electrode having at least one dimension, also called critical dimension, smaller than 25 μm[8]. For nanoelectrodes, dimensions are not as clearly defined as sub-microelectrodes are frequently called nanoelectrodes in literature. These small dimensions are meaningful since the behavior of microelectrodes in comparison to macroelectrodes is significantly different. In this section, the miniaturized electrodes are referred to as microelectrodes.

The difference in the theoretical treatment between macro- and microelectrode is related to their characteristics of mass transport, which can occur by three different mechanisms: convection, migration, and diffusion. Mostly, diffusion is considered as a sole mode of mass transport in theory since convection can be neglected in stationary solutions, and migration can be minimized by adding an excessive amount of supporting electrolyte. As Heinze et al.[9] has illustrated, nonlinear diffusion caused by curvature effects must be considered in describing the diffusion towards a microelectrode in contrast to dominating planar diffusion towards a macroelectrode (**Figure 2.1)**. Unlike the diffusive mass transport towards a macroelectrode, the diffusion from angular direction dominates in small-sized electrodes and this angular diffusion is referred to as hemispherical diffusion. Mathematically, this enhanced diffusion led to modification of the Cottrell equation, which represents the current-time relationship in planar diffusion (**Equation 2.1-2.2**)[8].

Cottrell equation $$i = \frac{nFAD_O^{1/2}C_O^*}{\pi^{1/2}t^{1/2}}$$ Equation 2.1

$$i = \frac{nFAD_O^{1/2}C_O^*}{\pi^{1/2}t^{1/2}} + \frac{nFAD_OC_O^*}{r_0}$$ Equation 2.2

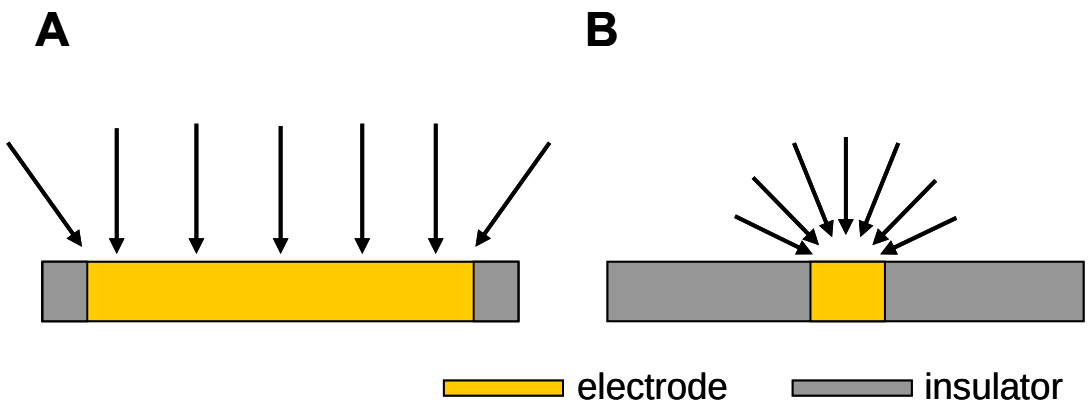

Figure 2.1 Schematic of diffusive mass transport at (A) macroelectrode (B) microelectrode[9].

where n is the number of electrons transferred in the electrode reaction, F is the Faraday constant, A is the electrode area, D_O is the diffusion coefficient of electroactive species O, C_O is the concentration of electroactive species O, t is the time and r_0 is the radius of an electrode. The modified Cottrell equation is derived from solving the Fick's laws of diffusion, which contains a radial component for microelectrodes due to the curvature effects. This second time-independent term in **Equation 2.2** of the modified Cottrell equation is related to (hemi)spherical diffusion towards the microelectrode enhancing the mass transfer resulting in a current contribution, which is not limited by diffusion anymore. The first term in the equation, is equal to the Cottrell equation and dominates at the beginning at short time periods when the diffusion layer is smaller than the electrode radius and planar diffusion is dominating like towards a macroelectrode. However, the second time-independent term becomes significant at longer times as the diffusion layer gets larger compared to electrode size.

Microelectrodes show several advantages compared to macroelectrodes in electrochemical analysis based on the enhanced mass transport and the small size. The first attractive advantage is the capability to rapidly achieve steady-state current in comparison to a macroelectrode. The rapidly achieved steady-state current signal is advantageous in electrochemical analysis as it does not require timing devices or complicated input signals[10] and it is reproducible as it does not suffer from natural convection. The dependence of the elapsed time to attain a steady-state signal is dependent of the size of an electrode, which was calculated and tabulated for disk-shaped microelectrodes by Zoski (**Table 2.1**)[11].

Table 2.1 Time to reach a steady-state current at disk electrode[11].

Radius (μm)	0.25	0.50	1.0	2.5	5.0	10	25
Time (ms)	3.2	13	52	320	1300	5200	32000

* A diffusion coefficient of 1.00×10^{-9} $m^2 s^{-1}$ was used for calculation.

The advantage of achieving steady-state current after a short period of time is important for sensing applications. As the number of electroactive species converted at the electrode surface is small, the concentration gradient from the electrode surface to the bulk solution is steeper since the distance is short in comparison to a macroelectrode as shown in **Figure 2.2**[9]. Consequently, the sensitivity to the activity of sample can be increased as the rate of mass transport is enhanced.

Another advantage of microelectrodes over macroelectrodes is the reduced charging current (i_c). Charging current results from charging the double-layer capacitance, when the potential applied to an electrode is changed. The charging current is unspecific,

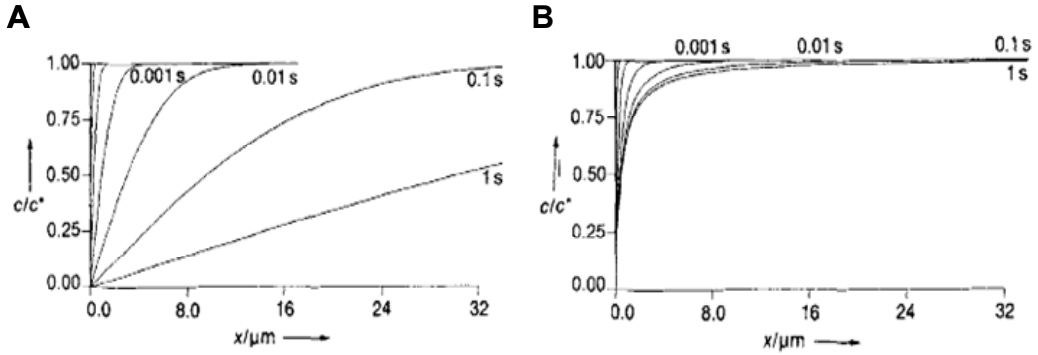

Figure 2.2 Concentration profiles for different times (t) after application of a potential step at (A) macroelectrode: planar diffusion, and (B) microelectrode: hemispherical diffusion. Diffusion coefficient D = 1 x 10^{-9} m^2 s^{-1}, c/c* = normalized concentration, r = 0.5 µm and x = distance from electrode[9].

and hence cannot be used as an analytical signal. In addition, it is convoluted with the faradaic current and therefore distorts the analytical signal. Hence, increasing the ratio of faradaic current to charging current is desirable. Considering an electrical equivalent circuit with a resistance of the solution (R) and a double layer capacitance (C) in series, the charging current (i_c) caused by a potential step from E_1 to E_2 is given by **Equation 2.3**[12] where the capacitive current is exponentially decaying over time. Since the

$$i_c = \frac{E_2 - E_1}{R} \exp\left(-\frac{t}{RC}\right) \qquad \text{Equation 2.3}$$

dimension of the double-layer capacitance is proportional to the surface area of the electrode as expressed in **Equation 2.4**, charging currents are less pronounced at microelectrodes.

$$RC \alpha \mathrm{r} \qquad \text{Equation 2.4}$$

where r is radius of disk-shaped electrode. For analytical applications, the reduction in charging current contribution results in higher signal-to-noise ratio or improved sensitivity.

In addition, at microelectrodes a minimized ohmic drop (IR drop) is obtained, which corresponds to the loss of a fraction of the applied potential between two electrodes, while the current flows through a solution. When planar diffusion is dominant, the current is proportional to the size of the electrode resulting in a decreased IR drop as the radius of the electrode is decreased. On the other hand, the IR drop no longer depends on the size of the electrode when steady-state current is observed. However, the diffusion-limited current is proportional to the radius of the electrode, and hence the IR drop is negligible at such small current levels (nA to pA). The significant reduction of IR drop at microelectrodes is very useful where current densities are high for example when using fast scan voltammetry[13-14]. Finally, the geometrically small dimensions allow using microelectrodes for measurements in small volume of samples such as bio-cells and enable their application in microelectronic devices. The applications of microelectrodes will be discuss in the following sections.

2.1.2 Voltammetry

Voltammetry is the most used electroanalytical technique. In voltammetric techniques, the potential applied to an electrode may be held constant or varied with time using different potential profiles. Information can be derived about the analytes by monitoring simultaneously the resulting current. This occurs by the polarization of the electrode, which means the potential of the electrode is deviated from its equilibrium value. **Figure 2.3** shows a variety of potential excitation signals, which have been used in voltammetry techniques. Among these illustrated techniques, cyclic voltammetry (CV) is the most popular voltammetric method (**Figure 2.3D**). In CV, the potential applied to the

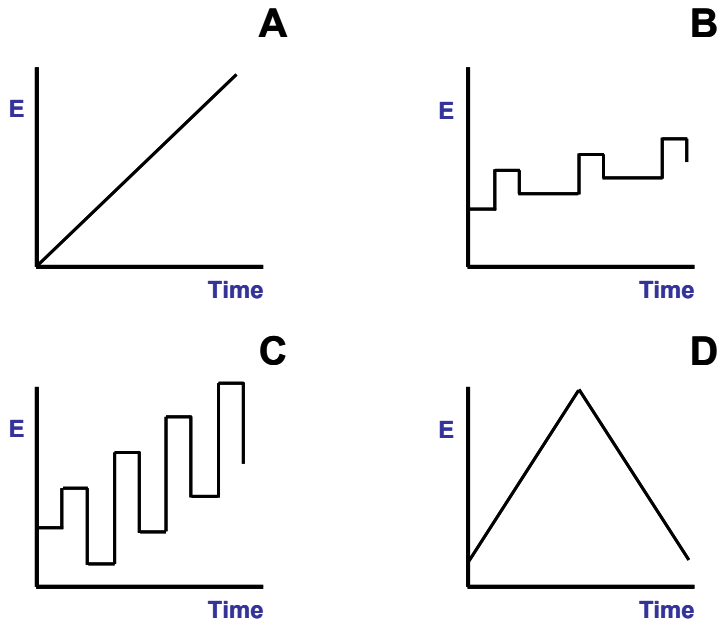

Figure 2.3 Examples of potential excitation signals in voltammetry: (A) linear sweep voltammetry, (B) differential pulse polarography, (C) square-wave voltammetry, (D) cyclic voltammetry.

working electrode has a triangular waveform. The applied potential is linearly swept from an initial potential value to a switching potential at which the reversal of direction of the potential sweep takes place and the potential returns to the initial value. The resulting current is plotted as a function of applied potential. Among many applications, CV is routinely applied for studying kinetics, rate constants and mechanisms of electrochemical reactions. The rest of this section is focusing on CV in microelectrochemistry.

Since the introduction of microelectrodes in electrochemistry, CV enabled new fields like measuring in highly resistive media[15], applying fast scan rates known as fast scan voltammetry[16-17], perform microscopic analysis[18], which would not be available with macroelectrodes based on the characteristics described in the previous section. CVs recorded at microelectrodes show a significantly different appearance compared to CVs recorded at macroelectrodes due to the dissimilar type of mass transport. For the following electron transfer reaction (**Equation 2.5**),

$$O + ne^- \leftrightarrow R \qquad \text{Equation 2.5}$$

where O is the oxidized form of the electroactive species, and R is its reduced form, the shape of the CVs recorded at a microelectrode and macroelectrode differs significantly as shown in **Figure 2.4**[19]. Comparing with the CV in **Figure 2.4A** resulting from planar diffusion towards a macroelectrode, the hemispherical diffusion profile towards a

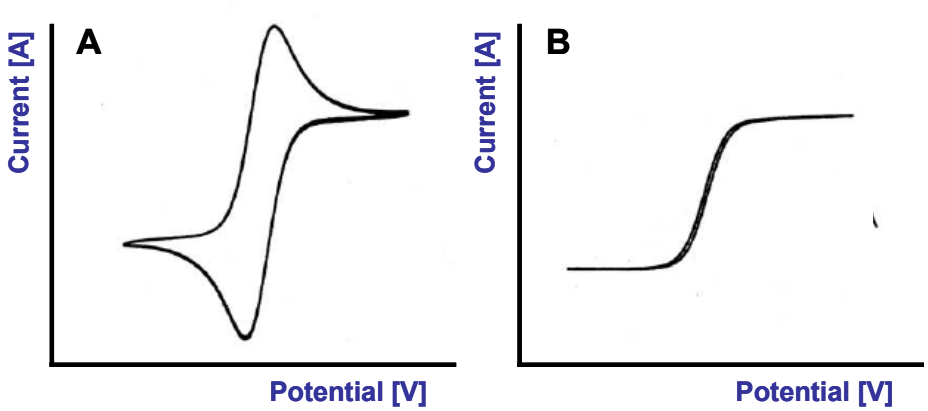

Figure 2.4 The representative shape of the cyclic voltammogram depends on the diffusion profiles: **(**A**)** planar diffusion profile towards a macroelectrode and (B) hemispherical diffusion profile towards a microelectrode[19].

microelectrode leads to a sigmoidal shape (**Figure 2.4B**). Due to the enhanced mass transfer a steady-state current is rapidly reached, which corresponds to the plateau value in the sigmoidal-shaped CV.

The Fick`s second law, which describes the time-dependent change of the diffusion field, is expressed by the equation shown below (**Equation 2.6**) for any type of geometry of electrodes[8].

$$\frac{\partial C_O}{\partial t} = D_O \nabla^2 C_O \qquad \text{Equation 2.6}$$

where C_O is the concentration of oxidized species, D_O is the diffusion coefficient of O, ∇^2 is the Laplacian operator. For a disk-shaped microelectrode **(Figure 2.5**), which is the most common geometry for microelectrodes, ∇^2 is given by

$$\nabla^2 = \frac{\partial^2}{\partial r^2} + \frac{1}{r}\frac{\partial}{\partial r} + \frac{\partial^2}{\partial z^2}$$ Equation 2.7

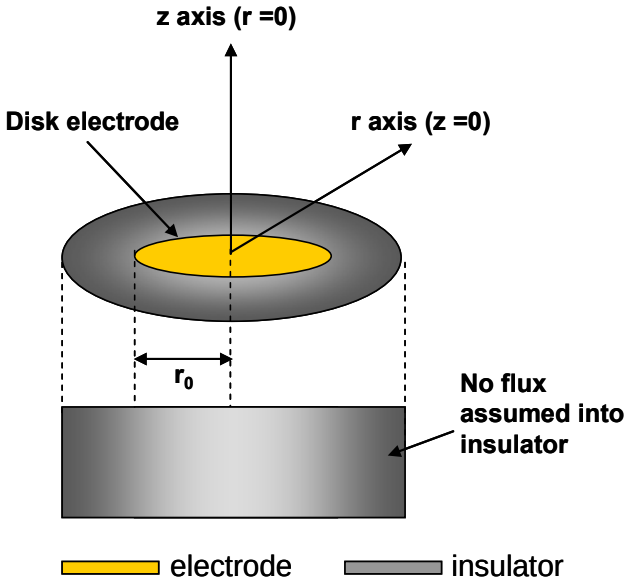

Figure 2.5 Diffusion geometry at a disk-shaped microelectrode.

where z is linear displacement perpendicular to the plane of electrode at z = 0 and r is the radial position perpendicular to the axis of symmetry at r = 0. Consequently, the Fick`s second law can be expressed as shown below (**Equation 2.8**) combining **Equation 2.6** and **2.7**,

$$\frac{\partial C_O(r,z,t)}{\partial t} = D_O\left[\frac{\partial^2 C_O(r,z,t)}{\partial r^2} + \frac{1}{r}\frac{\partial C_O(r,z,t)}{\partial r} + \frac{\partial^2 C_O(r,z,t)}{\partial z^2}\right]$$ Equation 2.8

For solving this equation, five boundary conditions need to be considered. Firstly, the concentration C_O at the surface of the electrode before the potential step (t = 0) is the same as the concentration C_O^* in bulk solution.

$$C_O(r,z,0) = C_O^* \qquad \text{Equation 2.9}$$

It is assumed that the concentration far from the surface of the electrode is the same as the concentration in the initial bulk solution, since it is not altered during the measurement.

$$\lim_{z\to\infty} C(r,z,t) = C_O^* \lim_{r\to\infty} C(r,z,t) = C_O^* \qquad \text{Equation 2.10}$$

Since there is no flux at the surface of insulator plane, the following boundary has to be considered.

$$\left.\frac{\partial C_O(r,z,t)}{\partial z}\right|_{z=0} = 0 \qquad (r > r_0) \qquad \text{Equation 2.11}$$

The final boundary condition describes the fact that the concentration of oxidized species is assumed to be zero at the surface of the electrode since it is immediately reduced at the surface.

$$\left(r \le r_0, t > 0\right) C_O\left(r,0,t\right) = 0 \qquad \text{Equation 2.12}$$

This diffusion equations can be solved by simulations[20], resulting in the concentration profiles, which allow calculating the diffusion-limited current by integration of the concentration gradient at the surface of an electrode. Nowadays commercial software packages allow solving these equations. However, the diffusion-limited current of a disk microelectrode at steady-state conditions can be calculated using a simple relation as shown in **Equation 2.13,** which is derived from dimensionless parameters and accounts for the disk geometries[21-22].

$$i_{T,\infty} = 4nFD_O C_O^* r_0 \qquad \text{Equation 2.13}$$

2.1.3 Potentiometry

Unlike voltammetry, which measures the current that develops in an electrochemical cell, potentiometry measures the potential change at an electrode in response to the concentration change of an analyte in solution. The measurement of the electrode potential with respect to the reference electrode (RE) is performed at thermodynamic equilibrium conditions, while any appreciable currents are compensated by the vast internal resistance of the potentiometer so that there is no current flow through the electrodes. The potentiometric response of an electrochemical cell is determined by the Nernst equation[8] (**Equation 2.14**)

$$E = E^0 + \frac{RT}{nF} \ln\left(\frac{a_O}{a_R}\right) \qquad \text{Equation 2.14}$$

where E^0 is the standard potential, R is the gas constant, F is the Faraday constant, T is the absolute temperature, a_R and a_O are the activities which are assumed to be the concentration of the reduced and oxidized species in dilute solution, respectively. The electrochemical cell is at thermodynamic equilibrium condition during the measurement and there is no current flowing between the electrodes in solution. However, selectivity and interfering ions are an issue in potentiometric measurements, as any change at the junction potential leads to a potential change, which essentially affect the potential need to be taken into account. In **Equation 2.15** the semi-empirical Nickolsky equation[23] is shown, derived from the Nernst equation including the effect of interfering ions.

$$E = E^0 + \frac{RT}{nF} \ln\left[a_i + k_{ij}\left(a_j\right)^{n/m}\right] \qquad \text{Equation 2.15}$$

where the subscript i refers to the analyte, the subscript j refers to the interfering species, m is the charge number corresponding to the charge of interfering ions, k is the selectivity coefficient, n is the number of electrons.

Ongoing research focuses on measurements in small volumes and observation of discrete spatial events at the microscale. Hence, miniaturization of electrodes for potentiometric sensors received substantial attention. Among potentiometric sensors, the pH glass electrode is the most used and robust ion-selective electrode[24]. In 1959, Hinke

presented the first potentiometric glass microelectrode for piercing cells and measuring interior ions such as sodium and potassium[25]. Over the years, there have been several attempts to use miniaturized glass electrodes for pH measurements at the microscale or in small volumes[26-30]. The glass electrode has several advantages in comparison to other pH sensitive materials such as high selectivity, sensitivity and long life time[31]. However, it is also limited in application and further miniaturization due to the intrinsic nature of the glass membrane. Limitations such as high impedance, acid and alkaline error, instability at high temperature, difficulty to further miniaturize and mechanical fragility, which interfere with *in vivo* applications have initialized a fair amount of research to develop alternative non-glass based miniaturized potentiometric sensors[32]. The representatives will be discussed in the next sections.

2.1.4 Solid-state potentiometric sensors

Typically, solid-state potentiometric sensors are based on ion-sensitive field effect transistors (ISFET) and ion-selective electrodes (ISE). Section 2.1.4.1 briefly introduces ISFET and section 2.1.4.2 discusses solid-state miniaturized ISE, which are promising to overcome the current drawbacks of miniaturized pH glass electrodes. The discussion will be restricted to measurements of hydronium ion concentration since part of this thesis is concerned with the development of an AFM tip-integrated pH sensor.

2.1.4.1 Ion-sensitive field effect transistor (ISFET)

Bergveld published the first ISFETs, which were developed to measure pH or the exchange of sodium and potassium ions at nerve and muscle membrane[33-34]. The

principle of an ISFET is shown as illustration in **Figure 2.6**[35]. The SiO_2 layer is coated with a gate material such as Si_3N_4, Al_2O_3 or Ta_2O_5, which is again covered with an ion-sensitive layer. The solution acts as a gate electrode instead of a metal gate in a typical metal-oxide-semiconductor field-effect transistor (MOSFET). The potential generated from the gate is affected by the change of ion concentration such as e.g., a pH change. Consequently, the measured current is varied depending on the change of ion concentration. Usually, a feedback voltage is supplied to the reference electrode, which is in a closed circuit and the system is operated at constant current regime. ISFET offers high signal-to-noise ratio as a FET as a trans-conductance amplifier is used. However, its precision is not as good as the glass electrode yet and it is limited in operation to a pressure of less than approx. 2 bar and a temperature up to about 85 ºC. Also, life-time stability and film formation on the surface are still challenging issues[35-36].

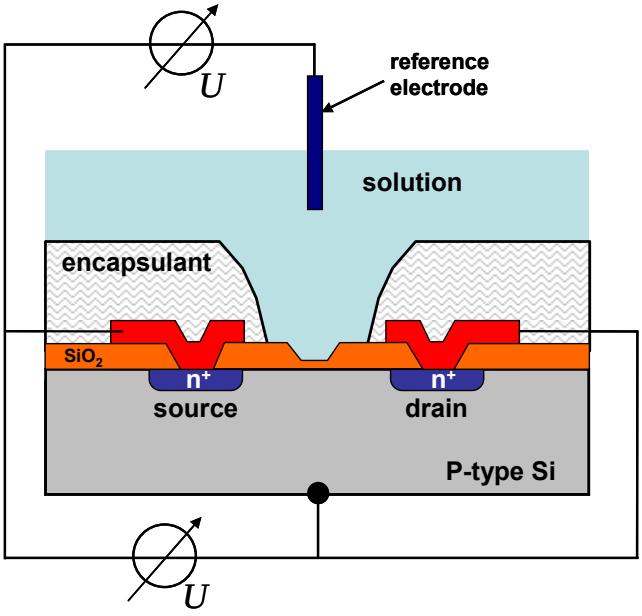

Figure 2.6 Schematic of an ion-sensitive field-effect transistor (ISFET). Re-sketched from[35].

2.1.4.2 Solid-state miniaturized ion-selective electrode

ISEs are one of the most applied potentiometric sensors. In principle, ISE can be defined as a transducer that converts the concentration of a specific ion into an electrical potential. As mentioned above, pH glass electrodes are the most routinely used form of ISE. However, the listed drawbacks of pH glass electrodes have motivated substantial research to develop non-glass based potentiometric sensors. Metal/metal oxide systems have attracted considerable attention as candidates that can replace pH glass electrodes for analysis at the microscopic scale. Various types of metal/metal oxides have been investigated as pH sensing schemes such as: Sb_2O_3, IrO_2, RuO_2, OsO_2, Ta_2O_5, RhO_2, TiO_2, SnO_2, ZrO_2, Co_3O_4, PbO, Bi_2O_3, PtO_2, PbO_2 and their performances have been reviewed in several publications[36-40]. Generally, metal/metal oxide electrodes have better

stability in harsh conditions (for example temperature up to 250 ºC[41]) and suitable for miniaturization compared to pH glass electrode. Among the listed materials, Sb/Sb_2O_3 is the most widely used solid-state pH sensing scheme since Sb/Sb_2O_3 electrodes can be easily prepared. In addition, Sb/Sb_2O_3 electrodes can be used in acid-base titration and in strong acid such as HF contained solution[38]. The surface of antimony is spontaneously oxidized and does not need any further modification steps. Also, miniaturized Sb/Sb_2O_3 electrodes have been successfully used for the pH measurement at a microscopic scale and for in vivo measurements[42-47]. The pH response of antimony is governed by **Equation 2.16**[38] and as shown is directly depends on the activity of the hydronium ions in a range from pH3 to pH11.

$$Sb_2O_3 + 6H^+ + 6e^- \leftrightarrow 2Sb + 3H_2O \qquad \text{Equation 2.16}$$

The potential is governed by the Nernst equation as shown below[43]

$$E = E^0 - \frac{0.059}{n}\log\frac{1}{\left(a_{H^+}\right)^6} = 0.152 - 0.059\,pH \qquad \text{Equation 2.17}$$

Based on comparative studies[36-38,40], Ir/IrO_2 is known as the most promising among the listed materials due to its superior characteristics such as: 1) linear response in a wide pH range[38,48-49], 2) high stability in harsh conditions such as high temperature, high pressure, chemically aggressive environments[41,50-52], 3) fast response even in non-aqueous systems[53] and 4) low sensitivity to interferences and to convective effects[38,54-55].

Unlike Sb/Sb_2O_3, Ir/IrO_2 electrodes are fabricated using several different techniques. The Ir/IrO_2 system has different characteristics depending on the fabrication as its composition varies with the preparation method. Frequently used fabrication schemes are 1) thermal decomposition of iridium salts[56-59], 2) high temperature oxidation of an iridium substrate[60], 3) oxygen plasma sputtering from metallic iridium[51-52,61-62], 4) electrochemical oxidation of an iridium substrate[55,63-65]. The third method is advantageous in microelectrode array fabrication since it is based on the reactive RF sputtering, which is a standard semiconductor process. The iridium oxide films prepared using this method is known as sputtered iridium oxide films (SIROFs). SIROFs have typically reproducible potential/pH slope characteristics. Films prepared using methods 1 - 3 listed above are regarded as anhydrous oxide films and their potential determining reaction can be written as shown in **Equation 2.18**. The potential/pH response is close to the Nernstian value of -59 mV/pH at room temperature.

$$2IrO_2 + 2H^+ + 2e^- \leftrightarrow Ir_2O_3 + H_2O \qquad \text{Equation 2.18}$$

Iridium oxide film prepared by electrochemical oxidation of iridium is known by the acronym AIROF (anodic iridium oxide film). Iridium oxide films (IROFs) are grown at an iridium electrode by continuous cycling an applied potential in H_2SO_4 solution. During the cycling of the potential, an iridium oxide film is gradually grown while the redox transition of Ir^{III}/Ir^{IV} becomes irreversible with the film growth. AIROFs are generally regarded as highly hydrated and gel-like films with an amorphous structure[66]. The oxidation reaction can be expressed by following equation[36]

$$\mathrm{IrO_x(OH)}_y + ze^- + zH^+ \leftrightarrow \mathrm{IrO}_{x-z}\mathrm{(OH)}_{y+z} \quad (x \approx 2, y << 1, z \approx 1)$$ Equation 2.19

Unlike SIROF electrodes, AIROF electrodes have different characteristics of the pH response depending on the oxidation state, crystal structure and thickness of the layer. It has been reported that a higher oxidation state results in a steeper slope of the potential/pH response[67]. Monocrystalline AIROF show a more stable response and a slightly steeper slope of response compared to polycrystalline films[55]. In addition, thicker AIROF films reveal a better reproducibility of response in comparison to thinner films[68]. Typically, AIROF electrodes reveal so called super-Nernstian behavior with typical slopes of the pH response of -62 to -77 mV/pH[38].

2.2 Scanning probe microscopy (SPM)

Scanning probe microscopy (SPM) has become the most widely used surface analytical technique in laboratories since scanning tunneling microscopy (STM) was introduced by Binnig and Rohrer in 1982[69-70]. STM is capable of resolving features at an atomic scale and the inventors received the Nobel Prize with this revolutionary advancement in surface science. The introduction of STM has been a milestone towards the development of a multitude of SPM techniques, which are categorized based on their "nearfield" interaction between a SPM tip and a sample surface. In the following sections, two members of the SPM family, the atomic force microscopy (AFM) and the scanning electrochemical microscopy (SECM) will be described in more detail as they are the main SPM techniques used throughout this thesis.

2.2.1 Atomic force microscopy (AFM)

Since Binnig et al. introduced AFM in 1986[71], it is one of the most popular SPM techniques in laboratories across the scientific disciplines. Unlike STM, AFM is applicable to non-conducting samples. As mentioned above, the criteria for classification of SPM is the type of interaction between a tip and a sample surface. In AFM, attractive or repulsive forces are monitored between a sharp tip and a sample. The tip is fixed at a flexible cantilever, which serves as a force sensor. Hence, this cantilever with the sharp tip is one of the key elements in performance of AFM determining the achievable resolution. In AFM operation, the flexible cantilever is scanned across the sample surface in a line-by-line pattern. The interacting force between the tip and sample surface causes minute deflection of the cantilever during scanning induced by the change of force interaction. In constant force mode[72], which is used in most applications, the cantilever moves in three-dimensions utilizing piezoelectric actuator elements, which are guiding the tip at a constant value of deflection across the sample surface. Consequently, the change of the applied voltage to the piezoelectric actuator elements keeps the deflection signal constant and is translated into topographical information. **Figure 2.7** shows a schematic illustration of the optical detection scheme of the cantilever deflection. A laser beam is reflected from the rear side of the cantilever and focused to a position-sensitive photo detector, which consists of a 4-quadrant photodiode. With 4-quadrants, not only bending, but also the torsion of the cantilever can be detected. The photocurrent is processed by the controller generating an error signal, which is controlled in a feedback to maintain the interacting force constant during scanning.

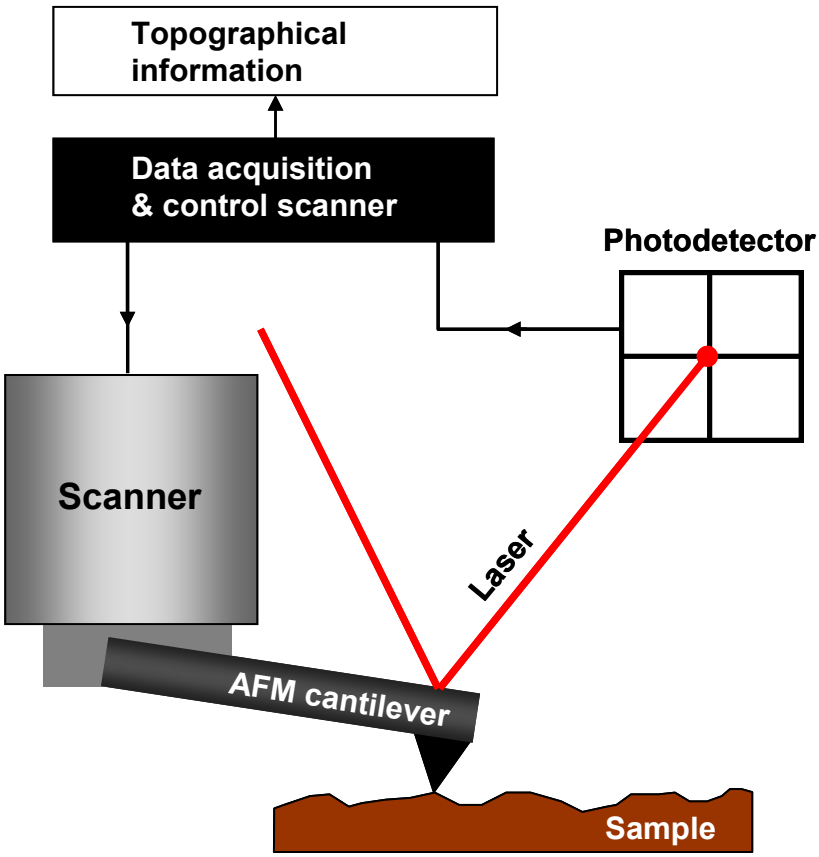

Figure 2.7 Schematic of the detection scheme of cantilever deflection.

Several modes have been introduced in AFM, which can be categorized as static and dynamic modes. The static modes measure the static deflection of a cantilever, while the dynamic properties such as eigenfrequency or oscillation amplitude are measured in the dynamic modes. Contact mode and intermittent mode are the most popularly used modes, which belong to static modes and dynamic modes, respectively. In contact mode[72], the tip is brought into the short-range repulsive force regime prior the tip is scanned over the sample surface maintaining a constant cantilever deflection to provide topographical information. One disadvantage of contact mode operation is that the downward force in the repulsive regime may damage soft samples such as polymers and biological samples.

This problem can be omitted by intermittent mode operation[73]. In this mode, the cantilever is oscillating at a frequency of a few hundred kilohertz and the amplitude serves as control parameter instead of a constant cantilever deflection in contact mode. The damped amplitude due to the tip-sample interaction is monitored, while the 20 − 100 nm of oscillation close to the cantilever resonant frequency is driven by a constant driving force. During the scanning, the tip is intermittently contacting the sample surface at the bottom of each oscillation, which results in a greatly reduced lateral force during scanning.

2.2.2 Scanning electrochemical microscopy (SECM)

Bard and coworkers and Engstrom and coworkers independently reported the first experiments using microelectrodes for imaging, which led to the introduction of scanning electrochemical microscopy (SECM) in 1980`s[74-76]. Unlike AFM and STM, SECM provides (electro)activity information of the sample surface. **Figure 2.8** shows an illustration of a typical SECM system. In a SECM experiment, the SECM tip, reference electrode, auxiliary electrode and sample are immersed in an electrolyte solution containing a redox mediator. The SECM tip is typically a glass-insulated disk UME with radii ranging from 0.6 to 25μm[77]. The UME is biased at a potential driving the electrochemical reaction while it is scanned in close proximity across the sample surface. Thereby, laterally resolved changes of the diffusion-limited faraday current measured at the UME are detected. The current is influenced by the morphology and electrochemical reactivity of the sample surface[78]. As the sample may be also biased in SECM measurements, a bipotentiostat is required.

SECM operates mainly in two modes: the feedback (FB) mode[74,79] and the generation-collection (GC) mode[80-81]. In GC mode, there are two types of measurements which are sample generation/tip collection (SG/TC) and tip generation/sample collection (TG/SC). Either the sample (SG/TC) or the tip (TG/SC) generates electroactive species, and the tip (SG/TC) or the sample (TG/SC) detects the species, respectively. However, this section only describes FB mode in more detail as only this mode was used in the AFM-SECM experiments presented throughout this thesis.

In FB mode SECM, a reversible redox mediator, which is added to solution in the millimolar concentration range, is oxidized or reduced when the UME is biased at a sufficient potential. When the tip is far from the substrate, a diffusion-limited steady-state current is obtained as described in section 2.1.2 for a disk-shaped UME. If the tip is

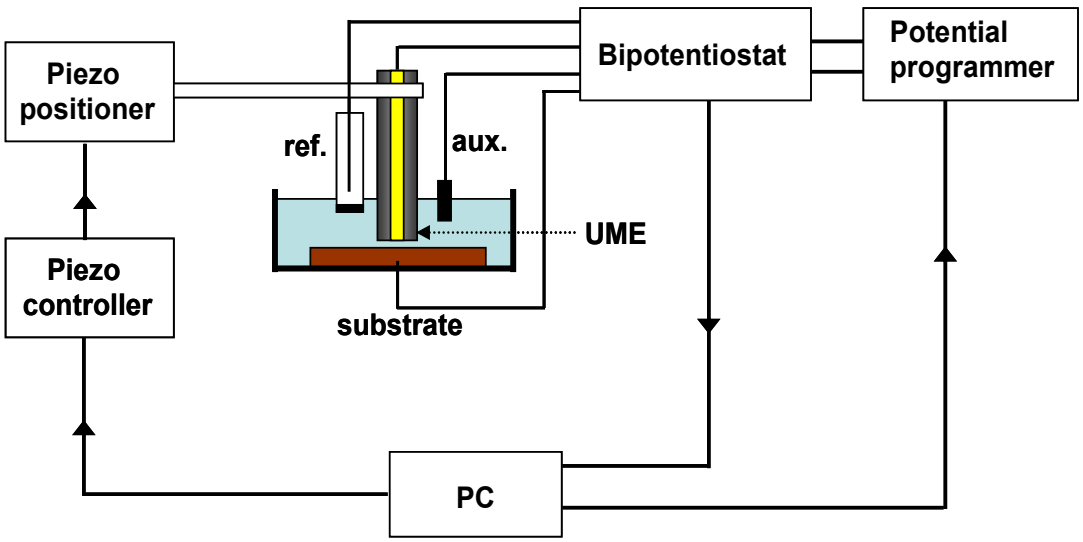

Figure 2.8 Schematic of a SECM system. Re-sketched from[77].

brought into close vicinity of an insulating surface, the current measured at the UME is decreasing since the hemispherical diffusion of the mediator towards the electrode is blocked. On the other hand, an increase of the tip current is observed, if the UME is brought into close vicinity of a conductive surface because the redox mediator can be recycled if a non-biased conductive sample is large compared to the dimensions of the tip or the sample is biased at a potential favoring the re-oxidation or re-reduction of the redox mediator (**Figure 2.9**). This dependence of the faradaic current on the nature of the sample and the distance of the tip to the sample are among the main factors determining electrochemical imaging in FB mode SECM. **Figure 2.9** shows a typical dependence of the measured current on the distance between the tip and the surface. Such current-distance curves are known as approach curves, which are used in conventional SECM to determine the optimal working distance for constant height imaging.

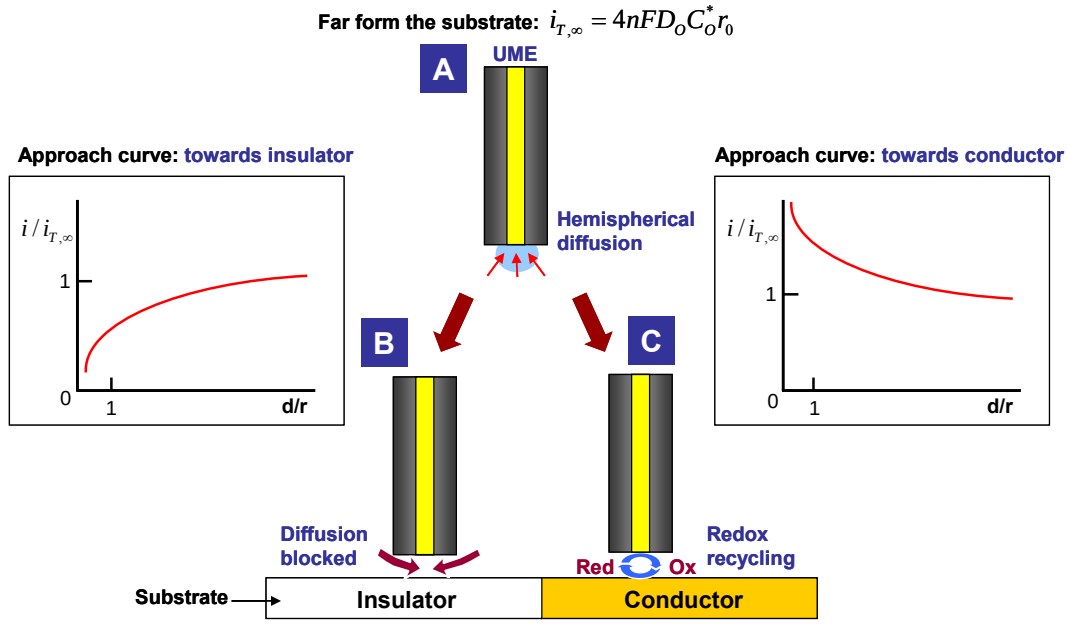

Figure 2.9 Principle of FB mode SECM: (A) when the tip is far from the substrate, a steady-state current can be calculated based on $i_{T,\infty} = 4nFD_O C_O^* r_0$ (Equation 2.13) for a disk-shaped UME. (B) A decrease in current is observed due to diffusion blockage when the tip is in close vicinity of an insulating surface. (C) An increase current is observed due to the recycling of the redox mediator if the tip is close to a conductive surface. Typically for approach curves, the distance (d) is normalized to the radius (r) and the steady-state current is normalized to the current recorded in bulk solution.

Besides the nature of the sample, the measured steady-state current is also affected by the tip geometry, the dimensions of the insulating sheath, which is typically expressed by the RG value, and the distance between tip and sample. The RG value defined by **Equation 2.20**, is used to characterize the tip, relating the radius of insulating sheath (r_g), and the radius of electroactive area (r). The RG value of the tip is one of the

$$RG = \frac{r_g}{r}$$ Equation 2.20

critical factors affecting steady-state current in SECM experiments as the size and shape (profile) of the hemispherical diffusion is influenced by the RG value. A more detailed discussion of the tip geometry and influence of the RG value is provided in section 4.3.1.

2.2.3 Combined AFM-SECM technology

AFM and SECM are among the most popular SPM techniques. While AFM is meanwhile a routine surface characterizing tool as described before, SECM has gained significant interests within the last decade. However, both techniques suffer from limitations. For example, AFM without any modification of the AFM tip provides limited chemical information despite its versatility. In contrast, topographical resolution of SECM cannot compete with the resolution routinely achieved by AFM.

Adding additional functionality to SPM to achieve complementary information has been shown for several hyphenated scanning probe techniques[82-83]. From the standpoint of micro-electrochemical characterization, the combination of AFM-SECM is very promising. Integrating electrodes into AFM tips or fabricating electrodes with the shape and feature of a cantilever allows positioning the electrode close to the sample surface independently from the faradaic current signal. Based on several approaches, which have been published over the last 10 years, the geometry of the proposed AFM-SECM probes can be categorized into two types, depending on where the electrode is defined at the AFM tip.

One approach is based on defining an electrode at the apex of the AFM tip[83-87]. This technique was first described by Macpherson and Unwin using flattened and etched Pt-microwires, which were subsequently insulated exposing a conical sub-microelectrode[83]. After bending the wire in form of a cantilever, the wire was covered with a polymeric insulation layer, which retracts during cross linking induced by heating to expose an electrode at the very end of the tip (**Figure 2.10**). This approach enables high resolution electrochemical imaging with small conical electrodes, but this advantage is often correlated with the disadvantage of sequential measurements of topography and electrochemistry.

The second approach is focused on defining the electroactive area recessed at a certain distance from the apex of the tip[82,88-95]. This approach was first described by Kranz et al[82] based on the modification of commercial AFM cantilevers. The original AFM tip was sequentially coated with electrode material and insulation layer. Then the

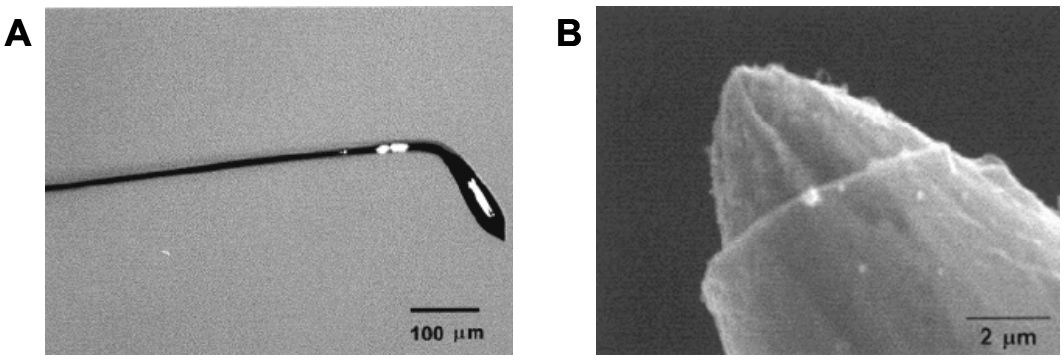

Figure 2.10 (A) Optical micrograph of a coated AFM-SECM probe. (B) SEM image of the apex of the AFM-SECM probe with the electrode defined at the apex of the tip[83].

tip was structured utilizing focused ion beam milling as shown in **Figure 2.11**[82,90]. Consequently, the electrode was recessed from the apex of the tip and a constant distance between the electrode and the sample surface can be maintained during the combined measurement. The distance between the AFM tip-integrated electrode and the sample surface can be adjusted by the length of the modified AFM tip. This approach typically prevents abrasion of softer electrode material, contamination by the sample surface, and additionally enables the modification of the integrated electrode with a sensing layer. Also, this does not require that topographical and electrochemical data are recorded in a sequential mode.

In addition, batch fabrication approaches, which are aiming on reduced time and cost for the fabrication of AFM-SECM probes have been reported[86, 94-98]. Some of these approaches are in the first category, where electrodes are defined at the apex of the AFM

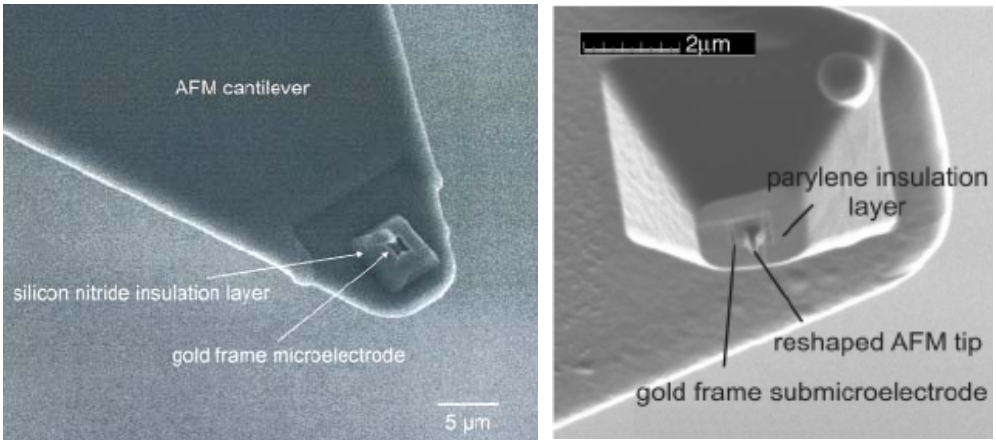

Figure 2.11 SEM images of AFM-SECM probes, which reveal a recessed electroactive area[82, 90].

tip. Fasching et al. presented FIB-assisted batch fabrication for AFM-SECM with sharpened high aspect ratio silicon tips[86]. However, all these approaches often require sequential measurements of topography and electrochemistry as described previously. Other batch fabrication approaches are aiming for probes belonging to the second category. Theses probes have the electrode recessed at a certain distance from the apex of the tip. Shin et al. reported batch-fabricated platinum ring electrodes integrated in AFM tips[94-95]. The ring-shaped electrodes were recessed from the apex of the tip without any FIB milling process. However, the electrode size was limited to micrometer scale due to the applied standard microfabrication procedures.

2.3 References

1. H. Y. Cheng, J. Schenk, R. Huff, R. N. Adams, In-vivo electrochemistry: behavior of micro electrodes in brain tissue. *Journal of Electroanalytical Chemistry* 1979, *100*. 23-31.

2. G. E. Loeb, R. A. Peck, J. Martyniuk, Toward the ultimate metal microelectrode. *Journal of Neuroscience Methods* 1995, *63*. 175-183.

3. P. E. M. Phillips, R. M. Wightman, Critical guidelines for validation of the selectivity of in-vivo chemical microsensors. *TrAC Trends in Analytical Chemistry* 2003, *22*. 509-514.

4. D. L. Robinson, B. J. Venton, M. L. A. V. Heien, R. M. Wightman, Detecting subsecond dopamine release with fast-scan cyclic voltammetry in vivo. *Clinical Chemistry* 2003, *49*. 1763-1773.

5. M. Fleischmann, S. Pons, The behavior of microelectrodes. *Analytical Chemistry* 1987, *59*. 1391A-1399A.

6. R. M. Wightman, Microvoltammetric electrodes. *Analytical Chemistry* 1981, *53*. 1125A-1134A.

7. P. M. S. Monk, Fundamentals of Electroanalytical Chemistry.; John Wiley & Sons Ltd.:Chichester. 2001.

8. A. J. Bard, L. R. Faulkner, Electrochemical Methods: Fundamentals and Applications, 2nd ed.; John Wiley & Sons, Inc.:New York. 2001.

9. J. Heinze, Ultramicroelectrodes in Electrochemistry. *Angewandte Chemie International Edition* 1993, *32*. 1268-1288.

10. A. M. Bond, K. B. Oldham, C. G. Zoski, Steady-state voltammetry. *Analytica Chimica Acta* 1989, *216*. 177-230.

11. C. G. Zoski, A survey of steady-state microelectrodes and experimental approaches to a voltammetric steady state. *Journal of Electroanalytical Chemistry* 1990, *296*. 317-333.

12. M. I. Montenegro, Q. M. Arlete., D. J. L., Microelectrodes: Theory and Applications: Kluwer Academic Publishers. 1990.

13. C. Amatore, E. Maisonhaute, G. Simonneau, Ohmic drop compensation in cyclic voltammetry at scan rates in the megavolt per second range: access to nanometric

diffusion layers via transient electrochemistry. *Journal of Electroanalytical Chemistry* 2000, *486*. 141-155.

14. D. Garreau, P. Hapiot, J. M. Savéant, Fast cyclic voltammetry at ultramicroelectrodes: Current measurement and ohmic drop positive feedback compensation by means of current feedback operational amplifiers. *Journal of Electroanalytical Chemistry* 1990, *281*. 73-83.

15. R. M. Wightman, Voltammetry with Microscopic Electrodes in New Domains. *Science* 1988, *240*. 415-420.

16. C. P. Andrieux, P. Audebert, P. Hapiot, M. Nechtschein, C. Odin, Fast scan rate cyclic voltammetry for conducting polymers electropolymerized on ultramicroelectrodes. *Journal of Electroanalytical Chemistry* 1991, *305*. 153-162.

17. R. M. Wightman, D. O. Wipf, High-speed cyclic voltammetry. *Accounts of Chemical Research* 1990, *23*. 64-70.

18. C. D. Paras, R. T. Kennedy, Amperometry and cyclic voltammetry of tyrosine and tryptophan-containing oligopeptides at carbon fiber microelectrodes applied to single cell analysis. *Electroanalysis* 1997, *9*. 203-208.

19. S. Ching, R. Dudek, E. Tabet, Cyclic Voltammetry with Ultramicroelectrodes. *Journal of Chemical Education* 1994, *71*. 602-null.

20. J. Heinze, Diffusion processes at finite (micro) disk electrodes solved by digital simulation. *Journal of Electroanalytical Chemistry* 1981, *124*. 73-86.

21. K. Aoki, J. Osteryoung, Diffusion-controlled current at the stationary finite disk electrode: Theory. *Journal of Electroanalytical Chemistry* 1981, *122*. 19-35.

22. K. Aoki, J. Osteryoung, Formulation of the diffusion-controlled current at very small stationary disk electrodes. *Journal of Electroanalytical Chemistry* 1984, *160*. 335-339.

23. D. G. Hall, Ion-Selective Membrane Electrodes: A General Limiting Treatment of Interference Effects. *The Journal of Physical Chemistry* 1996, *100*. 7230-7236.

24. W. S. Hughes, The potential difference between glass and electrolytes in contact with the glass. *Journal of the American Chemical Society* 1922, *44*. 2860-2867.

25. J. A. M. Hinke, Glass Micro-Electrodes for Measuring Intracellular Activities of Sodium and Potassium. *Nature* 1959, *184*. 1257-1258.

26. P. C. Caldwell, Studies on the internal pH of large muscle and nerve fibres. *Journal of Physiology* 1958, *142*. 22-62.

27. J. A. M. Hinke, M. R. Menard, Intracellular pH of single crustacean muscle fibres by the DMO and electrode methods during acid and alkaline conditions. *Journal of Physiology* 1976, *262*. 533-552.

28. R. C. Thomas, Membrane current and intracellular sodium changes in a snail neurone during extrusion of injected sodium. *Journal of Physiology* 1969, *201*. 495-514.

29. R. C. Thomas, New design for sodium-sensitive glass micro-electrode. *Journal of Physiology* 1970, *210*. 82-83.

30. A. Wernig, Estimates of statistical release parameters from crayfish and frog neuromuscular junctions. *Journal of Physiology* 1975, *244*. 207-221.

31. H. Galster, pH measurement-Fundamentals, Methods, Applications, Instruments, VCH publishers,; New York. 1991.

32. M. J. Madou, S. R. Morrison, Chemical Sensing with Solid State Devices, Academic Press, ; New York (1989). 1989.

33. P. Bergveld, Development of an Ion-Sensitive Solid-State Device for Neurophysiological Measurements. *Biomedical Engineering, IEEE Transactions on* 1970, *BME-17*. 70-71.

34. P. Bergveld, Development, Operation, and Application of the Ion-Sensitive Field-Effect Transistor as a Tool for Electrophysiology. *Biomedical Engineering, IEEE Transactions on* 1972, *BME-19*. 342-351.

35. S. M. Sze, Semiconductor sensors; John Wiley & Sons, Inc.:New York. 1994.

36. P. Kurzweil, Metal Oxides and Ion-Exchanging Surfaces as pH Sensors in Liquids: State-of-the-Art and Outlook. *Sensors (14248220)* 2009, *9*. 4955-4985.

37. A. Fog, R. P. Buck, Electronic semiconducting oxides as pH sensors. *Sensors and Actuators* 1984, *5*. 137-146.

38. S. Glab, A. Hulanicki, G. Edwall, F. Ingman, Metal-Metal Oxide and Metal Oxide Electrodes as pH Sensors. *Criticla Reviews In Analytical Chemistry* 1989, *21*. 29-47.

39. K. G. Kreider, M. J. Tarlov, J. P. Cline, Sputtered thin-film pH electrodes of platinum, palladium, ruthenium, and iridium oxides. *Sensors and Actuators B: Chemical* 1995, *28*. 167-172.

40. D. Midgley, A review of pH measurement at high temperatures. *Talanta* 1990, *37*. 767-781.

41. J. V. Dobson, P. R. Snodin, H. R. Thirsk, EMF measurements of cells employing metal--metal oxide electrodes in aqueous chloride and sulphate electrolytes at temperatures between 25-250°C. *Electrochimica Acta* 1976, *21*. 527-533.

42. K. Higashi, H. Fukushima, T. Urakawa, T. Adaniya, K. Matsudo, Mechanism of the Electrodeposition of Zinc Alloys Containing a Small Amount of Cobalt. *Journal of The Electrochemical Society* 1981, *128*. 2081-2085.

43. T. Honda, K. Murase, T. Hirato, Y. Awakura, pH measurement in the vicinity of a cathode evolving hydrogen gas using an antimony microelectrode. *Journal of Applied Electrochemistry* 1998, *28*. 617-622.

44. B. R. Horrocks, D. Schmidtke, A. Heller, A. J. Bard, Scanning electrochemical microscopy. 24. Enzyme ultramicroelectrodes for the measurement of hydrogen peroxide at surfaces. *Analytical Chemistry* 1993, *65*. 3605-3614.

45. H. Kofoed, Synovitis causes hypoxia and acidity in synovial fluid and subchondral bone. *Injury* 1986, *17*. 391-394.

46. N. Levine, H. Kelly, Measurement of pH in the rat epididymis in vivo. *J Reprod Fertil* 1978, *52*. 333-335.

47. J. Matulis, R. Slizys, On some characteristics of cathodic processes in nickel electrodeposition. *Electrochimica Acta* 1964, *9*. 1177-1188.

48. S. A. M. Marzouk, S. Ufer, R. P. Buck, T. A. Johnson, L. A. Dunlap, W. E. Cascio, Electrodeposited Iridium Oxide pH Electrode for Measurement of Extracellular Myocardial Acidosis during Acute Ischemia. *Analytical Chemistry* 1998, *70*. 5054-5061.

49. P. VanHoudt, Z. Lewandowski, B. Little, Iridium oxide pH microelectrode. *Biotechnology and Bioengineering* 1992, *40*. 601-608.

50. M. L. Hitchman, S. Ramanathan, Potentiometric determination of proton activities in solutions containing hydrofluoric acid using thermally oxidized iridium electrodes. *Analyst* 1991, *116*. 1131-1133.

51. T. Katsube, I. Lauks, J. N. Zemel, pH-sensitive sputtered iridium oxide films. *Sensors and Actuators* 1981, *2*. 399-410.

52. I. Lauks, M. F. Yuen, T. Dietz, Electrically free-standing IrOitx thin film electrodes for high temprature, corrosive environment pH sensing. *Sensors and Actuators* 1983, *4*. 375-379.

53. J. Joseph, H.-O. L. Kim, S. Oh, In Situ Electrochemical Sensor for Measurement in Nonconductive Liquids. *Journal of The Electrochemical Society* 1993, *140*. L33-L34.

54. A. N. Bezbaruah, T. C. Zhang, Fabrication of Anodically Electrodeposited Iridium Oxide Film pH Microelectrodes for Microenvironmental Studies. *Analytical Chemistry* 2002, *74*. 5726-5733.

55. E. Kinoshita, F. Ingman, G. Edwall, S. Thulin, S. Glab, Polycrystalline and monocrystalline antimony, iridium and palladium as electrode material for pH-sensing electrodes. *Talanta* 1986, *33*. 125-134.

56. S. Ardizzone, A. Carugati, S. Trasatti, Properties of thermally prepared iridium dioxide electrodes. *Journal of Electroanalytical Chemistry* 1981, *126*. 287-292.

57. M. Blouin, D. Guay, Activation of Ruthenium Oxide, Iridium Oxide, and Mixed Ru[sub x]Ir[sub 1 - x] Oxide Electrodes during Cathodic Polarization and Hydrogen Evolution. *Journal of The Electrochemical Society* 1997, *144*. 573-581.

58. J. Juodkazytė, B. Šebeka, I. Valsiunas, K. Juodkazis, Iridium Anodic Oxidation to Ir(III) and Ir(IV) Hydrous Oxides. *Electroanalysis* 2005, *17*. 947-952.

59. K. Kinoshita, M. J. Madou, Electrochemical Measurements on Pt, Ir, and Ti Oxides as pH Probes. *Journal of The Electrochemical Society* 1984, *131*. 1089-1094.

60. M. L. Hitchman, S. Ramanathan, Thermally grown iridium oxide electrodes for pH sensing in aqueous environments at 0 and 95°C. *Analytica Chimica Acta* 1992, *263*. 53-61.

61. P. J. Kinlen, J. E. Heider, D. E. Hubbard, A solid-state pH sensor based on a Nafion-coated iridium oxide indicator electrode and a polymer-based silver chloride reference electrode. *Sensors and Actuators B: Chemical* 1994, *22*. 13-25.

62. T. Pauporté, D. Aberdam, J.-L. Hazemann, R. Faure, R. Durand, X-ray absorption in relation to valency of iridium in sputtered iridium oxide films. *Journal of Electroanalytical Chemistry* 1999, *465*. 88-95.

63. L. D. Burke, J. K. Mulcahy, D. P. Whelan, Preparation of an oxidized iridium electrode and the variation of its potential with pH. *Journal of Electroanalytical Chemistry* 1984, *163*. 117-128.

64. A. Kapalka, S. Fierro, Z. Frontistis, A. Katsaounis, O. Frey, M. Koudelka, C. Comninellis, K. M. Udert, Electrochemical behaviour of ammonia () on electrochemically grown anodic iridium oxide film (AIROF) electrode. *Electrochemistry Communications* 2009, *11*. 1590-1592.

65. H. Suzuki, T. Hirakawa, S. Sasaki, I. Karube, An integrated module for sensing pO2, pCO2, and pH. *Analytica Chimica Acta* 2000, *405*. 57-65.

66. L. D. Burke, D. P. Whelan, A voltammetric investigation of the charge storage reactions of hydrous iridium oxide layers. *Journal of Electroanalytical Chemistry* 1984, *162*. 121-141.

67. W. Olthuis, M. A. M. Robben, P. Bergveld, M. Bos, W. E. van der Linden, pH sensor properties of electrochemically grown iridium oxide. *Sensors and Actuators B: Chemical* 1990, *2*. 247-256.

68. M. L. Hitchman, S. Ramanathan, Evaluation of iridium oxide electrodes formed by potential cycling as pH probes. *Analyst* 1988, *113*. 35-39.

69. G. Binnig, H. Rohrer, C. Gerber, E. Weibel, Surface Studies by Scanning Tunneling Microscopy. *Physical Review Letters* 1982, *49*. 57.

70. G. Binnig, H. Rohrer, C. Gerber, E. Weibel, Tunneling through a controllable vacuum gap. *Applied Physics Letters* 1982, *40*. 178-180.

71. G. Binnig, C. F. Quate, C. Gerber, Atomic Force Microscope. *Physical Review Letters* 1986, *56*. 930.

72. G. Meyer, N. M. Amer, Novel optical approach to atomic force microscopy. *Applied Physics Letters* 1988, *53*. 1045-1047.

73. Q. Zhong, D. Inniss, K. Kjoller, V. B. Elings, Fractured polymer/silica fiber surface studied by tapping mode atomic force microscopy. *Surface Science* 1993, *290*. L688-L692.

74. A. J. Bard, F. R. F. Fan, J. Kwak, O. Lev, Scanning electrochemical microscopy. Introduction and principles. *Analytical Chemistry* 1989, *61*. 132-138.

75. R. C. Engstrom, M. Weber, D. J. Wunder, R. Burgess, S. Winquist, Measurements within the diffusion layer using a microelectrode probe. *Analytical Chemistry* 1986, *58*. 844-848.

76. H. Y. Liu, F. R. F. Fan, C. W. Lin, A. J. Bard, Scanning electrochemical and tunneling ultramicroelectrode microscope for high-resolution examination of electrode surfaces in solution. *Journal of the American Chemical Society* 1986, *108*. 3838-3839.

77. A. E. Martin, et al., Scanning electrochemical microscopy: principles and applications to biophysical systems. *Physiological Measurement* 2006, *27*. R63.

78. A. J. Bard, F.-R. F. Fan, D. T. Pierce, P. R. Unwin, D. O. Wipf, F. Zhou, Chemical Imaging of Surfaces with the Scanning Electrochemical Microscope. *Science* 1991, *254*. 68-74.

79. J. Kwak, A. J. Bard, Scanning electrochemical microscopy. Theory of the feedback mode. *Analytical Chemistry* 1989, *61*. 1221-1227.

80. J. L. Fernández, A. J. Bard, Scanning Electrochemical Microscopy. 47. Imaging Electrocatalytic Activity for Oxygen Reduction in an Acidic Medium by the Tip Generation−Substrate Collection Mode. *Analytical Chemistry* 2003, *75*. 2967-2974.

81. C. Lee, J. Kwak, F. C. Anson, Application of scanning electrochemical microscopy to generation/collection experiments with high collection efficiency. *Analytical Chemistry* 1991, *63*. 1501-1504.

82. C. Kranz, G. Friedbacher, B. Mizaikoff, A. Lugstein, J. Smoliner, E. Bertagnolli, Integrating an Ultramicroelectrode in an AFM Cantilever: Combined Technology for Enhanced Information. *Analytical Chemistry* 2001, *73*. 2491-2500.

83. J. V. Macpherson, P. R. Unwin, Combined Scanning Electrochemical−Atomic Force Microscopy. *Analytical Chemistry* 2000, *72*. 276-285.

84. J. Abbou, C. Demaille, M. Druet, J. Moiroux, Fabrication of Submicrometer-Sized Gold Electrodes of Controlled Geometry for Scanning Electrochemical-Atomic Force Microscopy. *Analytical Chemistry* 2002, *74*. 6355-6363.

85. D. P. Burt, N. R. Wilson, J. M. R. Weaver, P. S. Dobson, J. V. Macpherson, Nanowire Probes for High Resolution Combined Scanning Electrochemical Microscopy − Atomic Force Microscopy. *Nano Letters* 2005, *5*. 639-643.

86. R. J. Fasching, Y. Tao, F. B. Prinz, Cantilever tip probe arrays for simultaneous SECM and AFM analysis. *Sensors and Actuators B: Chemical* 2005, *108*. 964-972.

87. J. V. Macpherson, P. R. Unwin, Noncontact Electrochemical Imaging with Combined Scanning Electrochemical Atomic Force Microscopy. *Analytical Chemistry* 2001, *73*. 550-557.

88. A. Davoodi, J. Pan, C. Leygraf, S. Norgren, In Situ Investigation of Localized Corrosion of Aluminum Alloys in Chloride Solution Using Integrated EC-AFM/SECM Techniques. *Electrochemical and Solid-State Letters* 2005, *8*. B21-B24.

89. C. Kranz, A. Kueng, A. Lugstein, E. Bertagnolli, B. Mizaikoff, Mapping of enzyme activity by detection of enzymatic products during AFM imaging with integrated SECM-AFM probes. *Ultramicroscopy* 2004, *100*. 127-134.

90. A. Kueng, C. Kranz, A. Lugstein, E. Bertagnolli, B. Mizaikoff, Integrated AFM–SECM in Tapping Mode: Simultaneous Topographical and Electrochemical Imaging of Enzyme Activity. *Angewandte Chemie International Edition* 2003, *42*. 3238-3240.

91. A. Kueng, C. Kranz, A. Lugstein, E. Bertagnolli, B. Mizaikoff, AFM-Tip-Integrated Amperometric Microbiosensors: High-Resolution Imaging of Membrane Transport. *Angewandte Chemie* 2005, *117*. 3485-3488.

92. A. Kueng, C. Kranz, B. Mizaikoff, A. Lugstein, E. Bertagnolli, Combined scanning electrochemical atomic force microscopy for tapping mode imaging. *Applied Physics Letters* 2003, *82*. 1592.

93. A. Lugstein, E. Bertagnolli, C. Kranz, A. Kueng, B. Mizaikoff, Integrating micro- and nanoelectrodes into atomic force microscopy cantilevers using focused ion beam techniques. *Applied Physics Letters* 2002, *81*. 349.

94. H. Shin, P. J. Hesketh, B. Mizaikoff, C. Kranz, Batch Fabrication of Atomic Force Microscopy Probes with Recessed Integrated Ring Microelectrodes at a Wafer Level. *Analytical Chemistry* 2007, *79*. 4769-4777.

95. H. Shin, P. J. Hesketh, B. Mizaikoff, C. Kranz, Development of wafer-level batch fabrication for combined atomic force-scanning electrochemical microscopy (AFM-SECM) probes. *Sensors and Actuators B: Chemical* 2008, *134*. 488-495.

96. T. Akiyama, M. R. Gullo, N. F. De Rooij, A. Tonin, H.-R. Hidber, P. L. T. M. Frederix, A. Engel, U. Staufer, Development of insulated conductive probes with platinum silicide tips for atomic force microscopy in cell biology. *Japanese Journal of Applied Physics, Part 1* 2004, *43*. 3865-3867.

97. P. S. Dobson, J. M. R. Weaver, M. N. Holder, P. R. Unwin, J. V. Macpherson, Characterization of Batch-Microfabricated Scanning Electrochemical-Atomic Force Microscopy Probes. *Analytical Chemistry* 2004, *77*. 424-434.

98. Y. Hirata, S. Yabuki, F. Mizutani, Application of integrated SECM ultra-micro-electrode and AFM force probe to biosensor surfaces. *Bioelectrochemistry* 2004, *63*. 217-224.

3 Improvement of the fabrication of AFM-SECM probes with integrated frame electrodes

The main objective of this chapter is to establish an efficient, reproducible and performance-optimized fabrication process of AFM tips with integrated sub-microelectrodes. The fabrication procedures starting from commercial AFM cantilevers for the fabrication of AFM-SECM probes are introduced and critical steps are described. Also, an evaluation of plasma-deposited fluorocarbon films as insulating materials is discussed. Cyclic voltammetry was used for electrochemical characterization and imaging with these combined AFM-SECM probes is shown.

3.1 Motivation

Since combined AFM-SECM probes with recessed electrodes have been introduced by Kranz et al.[1], this combined scanning probe technique has developed into a promising tool providing simultaneous topographical and electrochemical surface information[2-10]. The fabrication of the combined probes is based on modifications starting from commercially available AFM cantilevers using processes such as metal deposition, insulation steps and focused ion beam (FIB) milling. As these processes are not performed at the wafer level, the individual silicon nitride cantilevers are modified in small batches of 15 - 20 cantilevers with metal and consecutively with insulation layer, before the electrodes are individually exposed by FIB milling. The performance of the

AFM-SECM probes is influenced by the quality of the individual steps. Therefore, establishing efficient, reproducible fabrication for reliable measurements is necessary to extend the scope of applications for combined AFM-SECM probes.

In particular, when silicon nitride is used as insulation layer, it is required to optimize the insulation process as combined probes with silicon nitride show a tendency of electrical leakage and/or bending of the AFM cantilever. Both issues are very critical as leakage current disturbs electrochemical measurements and bending of the AFM cantilever obstructs the optical readout of the deflection during AFM operation. Hence, straight AFM-SECM cantilevers with an electrically perfect insulation are a prerequisite for proper performance.

In addition, the thickness of the insulation layer plays a significant role and a thin insulation layer is desired. From an AFM imaging perspective, a thin insulation layer reduces the possibility that the insulation is in contact with the sample surface when a sample with a high surface roughness is imaged or when the re-shaped AFM tip is short in comparison to the thickness of the insulation layer in order to achieve high resolution electrochemical imaging. As the thickness of the insulation layer is defining the RG value, which was described in section 2.2.2, the insulation layer has to be controlled. It is known that small RG values of SECM probes have enhanced steady-state currents with diffusion of electroactive species from behind the electrode plane.

Of all processes involved in the fabrication of the AFM-SECM probes, the metal and insulating layer deposition steps are considered critical as they determine stress of cantilever, electrical insulation quality, and thickness of insulation sheath. This chapter

describes the optimization of these fabrication processes in respect to improving the overall reproducibility and quality of the combined AFM-SECM probes.

3.1.1 Plasma-deposited fluorocarbon thin film

Typically, PECVD (plasma-enhanced chemical vapor deposition) Si_xN_y and/or SiO_2 thin films, which are standard materials in integrated circuits (ICs) fabrication or microelectromechanical systems (MEMS), are used for the insulation of AFM-SECM probes. As an alternative insulation layer, plasma-deposited fluorocarbon thin films using pentafluoroethane (PFE, CF_3CHF_2) as gas precursor were also applied. Fluorocarbon films are promising as insulating layers improving the performance of AFM-SECM probes as such films have high electrical resistance, chemical inertness, biocompatibility and conformal step coverage[11]. Also, the thermal stability[12], electrical property[13] and the involved plasma chemistry[14] have been extensively studied. One of the most attractive facts is that these thin films can be obtained at a relatively low temperature (approx. 120 ºC.), which is crucial since the AFM-SECM cantilevers are composed of metal and dielectric multilayers resulting in the tendency to bend at high temperature.

Summarizing, fluorocarbon films are promising as insulation material for AFM-SECM probes, as they fulfill most of the previously described requirements of an insulation layer providing small RG values.

3.2 Experimental

3.2.1 Fabrication of AFM-SECM probes

AFM-SECM probes were fabricated by a series of standard semiconductor processes[1]. This section provides a brief introduction of the fabrication procedure. **Figure 3.1** shows a schematic illustration of the fabrication process flow. Triangular-shaped commercially available Si_xN_y cantilevers (Veeco, Woodbury, NY) were utilized as basis for the AFM-SECM probes. In a first step (**Figure 3.1A**), the reflective coating on the backside of the cantilevers, which has 60 nm thick Au and 10 nm thick Cr for adhesion according to the manufacturer, were removed by Au etchant (GE-8110, Transene, Danvers, MA) and Cr etchant (CR7-S, Cyantek, Fremont, CA), respectively. Then, the cantilevers were cleaned in piranha solution (H_2SO_4 from Fisher Scientific, Pittsburgh, PA; 30 % H_2O_2 from JT Baker, Phillipsburg, NJ; ratio 4:1) at 120 ºC for 10 min prior to the metal deposition. Subsequently, 10 nm thick Ti layer for adhesion and 100 – 150 nm thick Au layer was deposited using a DC sputter system (CVC DC sputterer; power = 350 W for Ti, 2500 W for Au) (**Figure 3.1B**). A shadow mask was utilized for the metallization, and a conductive line connecting the electrode and the contact pad was patterned (details are described in the next section). The third step is the insulation of the probes including the cantilever chip made of glass (**Figure 3.1C**). In this thesis, either sandwiched layers of PECVD Si_xN_y-SiO_2 or PFE films were used for insulation. After the insulation step, FIB milling (Nova™ 200 NanoLab or Quanta™ 200 3D DualBeam™ systems, FEI, Hillsboro, OR) was performed to expose a frame-shaped electroactive area and to reshape the AFM tip as shown in **Figure 3.1D**. A bitmap of the desired milling shape was generated and uploaded into the FIB milling software used as a digital milling mask. Thereby, the number of FIB milling steps is significantly reduced[7]. The FIB milling was performed in two steps. In a first bitmap-assisted milling step, the insulation

layer and the metal layer were partly removed using a bi-triangular milling mask. In the second step, the probe was rotated by 90º in respect to the first milling step and the tip milling was repeated using a similar digital mask. After each milling step, a FIB cleaning

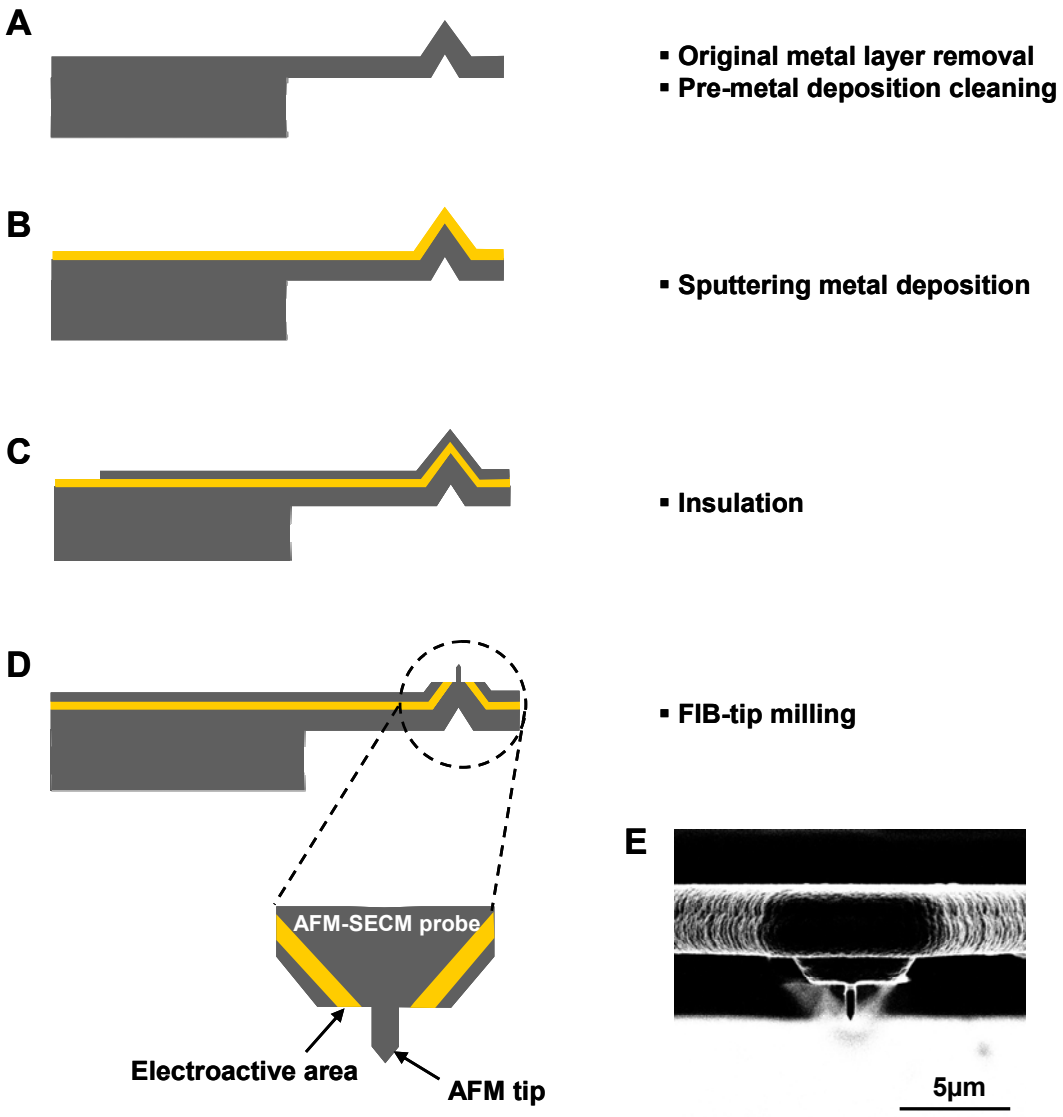

Figure 3.1 Schematic of the fabrication process flow for AFM-SECM probes fabrication.

step was executed for removal of residual material possibly remaining on the electrode surface. **Figure 3.1E** shows a SEM image of the AFM-SECM probe after the FIB milling step.

3.2.1.1 Metallization

In the metallization step (**Figure 3.1B**), depositing the metal layer in a structured fashion instead of coating the whole probe including the cantilever chip is crucial. This can significantly reduce possible electrical leakage currents as no conductive area can be exposed during handling the cantilever (for example mounting). Particularly, the edge of the cantilever chips of the conventional AFM cantilevers, which are used as basis for AFM-SECM probes have staircase-like edges, which is a prone source of leakage current after the insulation process. For this reason, a shadow mask was fabricated and used in the metallization step. As shown in **Figure 3.2**, Au metal lines were patterned to connect the tip through the cantilever arm with the contact pad using the shadow mask. The shadow mask was made of stainless steel and was micromachined utilizing an IR laser (Resonetics, Nashua, NH). The design of the shadow mask was created with a graphic software (Autocad 2004, Autodesk Inc., San Rafael, CA). The shadow mask was designed so that 15 cantilevers can be metalized in one run for improving the efficiency of the fabrication process.

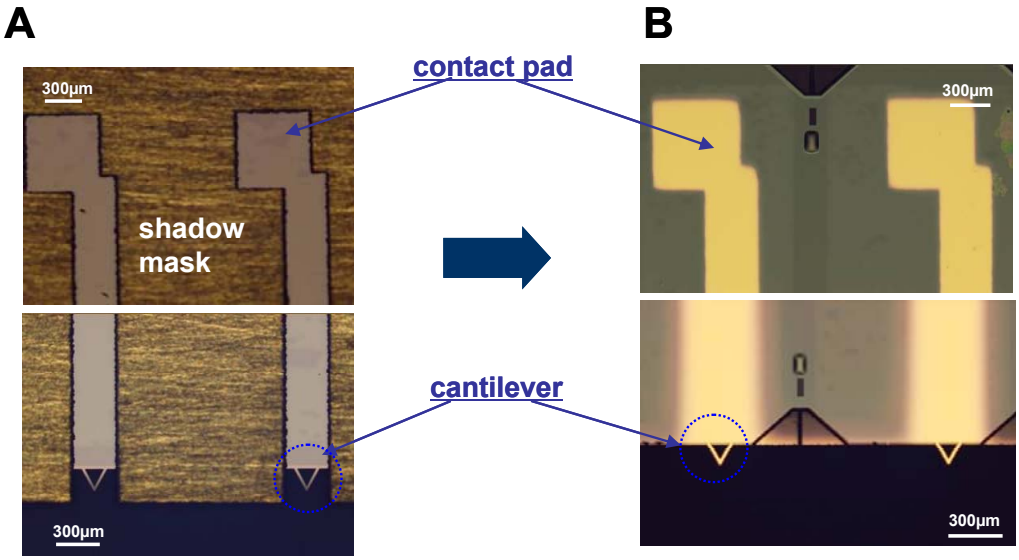

Figure 3.2 Optical micrographs for (A) aligned shadow mask and cantilevers before Au deposition and (B) cantilevers after the deposition process.

3.2.1.2 Insulation

Alternatively to the described insulation materials such as sandwiched layers of PECVD Si_xN_y and SiO_2, Parylene C has been used as insulation layer[3,15]. Parylene C can be deposited at room temperature; hence it does not induce noticeable thermal stress on AFM-SECM probes, which avoids bending effects. However, the mechanical and chemical properties of PECVD Si_xN_y and SiO_2 sandwiched layers are superior for AFM-SECM applications where potentials higher than 1.5 V have to be applied or measurements are performed in chemically harsh environments.

For the deposition of PECVD Si_xN_y and SiO_2 sandwiched layers, the temperature was the most critical parameter. As shown in **Figure 3.3**, bending of the cantilever was observed after PECVD Si_xN_y and SiO_2 layers (Unaxis PECVD; pressure = 1100 mTorr,

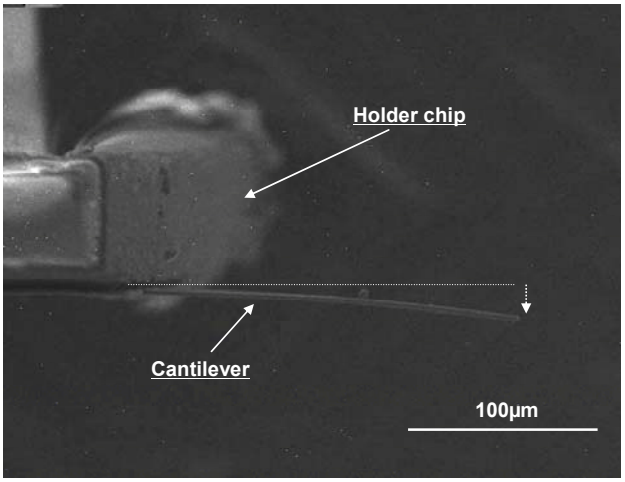

Figure 3.3 SEM image (side view) of a bent cantilever.

SiH_4 = 200 sccm, NH_3 = 8 sccm, temperature = 300 ºC, power = 50 W for Si_xN_y; pressure = 900 mTorr, SiH_4 = 400 sccm, NO_2 = 900 sccm, temperature = 300 ºC, power = 25 W for SiO_2) were deposited at typical temperatures ranging from 200 – 350 ºC[16]. Even a small degree of bending interferes with AFM operation as described previously. Since the metal layer is only deposited onto one side of the cantilever, the mismatch of the thermal expansion coefficients of the layered gold and silicon nitride material leads to bending of the cantilever at higher temperature.

The parameters used to obtain AFM-SECM probes with sandwiched layers of PECVD Si_xN_y and SiO_2 as insulation are tabulated (**Table 3.1**). The deposition was performed as alternating multilayer process of Si_xN_y-SiO_2-Si_xN_y-SiO_2-Si_xN_y. Stainless steel alligator clips (Mueller Electric, Akron, OH) were used to hold the individual probes. After the deposition, the substrate temperature was slowly cooled down to 100 ºC prior to venting the chamber.

Table 3.1 Summary of parameters used for deposition of PECVD Si_xN_y and SiO_2 insulation.

	Si_xN_y	SiO_2
Power (W)	50	25
Gas (sccm)	SiH_4 - 200 NH_3 - 8 He - 560 N_2 - 150	SiH_4 - 400 N_2O - 900
Pressure (mTorr)	1100	900

3.2.1.3 PFE insulation

Plasma deposition of PFE films for insulating AFM-SECM probes was obtained at the School of Chemical and Biomolecular Engineering (Georgia Institute of Technology) in collaboration with Dr. Dennis W. Hess.

Prior to the PFE insulation, AFM-SECM probes were cleaned in an UV/ozone chamber (BioForce Nanoscience, Ames, IA) for 20 min. Stainless steel alligator clips (Mueller Electric, Akron, OH) were used as holders for the probes to be processed in the PFE chamber.

For the PFE deposition, plasma reactor reagents include pentafluoroethane monomer gas (Dupont, Wilmington, DE; N4 grade, 99.99 %), argon carrier gas (Air products and Chemical Inc., Allentown, PA; Ultra High Purity, 99.99 %), nitrogen (Airgas Inc., Radnor, PA; Ultra High Purity, 99.999 %) and oxygen (Airgas Inc., Radnor, PA; Ultra Pure Carrier, 99.996 %).

Figure 3.4 shows a schematic of the experimental set-up[17]. A six-inch parallel plate plasma reactor was used for the deposition of PFE films. The bottom electrode was heated to approx. 112 ºC using cartridge heaters (Omegalux CIR 2015, Omega

Engineering Inc., Stamford, CT); the temperature was monitored by a type K thermocouple controlled with a temperature controller (Syskon, RKC Instrument Inc., Southbend, IN). 120 W RF (13.56 MHz) power (HF-300, ENI Power Systems, Rochester, NY) was applied to the top electrode and a matching network (Heathkit SA-2060A, Heath Company, Benton Harbor, MI) was connected for minimizing the reflected power. The chamber pressure was controlled with a pressure gauge (Varian Inc., Lexington, MA), and a rotary vacuum pump (Alcatel 2063 C, Alcatel, Annecy, France). The base pressure was set to 20 mTorr and the PFE film was deposited at approx. 1 Torr (Reaction gases were PFE monomer (20 sccm) and Ar (75 sccm)). Prior to the deposition, the oxygen plasma cleaning was performed at approx. 1 Torr (Reaction gas was oxygen (75 sccm)) for 1 min.

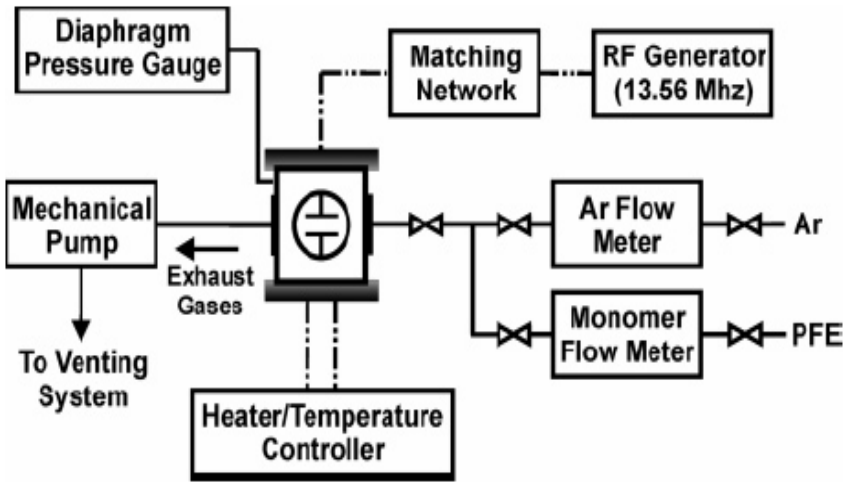

Figure 3.4 Schematic of the PFE insulation set-up (adapted from[17]).

3.2.2 Electrochemical characterization

CVs were performed for electrochemical characterization of the fabricated AFM-SECM probes. (Bi)potentiostats used throughout this thesis were models CHI660A, CHI842B and CHI832A from CH Instruments (Austin, TX). CVs were recorded in aqueous solutions containing 10mM potassium ferrocyanide(II) trihydrate ($Fe(CN)_6^{4-}$, (Sigma-Aldrich, St. Louis, MO), and 0.5 M potassium chloride (KCl, Sigma-Aldrich, St. Louis, MO) as a supporting electrolyte. A saturated calomel electrode (SCE) served as the reference electrode and a platinum wire was used as counter electrode. All solutions were prepared using deionized water with a resistance of 18.2 MΩ cm at 25 °C obtained from a water purification system (Millipore, Billerica, MA).

3.2.3 Simultaneous AFM-SECM imaging

The schematic of the set-up for simultaneous AFM-SECM imaging is shown in **Figure 3.5**. A model 5500 AFM from Agilent Technologies (Chandler, AZ) was used for all AFM and AFM-SECM experiments. The AFM features a top-down configuration, in which the scanning elements and electronics are isolated from the imaging environment. Also, the AFM-SECM probe and the sample area can be monitored through an optical microscope. For reduction of possible environmental vibration and electromagnetic noise during the measurement, the AFM was placed in a vibration isolation chamber (Agilent

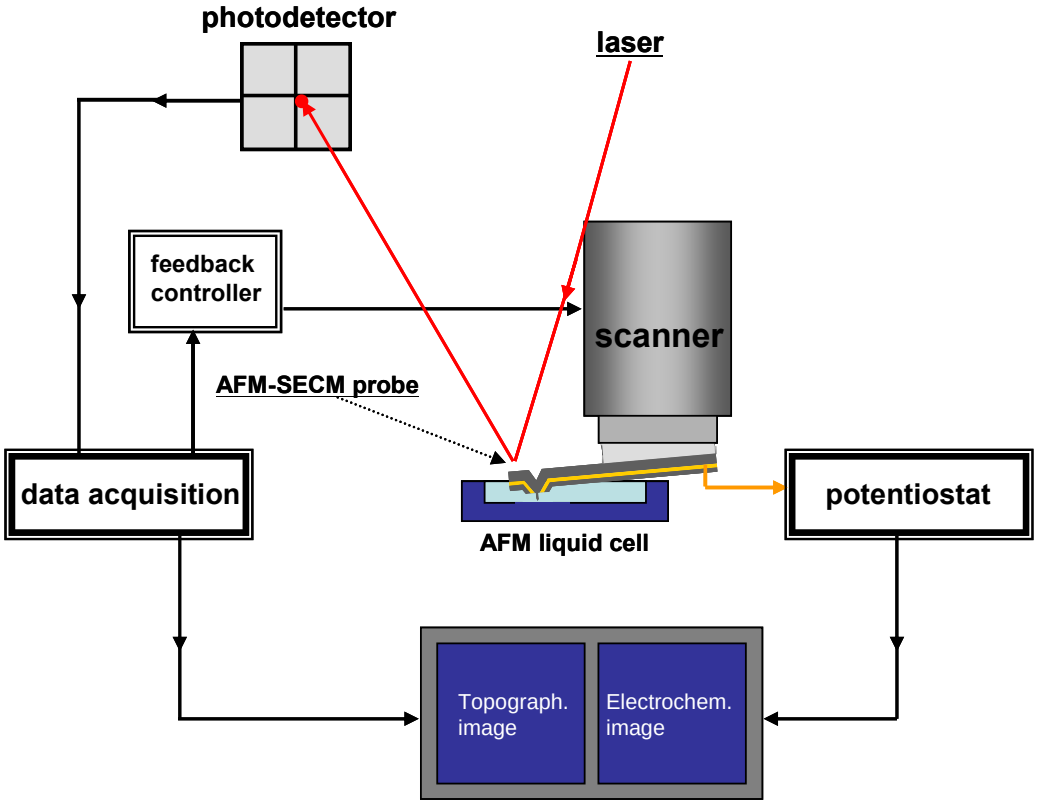

Figure 3.5 Schematic of a combined AFM-SECM set-up.

Technologies, Chandler, AZ), and additionally in a Faraday cage (home-built). Measurements were performed using an AFM liquid cell equipped with a three electrode system (**Figure 3.6**), with the AFM-SECM probe serving as the working electrode (WE), a chloridized silver wire as AgQRE (Silver quasi reference electrode) and a platinum

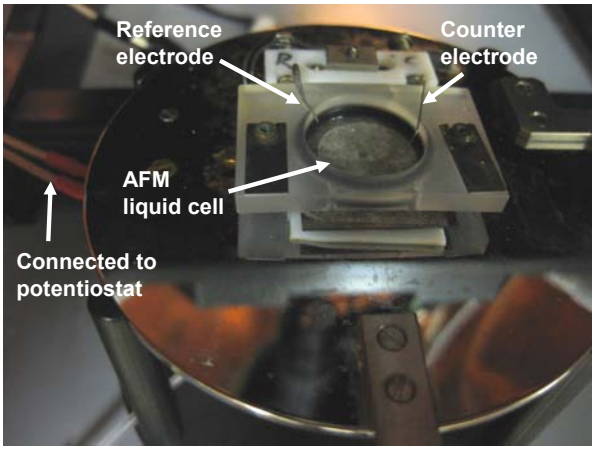

Figure 3.6 Photograph of an AFM liquid cell showing the reference and counter electrode.

wire as reference and counter electrode, respectively. AFM-SECM probes were mounted on nose cone assemblies (Agilent Technologies, Chandler, AZ) by gluing; the nose cone (**Figure 3.7**) is then attached to the scanner. The electrical connection of AFM- SECM probes to an external potentiostat were established using shielded cables (New England

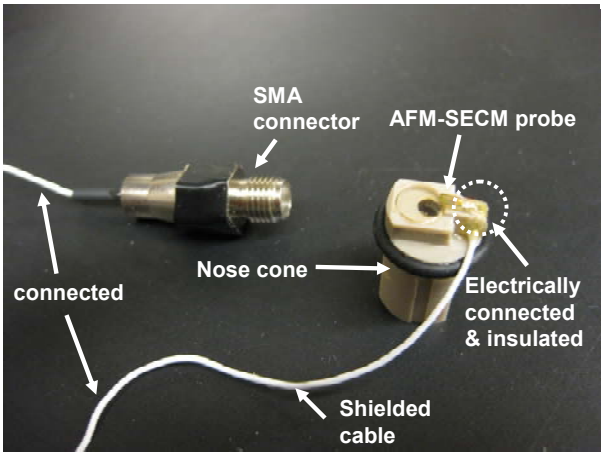

Figure 3.7 Photograph of a nose cone with mounted AFM-SECM probe showing the electrical connection cable.

Wire Technologies, Lisbon, NH) with SMA connectors (Pasternack, Irvine, CA). Subsequently, the contact pad area of AFM-SECM probes were insulated using insulation varnish (Electrolube, UK). The output signal of the potentiostat was read into an AD channel of the AFM controller for real-time correlation of the electrochemical and the AFM data. Post-processing of AFM images was performed with the PicoScan 5.3.3 software (Agilent Technologies, Chandler, AZ).

3.3 Results and discussion

3.3.1 Scanning electron microscopy

The typical thickness of PFE-insulated AFM-SECM probes was approx. 300 – 400 nm. **Figure 3.8** shows a representative SEM image of a PFE-insulated AFM-SECM probe after exposure of the electroactive area by FIB milling. A small variation in the thickness of insulation was observed after the tip milling. The thicknesses of the

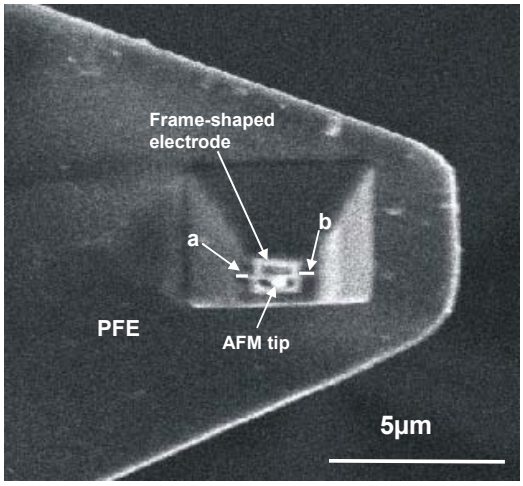

Figure 3.8 SEM image of a PFE-insulated AFM-SECM probe after exposure of an electrode by FIB milling.

insulation was measured at a and b as marked in **Figure 3.8**. The thickness of insulation measured at b was approx. 400 nm, while it was approx. 300 nm at a. The thickness variation observed may be attributed to the orientation of the probe surface to the ion bombardment direction during the deposition. An overall variation of the thickness was also observed at different samples. Since the PFE deposition is very sensitive to temperature, a slight temperature gradient in the chamber leads to thickness variations at different samples, which were coated during one run. However, these variations were in a small range of several tens of nanometers.

3.3.2 Electrochemical characterization

Cyclic voltammograms were recorded before and after the FIB milling step for electrochemical characterization of PFE-insulated AFM-SECM probes. Representative

CVs are shown in **Figure 3.9**. From the CV obtained before the tip milling, a charging current of only approx. 8pA was observed, which is an indication of a good electrical insulation of the probe. Despite a presence of slight variation in thickness of the insulation, insulation with PFE is applicable to AFM-SECM probes. After FIB milling, the probe was again characterized by CV. The CV reveals a sigmoidal shape with a corresponding steady-state faradaic current of approx. 2.3 nA, which is in the same order of magnitude as the theoretical current value of 1.4 nA, obtained utilizing an analytical expressions derived for ring electrodes[1]. The discrepancy may be caused by high density

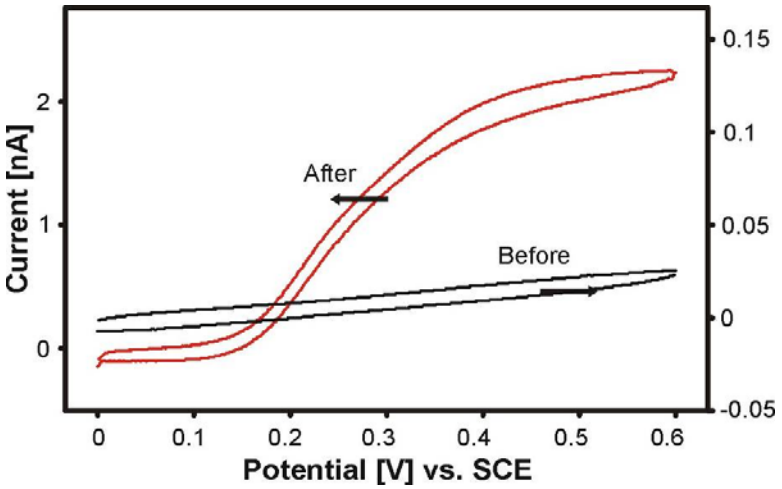

Figure 3.9 CVs recorded at PFE-insulated AFM-SECM probe before and after FIB milling in 10 mM $Fe(CN)_6^{4-}$ solution containing 0.5 M KCl as supporting electrolyte. CVs were obtained with a scan rate of 0.05 and 0.1 V s^{-1}. The frame edge length was approx. 1.28 µm[10].

effects at corners of frame-shaped electrodes, which is not considered in the theoretical approximation.

3.3.3 AFM-SECM imaging

In order to demonstrate the performance of AFM-SECM probes, simultaneous AFM contact mode and electrochemical feedback mode images were recorded.

3.3.3.1 Imaging with PFE-insulated AFM-SECM probe

Approx. 10 nm thick Ti and 100 nm thick Au-coated glass slide having insulating (glass) and conductive (Au) features were prepared using bitmap-assisted FIB milling as a test sample for an imaging experiment (**Figure 3.10**).

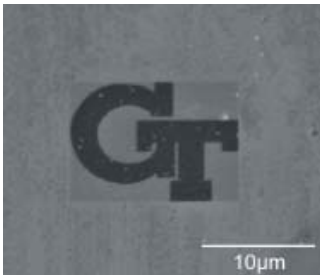

Figure 3.10 SEM image of the test substrate used for the imaging experiment with a PFE-insulated AFM-SECM probe.

Figure 3.11 shows simultaneously obtained AFM-SECM images obtained with a PFE-insulated AFM-SECM probe. The probe was scanned across the surface of the substrate, which was prepared by bitmap-assisted FIB milling (**Figure 3.10**). The tip-

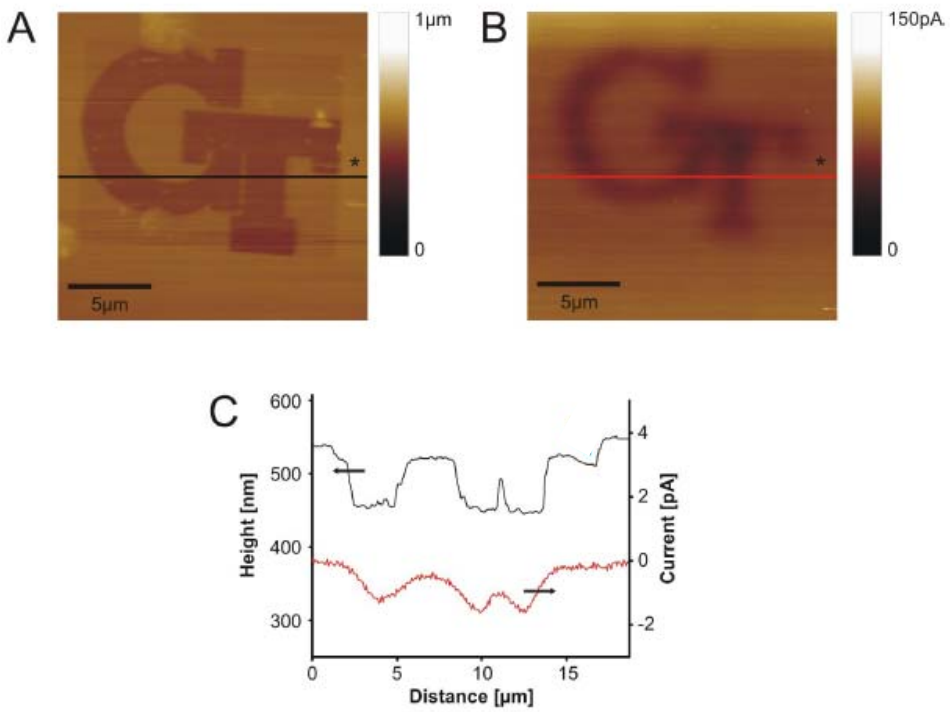

Figure 3.11 Simultaneously obtained AFM-SECM imaging with PFE-insulated AFM-SECM probe. (A) Topography, (B) simultaneously recorded current image with a integrated frame electrode (electrode frame length: approx. 1.6 µm). (C) The cross-sectional view of lines marked in (A) and (B). The image was recorded in contact mode at a rate of 0.36 line s^{-1} (original scan size : 25 x 25 μm^2) and the tip-integrated electrode was held at 0.6 V (vs. AgQRE) in 10 mM $Fe(CN)_6^{4-}$ solution containing 0.5 M KCl[10].

integrated electrode was biased at 0.6 V (vs. AgQRE) in 10 mM $Fe(CN)_6^{4-}$. As clearly visible in the image presented in **Figure 3.11**, the current was elevated due to positive feedback at the surface of conductive (Au) features and it is decreased at the surface of insulating (glass) features. The patterns were clearly resolved in both the topography and

electrochemical image. Moreover, the cross-sectional view (**Figure 3.11C**) demonstrates excellent resolution of the electrochemical image.

3.3.3.2 Imaging with PECVD Si_xN_y-insulated AFM-SECM probe

Imaging experiments on a model sample were also performed with a PECVD Si_xN_y-insulated AFM-SECM probe. A micro-structured pattern consisting of a conductive Pt layer (300 nm thick) and an insulating silicon oxide pattern was prepared as a test sample (**Figure 3.12**). The experiments were conducted in an aqueous solution containing 0.01 M $Fe(CN)_6^{4-}$ as the redox mediator in 0.5 M KCl as the supporting electrolyte. The integrated electrode was held at 600 mV vs. the AgQRE electrode.

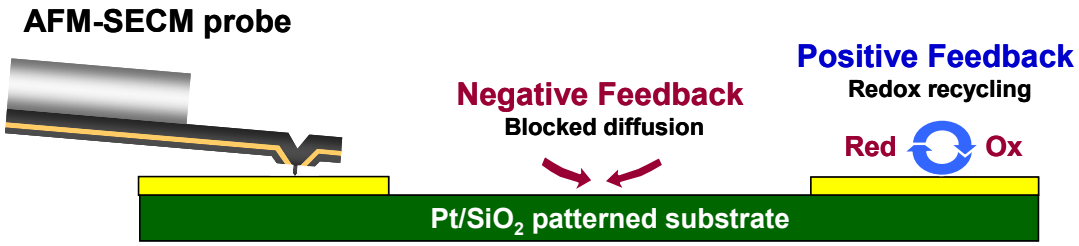

Figure 3.12 Schematic of the feedback mode imaging experiment.

The distance from the integrated electrode to the sample surface is determined by the length of the reshaped AFM tip (600 nm) during the imaging experiment. According to theory of the SECM feedback mode, if the tip is placed in close vicinity to the sample surface, the diffusion-limited steady-state current measured at the electrode is influenced

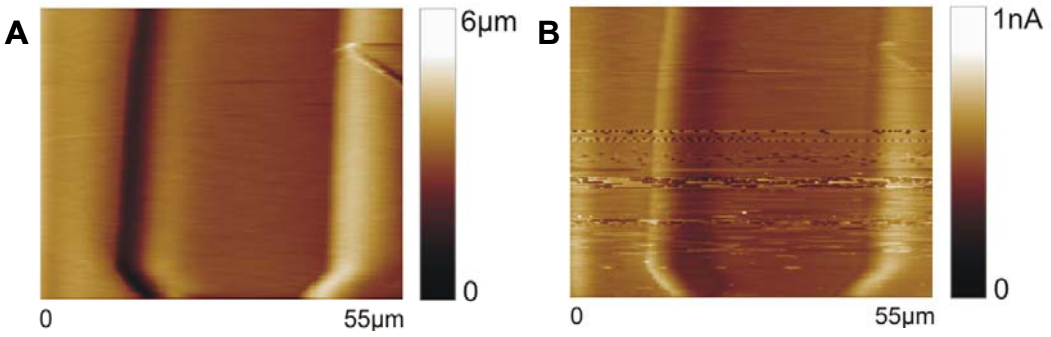

Figure 3.13 Combined AFM-SECM imaging: (A) topography of a Pt-SiO_2 micropatterned substrate imaged in AFM contact mode with a combined AFM-SECM probe. (B) Simultaneously recorded current image obtained with an integrated frame electrode (electrode frame length: 800 nm) biased at 0.6 V vs. AgQRE in 0.01 M $[Fe(CN)_6]^{4-}$ solution containing 0.5 M KCl.

by the properties of the surface. In feedback mode, the recorded current decreases compared to the steady-state current in bulk solution at the insulating features due to the hindrance of the hemispherical diffusion of the mediator towards the electrode. In contrast, conductive surface features result in an increased current due to recycling of the redox mediator as it is reduced at the surface. In **Figure 3.13**, the periodicity of the pattern evident in the electrochemical image (current response) corresponds well to the topographical features simultaneously obtained with the AFM tip during contact mode imaging[7].

3.4 Final remarks

For AFM-SECM probes with recessed frame electrodes, the fabrication steps were optimized in respect to metallization and insulation. The objective of this chapter

was improving the reproducibility in fabricating AFM-SECM probes ensuring electrically perfect insulation of the electroactive area, straight cantilevers and small RG values. For the metallization, a shadow mask made of stainless steel was designed and fabricated using IR laser micromachining. Sandwiched layers of PECVD Si_xN_y and SiO_2 and plasma-deposited PFE films were used and tested as insulation layers. For the sandwiched layers of PECVD Si_xN_y and SiO_2, AFM-SECM probes revealing straight cantilevers and excellent insulation characteristics were reproducibly obtained. The insulation thickness was in the range of 0.7 - 1.0 μm, which corresponds to RG values of approx. 5 - 8. Since RG values in a range of 5 - 20 are preferential[18], the obtained RG values fit well. In addition, AFM-SECM imaging was successfully performed at a Pt-SiO_2 micropatterned substrate and the simultaneously obtained topography and electrochemical images was in good agreement with SECM feedback theory. PFE thin films were also tested as very promising insulating layer for AFM-SECM probes. CVs were recorded for electrochemical characterization of PFE-insulated AFM-SECM probes and excellent insulating property was obtained. Moreover, this insulation property could be achieved at a thickness of approx. 400 nm, which corresponds to less than half of the thickness of PECVD Si_xN_y and SiO_2 layers. For both insulation strategies, the surface cleanliness of AFM-SECM probes in each fabrication steps is crucial. Particularly, optimizing the surface treatment strategy before the insulation step results in improved electrical insulation and adhesion of insulation layers.

3.5 References

1. C. Kranz, G. Friedbacher, B. Mizaikoff, A. Lugstein, J. Smoliner, E. Bertagnolli, Integrating an Ultramicroelectrode in an AFM Cantilever: Combined Technology for Enhanced Information. *Analytical Chemistry* 2001, *73*. 2491-2500.

2. C. Kranz, A. Kueng, A. Lugstein, E. Bertagnolli, B. Mizaikoff, Mapping of enzyme activity by detection of enzymatic products during AFM imaging with integrated SECM-AFM probes. *Ultramicroscopy* 2004, *100*. 127-134.

3. A. Kueng, C. Kranz, A. Lugstein, E. Bertagnolli, B. Mizaikoff, Integrated AFM–SECM in Tapping Mode: Simultaneous Topographical and Electrochemical Imaging of Enzyme Activity. *Angewandte Chemie International Edition* 2003, *42*. 3238-3240.

4. A. Kueng, C. Kranz, A. Lugstein, E. Bertagnolli, B. Mizaikoff, AFM-Tip-Integrated Amperometric Microbiosensors: High-Resolution Imaging of Membrane Transport. *Angewandte Chemie* 2005, *117*. 3485-3488.

5. A. Kueng, C. Kranz, B. Mizaikoff, A. Lugstein, E. Bertagnolli, Combined scanning electrochemical atomic force microscopy for tapping mode imaging. *Applied Physics Letters* 2003, *82*. 1592.

6. A. Lugstein, E. Bertagnolli, C. Kranz, A. Kueng, B. Mizaikoff, Integrating micro- and nanoelectrodes into atomic force microscopy cantilevers using focused ion beam techniques. *Applied Physics Letters* 2002, *81*. 349.

7. J.-S. Moon, H. Shin, B. Mizaikoff, C. Kranz, Bitmap-assisted focused ion beam fabrication of combined atomic force scanning electrochemical microscopy probes. *Journal of the Korean Physical Society* 2007, *51*. 920-924.

8. H. Shin, P. J. Hesketh, B. Mizaikoff, C. Kranz, Batch Fabrication of Atomic Force Microscopy Probes with Recessed Integrated Ring Microelectrodes at a Wafer Level. *Analytical Chemistry* 2007, *79*. 4769-4777.

9. H. Shin, P. J. Hesketh, B. Mizaikoff, C. Kranz, Development of wafer-level batch fabrication for combined atomic force-scanning electrochemical microscopy (AFM-SECM) probes. *Sensors and Actuators B: Chemical* 2008, *134*. 488-495.

10. J. Wiedemair, B. Balu, J.-S. Moon, D. W. Hess, B. Mizaikoff, C. Kranz, Plasma-Deposited Fluorocarbon Films: Insulation Material for Microelectrodes and Combined Atomic Force Microscopy−Scanning Electrochemical Microscopy Probes. *Analytical Chemistry* 2008, *80*. 5260-5265.

11. H. V. Jansen, J. G. E. Gardeniers, J. Elders, H. A. C. Tilmans, M. Elwenspoek, Applications of fluorocarbon polymers in micromechanics and micromachining. *Sensors and Actuators A: Physical* 1994, *41*. 136-140.

12. S. Agraharam, D. W. Hess, P. A. Kohl, S. A. B. Allen, Thermal Stability of Fluorocarbon Films Deposited from Pentafluoroethane/Argon Plasmas. *Journal of The Electrochemical Society* 2000, *147*. 2665-2670.

13. S. Agraharam, D. W. Hess, P. A. Kohl, S. A. B. Allen, Electrical Properties and Temperature-Humidity Studies of Fluorocarbon Films Deposited from Pentafluoroethane/Argon Plasmas. *Journal of The Electrochemical Society* 2001, *148*. F102-F107.

14. S. Agraharam, D. W. Hess, P. A. Kohl, S. A. B. Allen, Plasma chemistry in fluorocarbon film deposition from pentafluoroethane/argon mixtures. *Journal of Vacuum Science & Technology A: Vacuum, Surfaces, and Films* 1999, *17*. 3265-3271.

15. E. L. H. Heintz, C. Kranz, B. Mizaikoff, H.-S. Noh, P. J. Hesketh, A. Lugstein, E. Bertagnolli, Characterization of Parylene Coated Combined Scanning Probe Tips for In-Situ Electrochemical and Topographical Imaging. *Proceedings of the 2001 1st IEEE Conference on Nanotechnology. IEEE-NANO 2001 (Cat. No.01EX516), Maui, HI, USA, 2001//2001; IEEE; 346-351.* 2001.

16. M. J. Madou, Fundamentals of Microfabrication: The Science of Miniaturization, 2nd ed., Boca Raton, FL: CRC Press. 2002.

17. G. T. Dobbs, B. Balu, C. Young, C. Kranz, D. W. Hess, B. Mizaikoff, Mid-Infrared Chemical Sensors Utilizing Plasma-Deposited Fluorocarbon Membranes. *Analytical Chemistry* 2007, *79*. 9566-9571.

18. G. Wittstock, M. Burchardt, S. Pust, Y. Shen, C. Zhao, Scanning Electrochemical Microscopy for Direct Imaging of Reaction Rates. *Angewandte Chemie International Edition* 2007, *46*. 1584-1617.

4 Batch fabrication of AFM tip-integrated disk nanoelectrodes

This chapter describes the fabrication of disk nanoelectrodes integrated in AFM tips for combined AFM-SECM measurements. The disk electrodes were designed to have radii in the range of 50 – 100 nm, which enables an improved lateral resolution in SECM experiments. This developed fabrication scheme is based on a reproducible semi batch-fabrication process at a wafer level. Therefore, significantly reduced time and cost for the fabrication are additional advantageous aspects. The detailed process steps will be discussed. The combined AFM-SECM probes were electrochemically characterized and their performances were demonstrated by imaging model samples consisting of patterns of conductive and insulating features, such as a structured Au layer patterned on an insulating substrate.

4.1 Motivation

To obtain highly resolved information on electrochemical processes is a growing demand in numerous research fields. In fuel cell technology, as an example, spatially resolved evaluation of electrochemical activity at nanostructured material is the key in understanding the structure-activity relationship in fuel cell components such as catalyst films[1]. Also, in corrosion science electrochemical techniques providing laterally resolved information play a significant role in this area. For example, investigating high-

performance coatings and degradation mechanism of metals and alloys at the nanoscale strongly demands high spatial resolution capability of the electrochemical imaging technique[2]. Conventional electrochemical impedance spectroscopy (EIS) has been widely used to study macroscopic corrosion phenomena[3]. However, such macroscopic studies are intrinsically limited and focus on the final stage of corrosion activity, whereas the initial symptoms of corrosion are confined to microscopic surface areas. Conversely, a micro- or nanoscopic localized investigation of corrosion events at initial stage provides critical information on the corrosion initiation mechanisms. Also, in life sciences electrochemical techniques capable of providing information at the microscopic scale have attracted great interests. In cell biology, a variety of biological processes such as metabolic processes involve activities of cells, which are responsible for the basic functions of life. The activities of cells include growth, respiration, reproduction and cell communication with an extracellular environment and these activities can be sustained in isolated single cells. Therefore, electrochemical investigation of cellular processes at a single cell level provides better understanding of the complex biological processes[4].

4.1.1 High resolution SECM

SECM has gained considerable attention as an attractive technique providing insight in surface activity and surface-confined chemical reactions obtained during scanning a miniaturized electrode across the sample surface. The lateral resolution obtained in SECM measurements depends predominantly on the size of the electrode, the working distance between the electrode and the sample surface and the nature of the sample. The working distance is related to the size of the electrode, and positioning the

tip at an appropriate distance during a scanning experiments becomes a critical issue when SECM experiments are conducted with sub-micron-sized electrodes in order to obtain high resolution imaging[4]. The constant height mode, which is applied in conventional SECM experiments, is not suitable if tilted samples, samples with high topography or sub-micron electrodes are used for imaging. With decreasing size of the electrode, the distance between tip and surface has to be reduced (ideally, the distance should be smaller than the diameter of electrode to obtain an optimized resolution in the electrochemical image). For example, rough sample surfaces and even a slight tilt of the electrode to the surface have a significant impact, interfering with a precise scanning experiment in constant height mode. As a result, convolution of both activity and topographical contributions or crashing the tip into the surface may occur. Hence, a way of precisely controlling the distance between tip and sample surface is required.

As an alternative method to constant height imaging, constant-distance mode imaging is a very promising mode for positioning small electrodes in SECM experiments. A variety of constant-distance mode positioning for SECM have been reported[5-16]. The most prominent mode is using a shear-force-based feedback mechanism. In shear-force based positioning, the damping of a lateral vibration of a fiber-shaped SECM tip, is caused by hydrodynamic forces when the electrode is in close vicinity of the sample surface[8-10,12,15]. Read-out of the vibration damping was demonstrated using several different types of shear-force detection schemes such as optical[8,12], piezoelectric[10] or tuning-fork based detection[9,15]. Besides shear-force-based positioning, an impedance-based feedback[5,7] and combining SECM with complementary SPM techniques such as STM[16] and NSOM[14] has been reported. As the topographical resolution is dependent on

the size of the electrode, shear-force-based SECM cannot compete in resolution with scanning probe techniques. In addition, combinations with STM are limited to investigations of conductive surfaces. The most promising technique in hyphenated scanning probe techniques providing electrochemical information along with topographical information is the combination of SECM and AFM, which enables simultaneously recording electrochemical and topographical information with high spatial resolution at a controlled distance independent of the size of electrode[11, 13]. As described in section 2.2.3, the approaches to fabricate AFM-SECM probes can be basically categorized into two groups. The first approach focuses on defining an electrode at the apex of the AFM tip and therefore typically enables high resolution electrochemical imaging with small conical electrodes. For example, Burt et al.[6] used single-walled carbon nanotube AFM tips. By attaching the carbon nanotube to an AFM tip and consecutively coat the assembly with an Au layer and an insulating layer, an electrode with a few tenths of nanometer of active electrode with a fairly large insulation was achieved. However, this type of combined probe cannot provide the real-time combination of topographical and electrochemical surface information since the operation intrinsically needs sequential measurements of topography and electrochemistry. Although, the second type of probes focus on locating the electroactive area recessed at a certain distance from the apex of the tip, which have several advantages as described previously, up to now these advantages were impaired with the disadvantage of larger integrated electrodes with micrometer and sub-micrometer dimensions.

4.2 Experimental

4.2.1 Electrochemical experiments

CVs, recorded current approach curves, and AFM-SECM imaging experiments were performed in aqueous solution containing 5 mM hexaammine-ruthenium(III) trichloride ($Ru(NH_3)_6^{3+}$, (Sigma-Aldrich, St. Louis, MO), and 0.5 M potassium chloride (KCl, Sigma-Aldrich, St. Louis, MO) as supporting electrolyte. A (bi)potentiostat (CHI842B, CH instruments, Austin, TX) was used to control all electrochemical experiments. A platinum wire served as a counter electrode and a freshly chloridized silver wire (Goodfellow, U.K.) served as reference electrode (AgQRE). The solutions were prepared using deionized water with a resistance of 18.2 MΩ cm at 25 °C obtained from a water purification system (Millipore, Billerica, MA).

4.2.2 AFM-SECM imaging

AFM-SECM imaging experiments were performed with the same set-up as described in section 3.2.3. Two samples were designed and fabricated as model samples for combined imaging experiments. The first sample was a single-sided polished (100) silicon substrate coated with 500 nm thick PECVD Si_xN_y with an approx. size of 2 x 2 cm^2. In a next step, a layer of 10 nm thick Ti was deposited as adhesion layer and consecutively a layer of 50 nm thick Au was deposited by e-beam evaporation (CHA E-beam) and patterned into a strip using the lift-off technique as shown in **Figure 4.1A**. For the second sample, a silicon substrate was used again and coated with 500 nm thick PECVD Si_xN_y. A layer of 10 nm thick Ti and consecutively a layer of 120 nm thick Au was deposited using an e-beam evaporator. After the deposition steps, a pattern of alternating conductive Au lines and insulating Si_xN_y lines were generated using bitmap-

assisted FIB milling (**Figure 4.1B**). For the alternating patterns, 300 – 400 nm width of the conductive lines and 300 nm or 600 nm of insulating features were milled, generating a pattern with a periodicity of conductive and insulating lines.

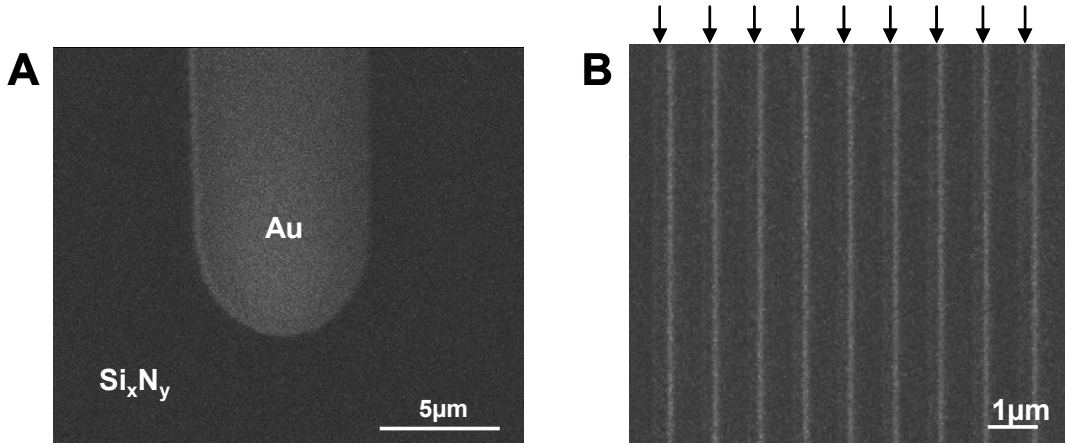

Figure 4.1 SEM images of the model samples prepared for AFM-SECM imaging experiments. (A) Au strip pattern (Au strip: width approx. 8 µm, thickness approx. 60 nm) (B) Sample consisting of alternating patterns of conductive and insulating lines. The conductive lines are indicated with arrows. (Conductive lines: width approx. 300 - 400 nm, thickness approx. 120 nm, distance between the lines approx. 600 nm).

4.2.3 Fabrication of AFM tip-integrated disk nanoelectrodes

4.2.3.1 Overview of the fabrication process

The overall schematic of fabrication process flow for the AFM tip-integrated disk nanoelectrodes is shown in **Figure 4.2.** The processes for the fabrication of cantilever probes are developed on a 500 - 550 µm thick, 4-inch diameter, single sided polished (100) silicon wafer. The first step of the process defines the pyramidal shape of the AFM

tip at the surface of the silicon substrate by using anisotropic silicon wet etching **(Figure 4.2A)**. As shown in **Figures 4.2B**, a low stress Si_xN_y layer is deposited as the bottom cantilever layer using low-pressure chemical vapor deposition (LPCVD), and in addition contact pads are patterned for electrical connecting the integrated electrode later to an external potentiostat for measurements. Cylindrical-shaped holes as a mold for disk nanoelectrodes are milled using focused ion beam technology (**Figure 4.2C),** and these holes are then consecutively back-filled with Au as electrode material using e-beam evaporation as shown in **Figure 4.2D**. An Au metal line is patterned connecting the electrode area with the contact pad (**Figure 4.2E**) and the metal patterns are then insulated with 800 nm - 1000 nm thick PECVD Si_xN_y as the top cantilever layer and patterned into cantilever array profiles **(Figure 4.2F)**. This patterned cantilever membrane is bonded to a Pyrex glass chip, which is partially diced to align and release cantilevers as shown in **Figure 4.2G**. Cantilevers are released by stripping the entire silicon sacrificial layer using a silicon wet etchant. As the last step, a disk-shaped electroactive area is exposed and a non-conductive AFM tip is shaped by FIB milling (**Figure 4.2H**). The detailed fabrication steps for the process will be discussed in following sections.

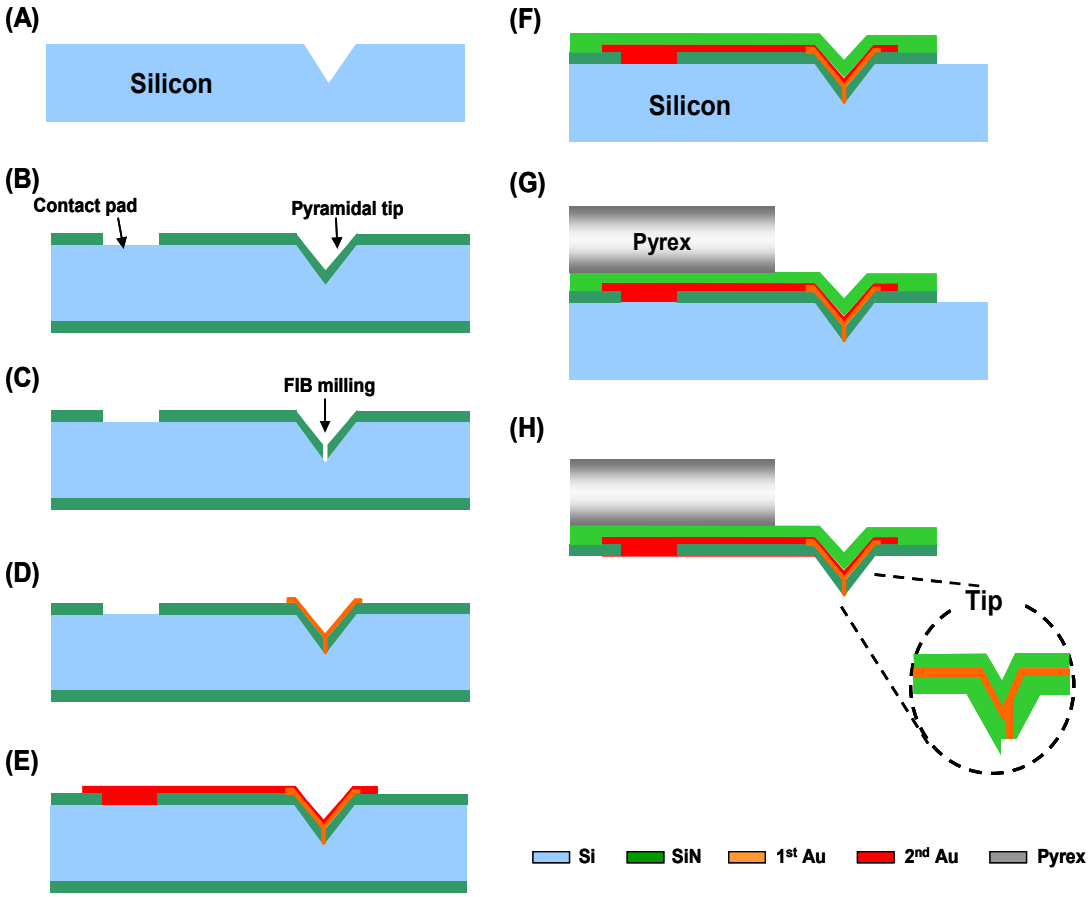

Figure 4.2 Schematic of the fabrication process flow. (A) Pyramidal tip formation, (B) bottom Si_xN_y of cantilever layer deposition and contact pad patterning, (C) FIB hole milling (D) Au back filling by evaporating, (E) metal line patterning, (F) top Si_xN_y deposition and cantilever patterning, (G) anodic bonding to Pyrex glass, (H) releasing cantilever and finally FIB milling to expose the electrode and shape the AFM tip.

4.2.3.2 Cantilever design

The cantilever itself is undoubtedly one of the most critical elements in the AFM probe design. Its dimensions need to be deliberately considered in the fabrication

processes since the dimensions of the cantilever directly affect the spring constant, which is one of the important physical parameter of AFM cantilevers. Besides a high resonance frequency for reduced noise levels, a low spring constant is desirable for low force impact on soft samples such as biological entities (e.g. cells). Long and narrow cantilevers have a relatively low spring constant in comparison to short and wider cantilever[17-18]. However, these cantilevers are more fragile and can be easily broken during operation or manufacturing. In addition, a compromise in dimensions has to be considered as a high resonance frequency demands opposite dimensions as a low force constant[17-18].

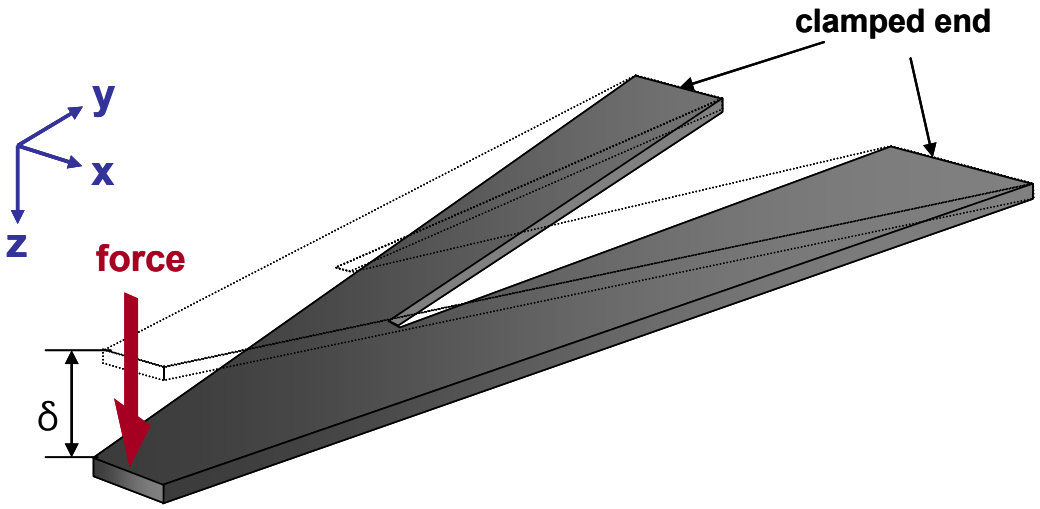

Figure 4.3 Triangular cantilever with two clamped legs (dashed line). When a force is applied to the end, the cantilever is displaced to the same direction (solid line). The spring constant can be obtained by the relationship between the applied force and the displacement.

Triangular cantilevers with several different types of dimensions have been designed in a batch and the related effective spring constants were estimated. For a triangular cantilever as illustrated in **Figure 4.3** the effective spring constant (k) can be expressed by Hook`s law (**Equation 4.1**), assuming each end of the two legs of the cantilever is clamped, which is the case as they are bonded to a holder made of Pyrex glass. Applying a force F to the z-axis of the end of the triangular cantilever, the static deflection δ is defined by.

$$k = \frac{F}{\delta} \qquad \text{Equation 4.1}$$

For a force applied in z-axis, the equilibrium equation can be expressed as

$$F_z = -\frac{\partial \tau_{xz}}{\partial x} - \frac{\partial \tau_{yz}}{\partial y} - \frac{\partial \sigma_z}{\partial z} \qquad \text{Equation 4.2}$$

where σ_z is the normal stress tensor and $\tau_{xz,}\ \tau_{yz}$ are shear stress tensors. The stress (σ) can be related to strain (ε) by the elasticity matrix (D),

$$\sigma = D\varepsilon \qquad \text{Equation 4.3}$$

$$\sigma_x = \frac{E}{(1+\nu)(1-2\nu)}\left[(1-\nu)\varepsilon_x + \nu\varepsilon_y + \nu\varepsilon_z\right] \qquad \tau_{xy} = \frac{E}{2(1+\nu)}\gamma_{xy}$$

$$\sigma_y = \frac{E}{(1+\nu)(1-2\nu)}\left[\nu\varepsilon_x + (1-\nu)\varepsilon_y + \nu\varepsilon_z\right] \qquad \tau_{yz} = \frac{E}{2(1+\nu)}\gamma_{yz}$$

$$\sigma_z = \frac{E}{(1+\nu)(1-2\nu)}\left[\nu\varepsilon_x + \nu\varepsilon_y + (1-\nu)\varepsilon_z\right] \qquad \tau_{xz} = \frac{E}{2(1+\nu)}\gamma_{xz}$$

Equation 4.4

where E is the Young's modulus, ν is the Poisson ratio, γ is the shear strain. The strains can be 3-dimensionally described by deformation components (u, v, w) as

$$\varepsilon_x = \frac{\partial u}{\partial x} \qquad \gamma_{xy} = \left(\frac{\partial u}{\partial y} + \frac{\partial v}{\partial x}\right)$$

$$\varepsilon_y = \frac{\partial v}{\partial y} \qquad \gamma_{yz} = \left(\frac{\partial v}{\partial z} + \frac{\partial w}{\partial y}\right)$$

$$\varepsilon_z = \frac{\partial w}{\partial z} \qquad \gamma_{xz} = \left(\frac{\partial u}{\partial z} + \frac{\partial w}{\partial x}\right)$$

Equation 4.5

For different dimensions of cantilevers, the displacement of the z-axis induced by an applied force (F_z) in the same direction can be obtained by calculation using **Equation 4.2** through **4.5**. This was obtained using a software package from COMSOL multiphysics 3.4 by defining the boundary conditions of clamping the two cantilever legs and applying a force of 0.1 N in z-axis at the end of the cantilever. The displacement obtained by this calculation for the applied force was used in **Equation 4.1** to determine

the spring constants for different dimensions. The AFM-SECM cantilevers consist of two Si_xN_y layers, where one is LPCVD Si_xN_y and the other is PECVD Si_xN_y. The metal layer for electrical connection was not considered in this calculation since it was designed to be much smaller in dimensions compared to the cantilever width and thinner (0.05 μm) compared to the total thickness of the cantilever (approx. 1.5 μm). In **Table 4.1,** dimensions for different types of AFM-SECM cantilevers are summarized. For total thickness of the cantilever, only the thickness of the top Si_xN_y layer deposited by PECVD was varied in the calculations, whereas a fixed thickness of 0.6 μm of the bottom Si_xN_y layer deposited by LPCVD was used. As LPCVD Si_xN_y is chemically more stable and has less pinholes in comparison to PECVD Si_xN_y[19], the PECVD Si_xN_y layer needs to be thicker than the LPCVD Si_xN_y layer.

Table 4.1 Different dimensions of AFM-SECM cantilevers.

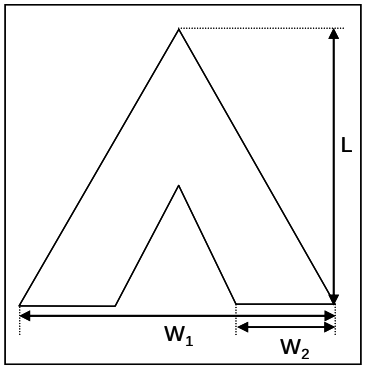

Type	Length(L) [µm]	Width1(W1) [µm]	Width2(W2) [µm]
A	250	225	46
B	200	195	35
C	165	150	26
D	135	134	22
E	100	104	22

For the different dimensions of cantilevers (**Table 4.1**), spring constants were calculated in respect to the variation of thickness in **Figure 4.4**. A reduced thickness of Si_xN_y layer is apparently advantageous for obtaining reduced spring constants, however a critical point for the AFM-SECM design is a sufficient insulation for the conductive layer. Hence, the final thickness of the Si_xN_y layer needs to be adjusted after electrochemical characterization of the probes, in order to determine the thickness of Si_xN_y, which is needed for perfect insulation. However it is expected that the total thickness of the cantilever will be in range of 1 - 1.6 µm based on previous results, which were obtained fabricating AFM-SECM probes using commercial AFM cantilevers, in which approx. less than 1.0 µm PECVD Si_xN_y was deposited for insulation.

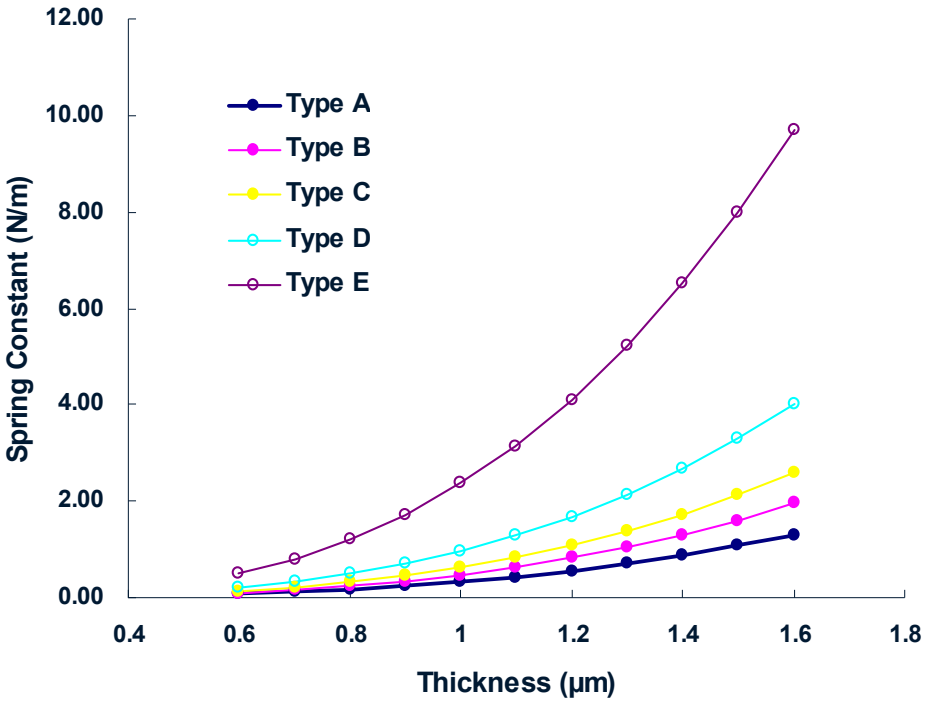

Figure 4.4 Spring constant (N/m) vs. thickness for different dimensions of cantilevers, which are listed in table 4.1.

4.2.3.3 Pyramidal tip formation

In a first step of the fabrication process, AFM-SECM probes were designed with a pyramidal shape of the tip. Arrays of these pyramidal grooves were defined at the surface of a 500 - 550 µm thick, 4-inch diameter, single sided polished (100) silicon wafer. As a masking layer for the silicon wet etching, a layer of 300 - 400 nm Si_xN_y was deposited by PECVD and inductively coupled plasma (ICP) etching was used to pattern 4 x 4 µm squares of wet etch windows. Through the etch windows, the pyramidal shape of grooves were formed by anisotropic wet etching in 30 wt% potassium hydroxide (KOH) at 80 °C. Due to the crystal structure of the (100)-oriented silicon and high etching ratio (111) to

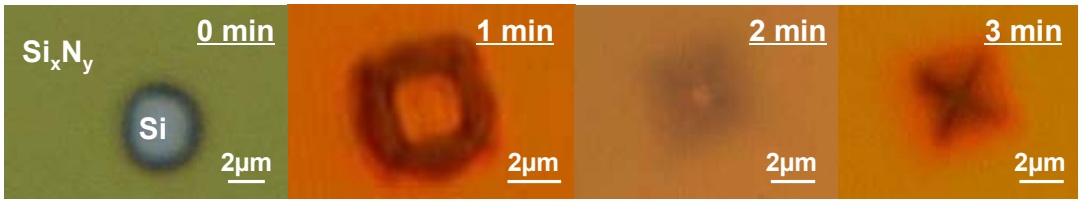

Figure 4.5 Optical micrographs showing the pyramidal grooves for AFM-SECM probes at different etching times.

(100) directions, known as 400:1[19], the sidewalls of pyramidal grooves were defined with a angle of 54.74º to the plane surface of the silicon substrate. Given the geometrical consideration, the depth of the groove, which corresponds to the height of the formed tip was estimated to be approx. 2.8 µm. The measured silicon-etching rate was approx. 1.1 µm/min and 4 min of etching time was enough to obtain a pyramidal groove with a sharp apex. The quality of the pyramidal grooves was investigated by optical microscopy ensuring a proper etching process (**Figure 4.5**).

4.2.3.4 Bottom silicon nitride layer deposition and contact pad patterning

A masking layer for wet-etch deposited in the previous step was stripped using HF solution, prior to the deposition of a layer of approx. 600 - 800 nm thick low stress Si_xN_y, which defines the bottom cantilever layer. The low stress Si_xN_y was deposited by LPCVD (Tystar nitride furnace; temperature = 850 °C, gases were SiH_2Cl_2 and NH_2). In a next step, 600 x 600 µm square-shaped contact pads for electrical connecting the integrated electroactive area later to a potentiostat were patterned at a distance of approx. 2.4 mm from the pyramidal grooves as illustrated in **Figure 4.6**. **Figure 4.7** shows a SEM image of an array at the described fabrication step. As marked in the SEM image, each

rectangular island is one probe sample with dimensions comparable to commercial cantilevers in order to fit in the cantilever mount of any AFM system.

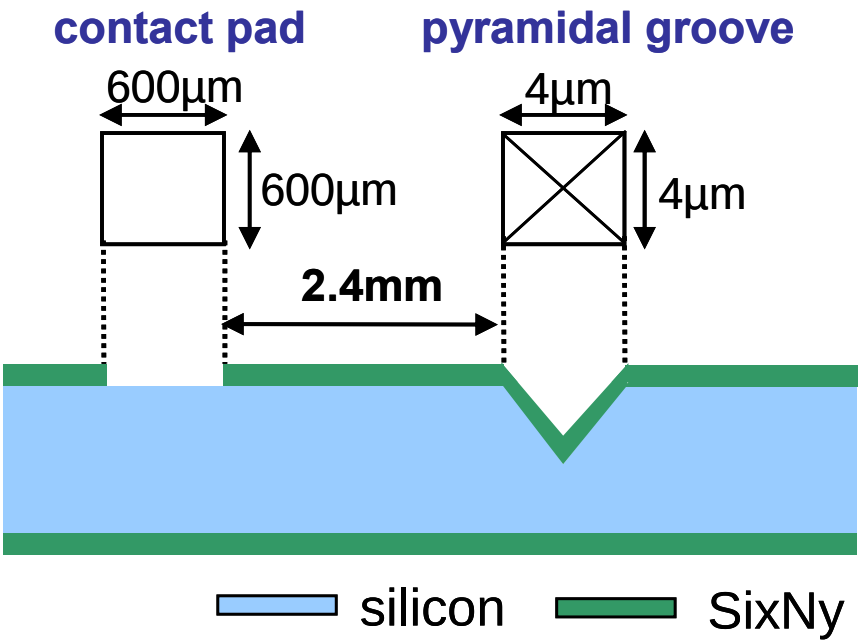

Figure 4.6 Schematic of contact pad patterning with deposited bottom layer of Si_xN_y of the cantilever.

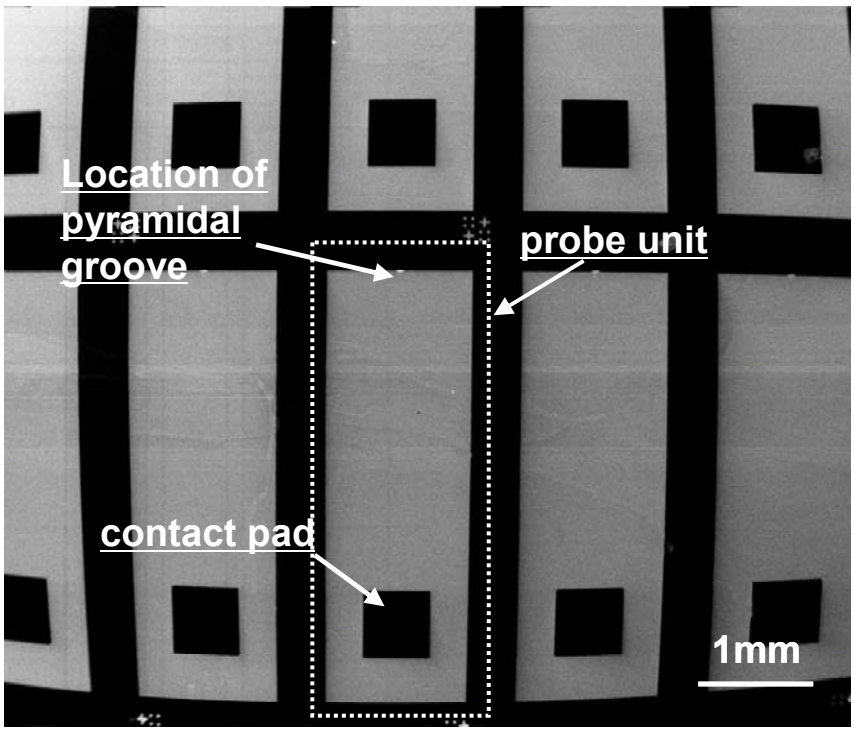

Figure 4.7 SEM image showing several units of the probe design. Each unit has dimensions that will later allow mounting the probe in any AFM systems.

4.2.3.5 Fabrication of disk nanoelectrodes

Cylindrical-shaped holes were milled inside each of the pyramidal grooves using FIB technology (**Figure 4.2C**). These holes then served as a mold for disk nanoelectrodes. **Figure 4.8** shows the scheme and in addition a SEM image for a hole milled into the pyramidal groove. Hole milling was performed in two sequential steps. First a hole with 200 nm depth and 800 nm diameter was milled prior to a cylindrical hole with a smaller diameter of 100 - 300 nm. This larger ratio of diameter to depth of the hole was used to improve back filling the hole with Au by evaporation in the next step.

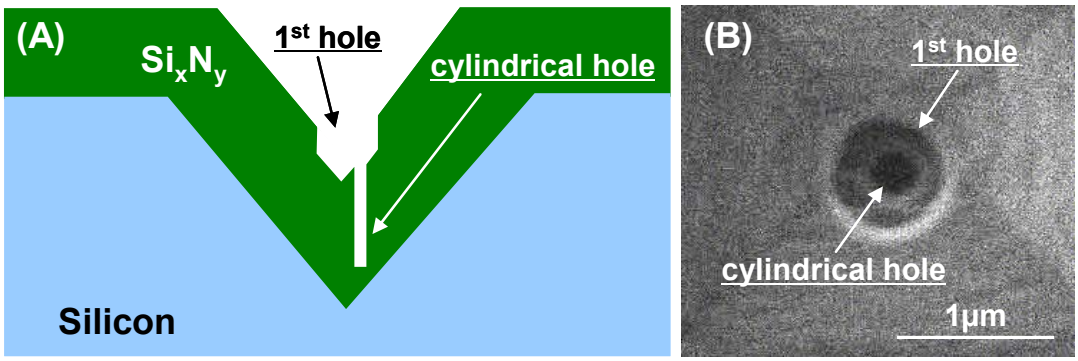

Figure 4.8 (A) Schematic of the cross-sectional view showing the hole milled into the pyramidal groove. (B) SEM image of the milled holes. 1st hole was milled prior to cylindrical hole to enlarge the ratio of diameter to depth, which improves the Au back filling by evaporation.

The hole was not milled completely through to the Si_xN_y layer. The FIB milling was stopped so that a layer of 50 nm - 100 nm Si_xN_y remained in order to avoid milling through the layer to the surface of the silicon substrate as illustrated in **Figure 4.8A**. The diameter of the second cylindrical hole determined the size of electroactive area at the final step of fabrication.

The second step in fabricating disk nanoelectrodes was filling the cylindrical hole with Au as electrode material (**Figure 4.2D**). A layer of 10 nm Ti for adhesion and a layer of approx. 200 nm Au was deposited with a deposition rate of 1 Å/s using e-beam evaporator (CHA E-beam; base pressure = 8.8 x 10^{-8} Torr) to fill the cylindrical hole. As shown in **Figure 4.9A**, the Au layer was only deposited at the area of the pyramidal groove using a negative photoresist mold for the lift-off process. This process was tested with conventional AFM cantilever. Inside of the pyramidal tip of the cantilever, a

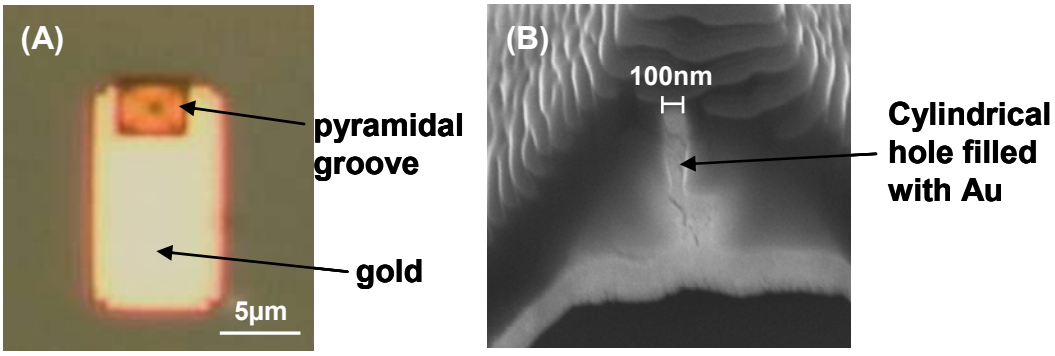

Figure 4.9 (A) Optical image of pyramidal groove after Au deposition. Au layer was deposited only at the area of the pyramidal groove using negative photoresist mold for the lift-off process. (B) Cross-sectional SEM image of a AFM tip having a disk nanoelectrode.

cylindrical hole was milled and Au was back-filled. **Figure 4.9B** shows the SEM image of a cross-sectional view of a cylindrical hole filled with Au.

For electrical connecting the integrated disk nanoelectrode to an external potentiostat, an Au metal line was patterned from the electrode area across the cantilever arm to the contact pad using again lift-off technique as shown in **Figure 4.10**. This sequential Au patterning as shown in **Figure 4.9** and **Figure 4.10** was applied to prevent

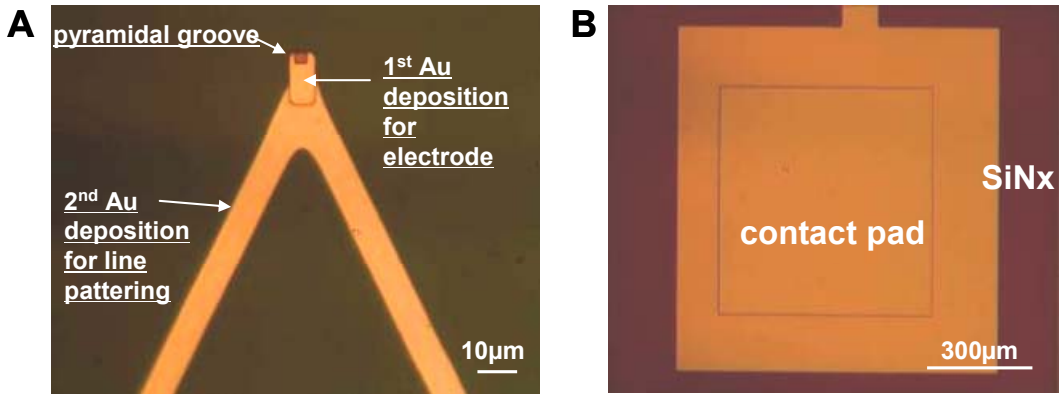

Figure 4.10 Optical images of the patterned metal line, which allow electrical contact of the integrated electrode; (A) metal line and (B) contact pad.

bending of the cantilever caused by intrinsic stress due to the thick metal deposition (during the filling of the whole). For this reason, the thickness of the deposited metal line (contact line) was only 50 nm thick with an adhesion layer of 8 nm Ti both deposited by e-beam evaporation (CHA E-beam; base pressure = 8.8 x 10^{-8} Torr).

4.2.3.6 Cantilever patterning

PECVD Si_xN_y was deposited and patterned into cantilever shape (**Figure 4.2F)**. For the top cantilever layer following points are crucial. First, a pinhole-free insulation of the previously deposited metal layer has to be obtained, secondly low-stress deposition is important to prevent bending of the cantilever, and thirdly the layer has to be suitable for anodic bonding since this layer is supposed to directly bond to a Pyrex glass chip.

For good insulation of the metal line, based on previous AFM-SECM fabrication results and experimental tests, the thickness needs to be at least approx. 0.8 - 1.0 µm obtained with multiple deposition steps for sufficient electrical insulation of the AFM-

SECM probes. With a fixed thickness of 0.8 μm, the stress of PECVD Si_xN_y was adjusted to achieve straight cantilever. The stress of the PECVD Si_xN_y layer can be controlled by varying the flow rate of nitrogen[20]. Prior to the deposition on the probe samples, the stress of PECVD Si_xN_y layer was measured by profilometer (Tencor KLA profilometer), which measures and analyzes the curvature change of a silicon substrate before and after thin film deposition of Si_xN_y layer. The change of measured stress as the nitrogen gas flow varies at deposition conditions with 1100 mTorr and 700 mTorr is shown in **Figure 4.11**. The pressure was changed to find out parameters for improved conditions of the anodic bonding, which will be discussed later. Since the metal line is narrow and thin compared to the whole cantilever structure, only two layers of LPCVD Si_xN_y and PECVD Si_xN_y need to be considered for stress evaluation of the cantilever. Since the LPCVD Si_xN_y layer, as the bottom cantilever layer, has only few tenths (approx. < 30 MPa) of tensile stress, the stress of the PECVD Si_xN_y layer was targeted to be zero.

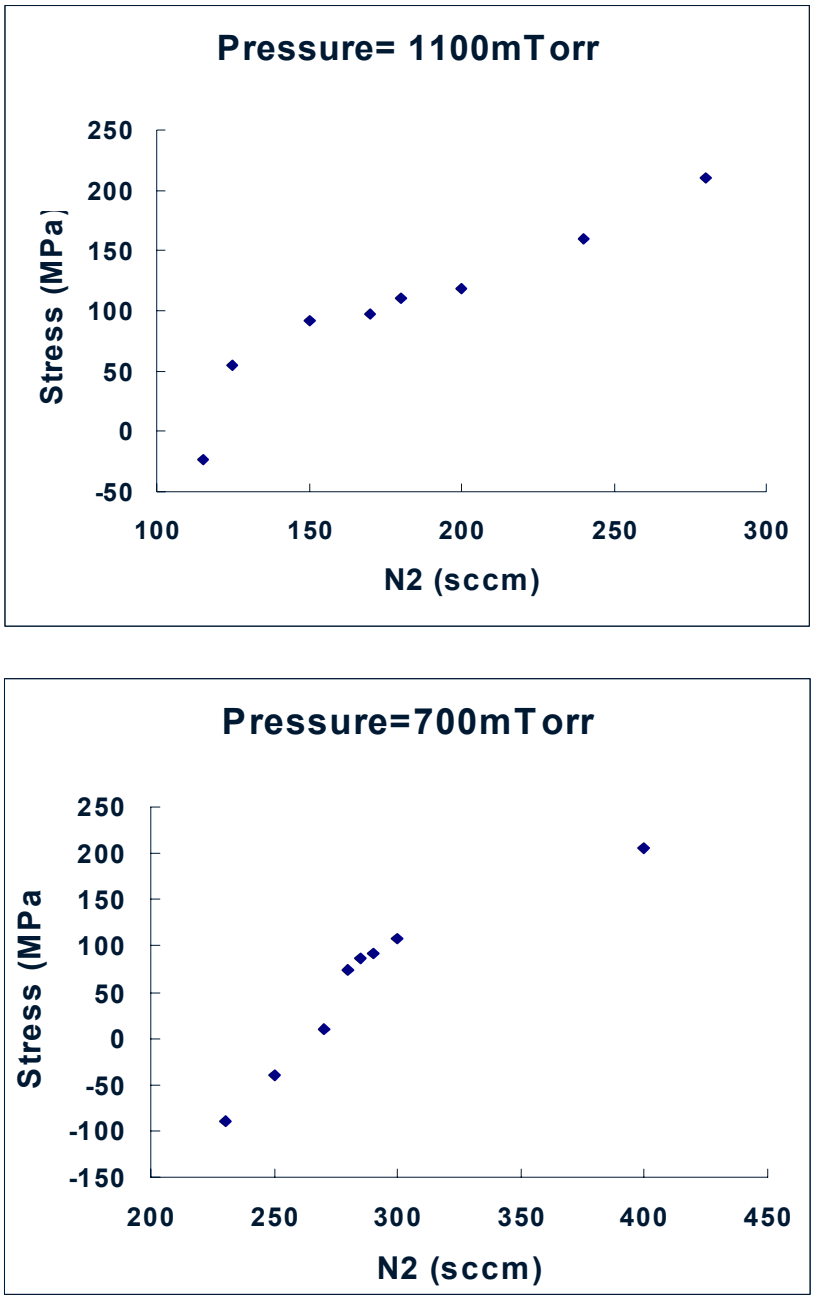

Figure 4.11 Stress change in silicon nitride layer with variation of the nitrogen gas flow at a deposition pressure = 1100 mTorr (top) and pressure = 700 mTorr (bottom).

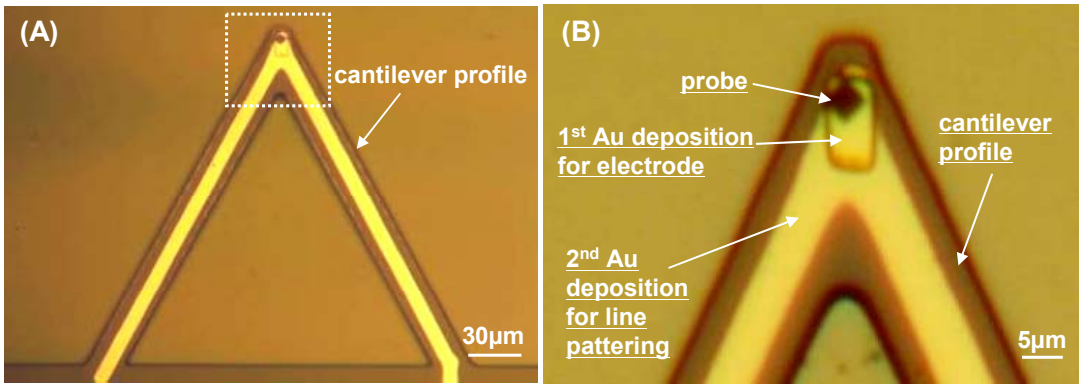

Figure 4.12 Optical image: (A) for patterned cantilever profile and (B) zoom of the marked area (box) in (A).

For the best result, a 900 nm thick layer of PECVD Si_xN_y (Unaxis PECVD system; temperature = 300 °C, pressure = 1100 mTorr, power = 50 W, gases were SiH_4, He and NH_3) as the top cantilever layer was deposited and patterned into a triangular cantilever shape. Cantilever profiles were patterned at 5 different dimensions as discussed in section 4.2.3.2. Mask material of Futurrex NR5-8000 negative photoresist was spin-coated at the samples with 4000 rpm and ICP etching was used for the Si_xN_y layers to be patterned into cantilevers (**Figure 4.12**). After the cantilever patterning, the backside silicon nitride was etched away for the next step of bulk silicon wet etching.

Reactive ion etching (RIE; Advanced vacuum vision RIE system; pressure = 12 mTorr, power = 350 W; reaction gases were CHF_3 (40 sccm), O_2 (6 sccm), Ar (10 sccm)) was used for backside etching, while the front side was protected by Futurrex NR5-8000 negative photoresist, which was spin-coated with 4000 rpm.

4.2.3.7 Anodic bonding and cantilever release

Anodic bonding technique was utilized to transfer the patterned cantilever from the silicon substrate to a chip made of glass (Pyrex 7740) as a support for the fabricated cantilever (**Figure 4.2G**). The glass was diced three times. The first dicing was performed to dice partially the glass forming a cavity so that the cavity is aligned just right above the cantilevers for the anodic bonding process (**Figure 4.13A**). After the anodic bonding, the glass was diced (400 μm in depth) again between probe units so that they can be easily separated after the fabrication process is complete. Also, the remainder glass above cantilever is diced to be then removed as shown in **Figure 4.13B**.[21]

Although the anodic bonding process of silicon to glass is extensively studied and is a well established process, the bonding of dielectric layers such as silicon nitride to

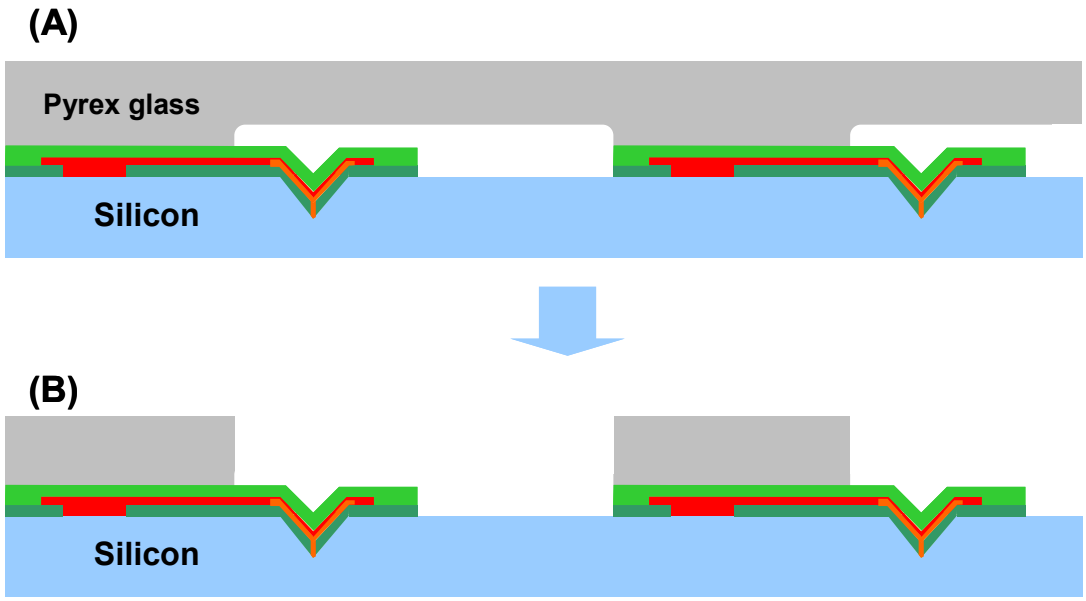

Figure 4.13 Schematic: (A) anodic bonding of the probes and the partially diced Pyrex glass. (B) Partial dicing to remove the glass above of cantilevers.

glass requires more deliberate choice of bonding parameters and stringent surface quality since the dielectric layer prevents the electrostatic field as a source for anodic bonding. All anodic bonding tests and processes, described in this thesis were obtained with a Karl Suss SB6 bonder. A schematic of its operation is shown in **Figure 4.14**. Since this method uses a pinpoint type cathode, it requires a very high applied voltage and longer bonding times compared to a cathode allowing whole contact. However, the pinpoint contact is advantageous in eliminating voids between the substrates as air can escape during the process by beginning bonding from the area near the cathode point progressively to the area far from the point instead of bonding all the area at a same time. In order to test the bonding, layers of 600 nm thick PECVD Si_xN_y were deposited on silicon substrates and bonded to glass substrates with parameters of temperature = 350 ºC, voltage = 1000V, pressure = 2000 mbar and bonding time = 1hr followed by sacrificial silicon substrate wet etching.

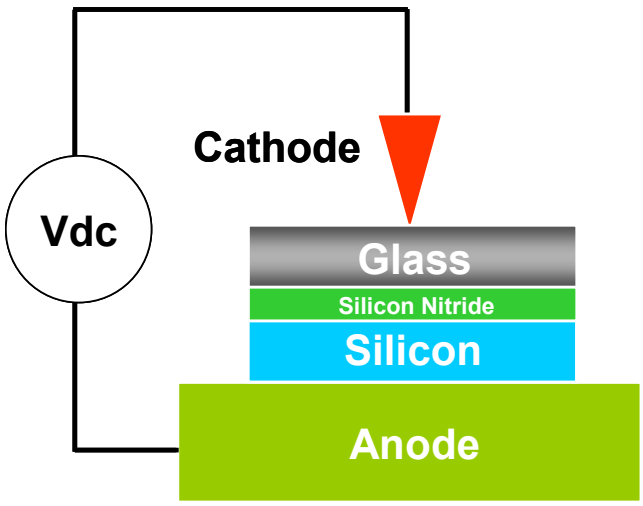

Figure 4.14 Schematic of anodic bonding using a Karl Suss SB6 bonder.

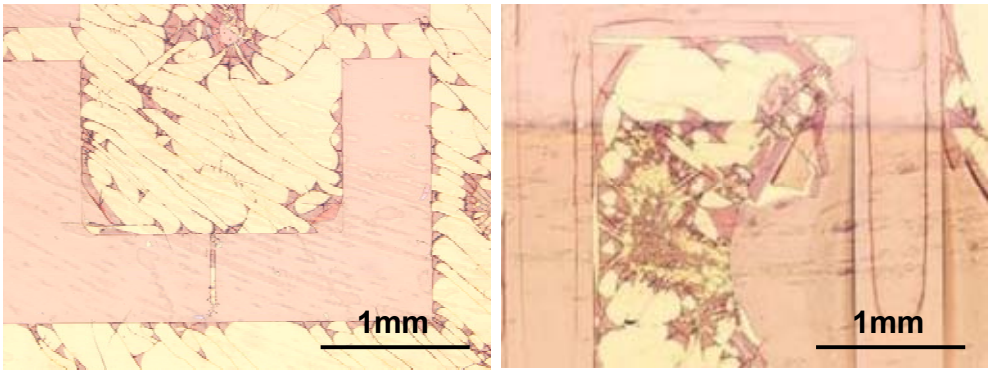

Figure 4.15 Optical micrographs of cracked silicon nitride layers after anodic bonding to Pyrex glass without appropriate parameters and optimization of the surface treatment.

Figure 4.15 shows optical micrographs of the substrate surface after the test. Unless the parameters and surface pretreatments are not appropriately optimized, it results in a cracked nitride layer as the layer is not strongly bonded to the glass substrate. The challenge of the bonding process is avoiding any voids or hairline cracks so that there is no leakage current between the external electric connection and the probes. Applied voltage, bonding time and temperature are considered as the critical parameters for the optimization of the anodic bonding process, which have been investigated for successful transfer of the cantilever probes to the Pyrex glass chip. In addition, the influence of surface treatment on the bonding process has been studied. For each test, the quality of the anodic bonding was estimated by the percentage of bonded area, which was determined by optical microscopy. The 4-inch silicon and glass substrates were diced into pieces with a size of 38.28 x 27 mm^2, which equals 132 units of cantilever probes. The percentage of bonded area was calculated as below.

$$\text{Percentage of bonded area} = \frac{\#\text{ of bonded unit of cantilever probes}}{\text{Total 132 units of cantilever probes}} \quad \text{Equation 4.6}$$

In this calculation, only the units of cantilever probes free of voids and any hairline cracks were considered as bonded units since the voids and cracks caused by weak bonding can be a reason for leakage current when obtaining combined AFM-SECM measurements. **Figure 4.16** shows optical micrographs of bonded and not bonded units. Voltage parameter was tested in a range of 1000 – 1200 V based on previously reported anodic bonding of LPCVD Si_xN_y to glass substrate[22], however there was no noticeable difference in percentage of bonded area. Bonding time was varied based on monitoring current-time characteristics, which indicate the progress of anodic bonding generated by the bonder during the process; times were chosen to be in range of 1 hr 30 min to 2 hrs allowing the current to get stable and as close as possible to zero. Temperature settings

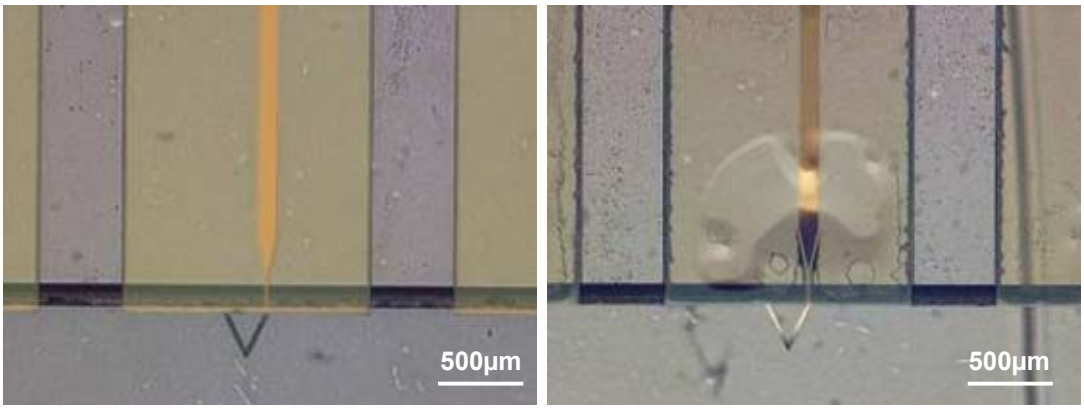

Figure 4.16 Optical micrographs of a bonded unit (left) and not-bonded unit (right).

were varied in a range of 300 - 400 °C. 400 °C was the upper limit to avoid changing the properties of PECVD Si_xN_y. **Table 4.2** shows the percentage of bonded area with changing the bonding temperature while the other parameters were fixed (voltage = 1200 V, pressure = 2000 mbar, time = 1 hr 30 min). Both substrates were pre-cleaned with piranha solution (H_2SO_4 from Fisher Scientific, Pittsburgh, PA; 30 % H_2O_2 from JT Baker, Phillipsburg, NJ; ratio 4:1) at 120 °C for 10 min. The percentage of bonded area was increased when increasing the temperature from 300 to 350 °C. However, no difference was found in the range of 350 - 400 °C.

Table 4.2 Percentage of bonded area with changing the bonding temperature.

Temperature (°C)	Bonded area (%)
300	10-20
350	50-60
370	50-60
400	50-60

* The other bonding parameters were fixed at voltage = 1200 V, pressure = 2000 mbar, time = 1 hr 30 min
* Both substrates were pre-treated with piranha cleaning (4:1 H_2SO_4-H_2O_2 at 120 ºC for 10 min.)

The influence of pre-treatments on both substrates was also investigated. **Table 4.3** shows the pre-treatments used at each substrate and the percentage of bonded area that was obtained. For this experiments, 800 - 900 nm of PECVD Si_xN_y was deposited as top cantilever layer and bonded to glass substrate using Karl Suss SB6 bonder with fixed bonding parameters (temperature = 370 °C, voltage = 1200 V, pressure = 2000 mbar, time = 2 hrs). Inspection of bonded area using optical microscope was performed after removal of the sacrificial silicon substrate using tetramethylammonium hydroxide

Table 4.3 Percentage of bonded area influenced by surface pre-treatments.

Pre-treatment	Bonded area	Pre-treatment	Bonded area
Acetone, Methanol, IPA Acetone, Methanol, IPA	35%	Piranha, UA Piranha, HF (50:1)	70%
Piranha Piranha	< 60%	Piranha, UA, RCA Piranha, RCA, HF (50:1)	70%
Piranha, UA Piranha	< 60%	Piranha, UA, Anneal @350℃ 5min Piranha, HF (50:1)	90%
Piranha, UA, RCA Piranha, RCA	< 60%	Piranha, UA, Anneal @350℃10min Piranha, HF (50:1)	90%

* For each cells, the first row (black) is the pre-treatment of the Si_xN_y surface and the second row (green) is the pre-treatment of the glass substrate.
* UA = Ultrasonicating in acetone for 10 min,
* RCA = RCA cleaning
* The bonding parameter is fixed at applied voltage: 1200 V, temperature: 370 ºC, pressure = 2000 mbar, time = 1 hr 30 min.

(TMAH; 10 % at 70 °C, 20 hrs) wet etching for cantilever release (**Table 4.3**). For every sample, the area close to pinpoint was well bonded, however it was crucial to enhance the bonding quality of the area far from the pinpoint. As show in **Table 4.3**, the pre-treatment cleaning steps of the substrates have an important role in successful anodic bonding. Interestingly, treating the membrane of cantilever probes at bonding temperature for a few minutes prior to the anodic bonding process dramatically increased the percentage of bonded area to 90 %.

In addition, unlike the PECVD Si_xN_y layer prepared at 1100 mTorr, the percentage of bonded area for PECVD Si_xN_y deposited at 700 mTorr pressure could not be increased over 30 % regardless of the applied pre-treatments. **Figure 4.17** shows the topographical images, obtained by AFM (Agilent Technologies, Chandler, AZ) of PECVD Si_xN_y layers deposited at 1100 mTorr (temperature = 300 °C, power = 50 W,

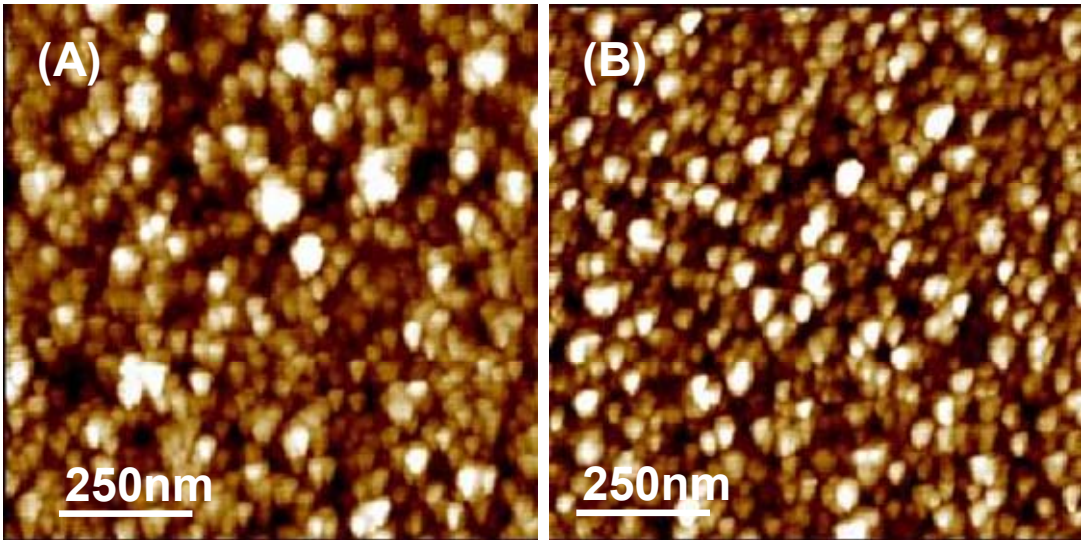

Figure 4.17 AFM topographical images for PECVD Si_xN_y deposited at (A) 700 mTorr, and (B) 1100 mTorr.

gases were SiH_4, He and NH_3) and at 700 mTorr of pressure (temperature = 300 °C, power = 50 W, gases were SiH_4, He and NH_3). Larger grain sizes are visible at the layer deposited at 700 mTorr. The increased roughness of the surface hinders strong bonding.

After releasing the cantilevers by silicon wet etching, electrochemical measurements were performed in addition to optical inspection to detect any pinholes or damages caused by the bonding process. Tests were performed by cyclic voltammetry (CV) using a three electrode arrangement (a silver/silver chloride as reference electrode and a platinum wire as a counter electrode). CVs were recorded in a solution containing 5 mM hexaammineruthenium(III) trichloride $Ru(NH_3)_6Cl_3$ Sigma-Aldrich, St. Louis, MO) and 0.5 M potassium chloride (KCl, Sigma-Aldrich, St. Louis, MO) as a supporting electrolyte. **Figure 4.18** shows an example of an obtained CV. The pico-ampere scale of

small charging current demonstrates the successful transfer of AFM-SECM cantilever probes to Pyrex glass by the bonding process.

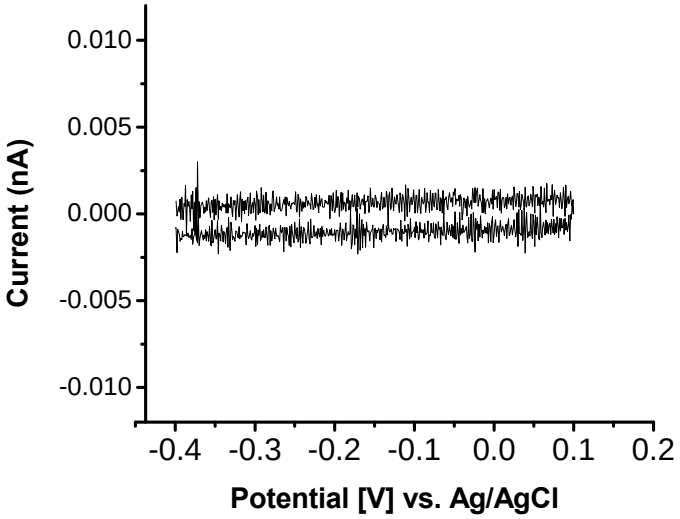

Figure 4.18 CVs obtained after bonding at AFM-SECM cantilevers in 5 mM $Ru(NH_3)_6^{3+}$ solution containing 0.5 M KCl (scan rate 0.1 V s^{-1}).

4.2.3.8 FIB milling and electrochemical characterization of the combined tips

FIB milling is the final step of the fabrication process. This step is crucial for exposing the electroactive area and re-shaping the AFM tip (**Figure 4.2H**). As the electrochemical characteristics of the integrated electrodes depend on geometrical aspects (spacing between electrode and tip), this step is critical and details will be discussed in the next section. **Figure 4.19** shows a schematic of the milling process. Several milling strategies were tested to improve the process of implementing disk nanoelectrodes. However, the first two milling steps are almost identical to the FIB milling for integrating

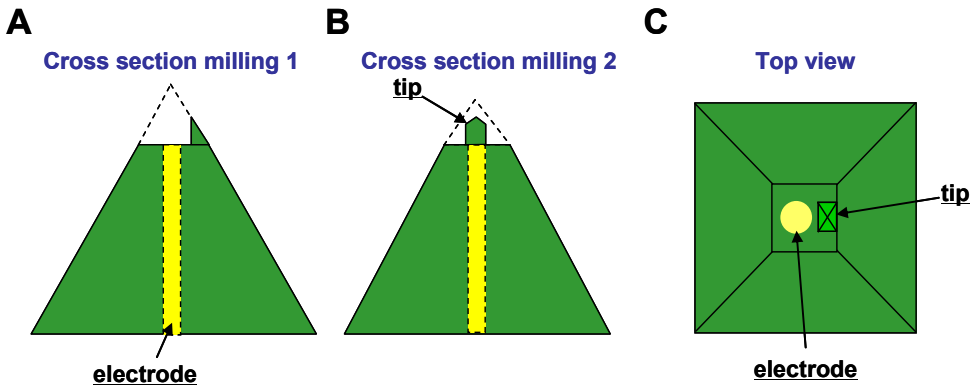

Figure 4.19 Schematic of the milling process. The cylindrical electrode is not visible in 2D view and drawn with dashed line. Similar to the integration of frame-electrodes, two steps of milling were executed. (A) Front view of the first FIB milling. (B) Side view (rotation by 90º) used for the second FIB milling. (C) Top view after milling process.

frame-shaped electrodes, besides that milling times were significantly reduced (approx. 10 times shorter).

Figure 4.20 shows SEM images of batch-fabricated AFM-SECM probes before FIB milling. Straight cantilevers could be obtained even for cantilever with a length 250 µm as shown in **Figure 4.20A**. Again, the lengths of the cantilevers were varied from 100 – 250 µm in respect to the desired force constant (section 4.2.3.2). **Figure 4.20B** shows the side view of a cantilever. Pyramidal-shaped tips with small tip radii similar to commercial probes can be obtained as exemplarily shown in **Figure 4.20B**. **Figure 4.20C** and **Figure 4.20D** show the topside and backside of a cantilever, respectively. In the SEM image of the backside of a cantilever, the patterned metal line, which is insulated with Si_xN_y is visible.

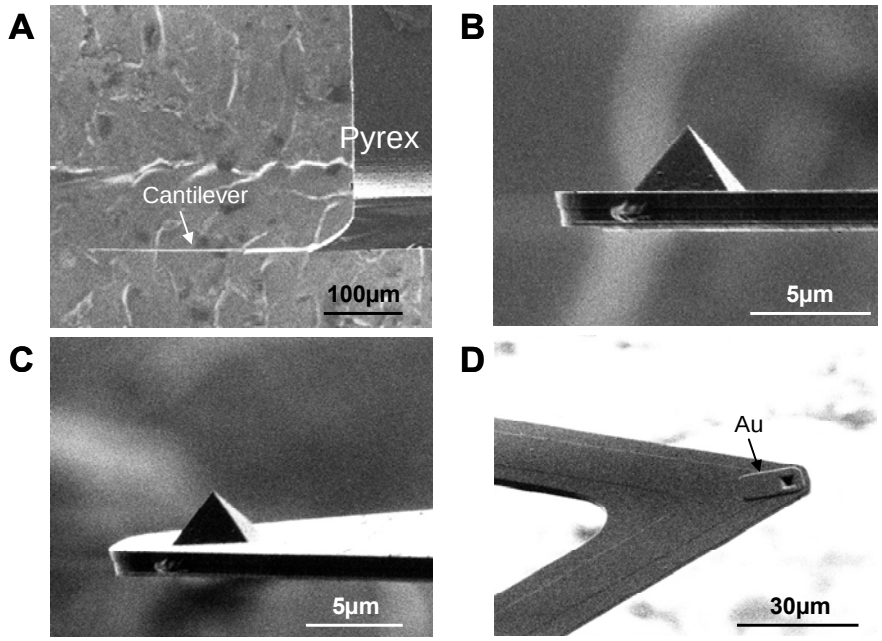

Figure 4.20 SEM images: (A) and (B) side view of a batch-fabricated probe. (C) Topside of a cantilever. (D) Backside of a cantilever.

Figure 4.21 shows SEM images of two AFM-SECM probes and the corresponding cyclic voltammograms recorded after exposing the disk nanoelectrodes by FIB milling. Disk-shaped electrodes are clearly visible and obtained radii derived from SEM imaging were 90 nm and 180 nm for A and B, respectively. The steady-state currents (included as value in the displayed CVs, **Figure 4.21**) obtained for each disk nanoelectrode were in good agreement with theoretically obtained values of 132 pA for probe A and 271 pA for probe B derived from **Equation 2.13** for steady-state current of disk-shaped electrodes. The discrepancy observed may be attributed to re-deposited material on the disk nanoelectrode during the FIB milling or may be attributed to geometrical deviations.

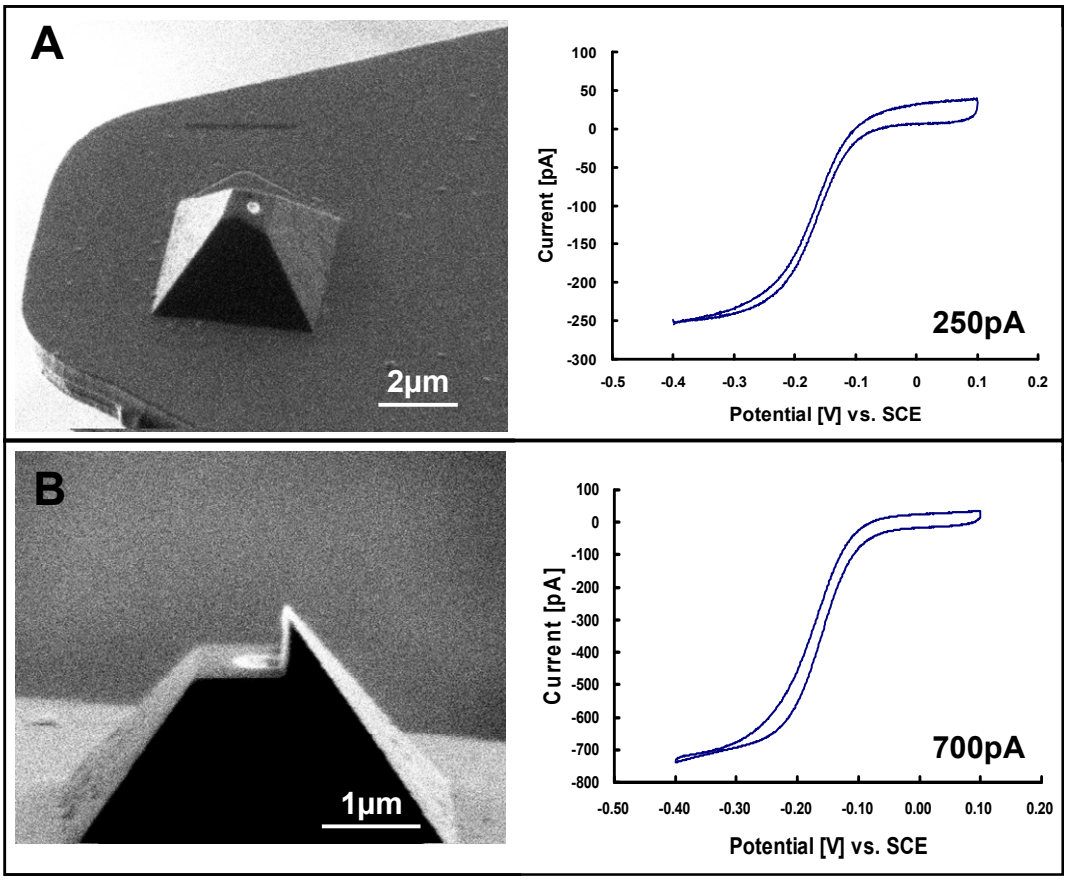

Figure 4.21 SEM images (left) and corresponding cyclic voltammograms (right) of tip-integrated disk nanoelectrodes. The diameters derived from SEM images of the electrodes were 180 nm for (A) and 370 nm for (B). CVs were obtained in 5 mM $(Ru(NH_3)_6)^{3+}$/0.5 M KCl solution (scan rate 100 mV s^{-1}). The currents noted in the images (right) are the steady-state currents.

Essentially, the equation describes the steady-state current of perfect disk-shaped electrodes with a symmetric insulation around the electrode. Neither the thickness of insulation nor a geometric obstacle, such as the AFM tip is considered. Hence an analytical model based on a numerical method has to be implemented for improved electrochemical characterization.

4.3 Results and discussion

4.3.1 Simulation

In this section, the simulation results of the electrochemical characteristics of AFM tip-integrated disk nanoelectrodes will be discussed. The influence of geometry on the electrochemical response will be considered in respect to concentration profiles. These simulations will not only give a better understanding of the electrochemical properties of nanometer-sized AFM-SECM tips, but also provide insight in experimental aspects for improving tip milling procedures.

For the simulation, $Ru(NH_3)_6^{3+/2+}$ was used as redox couple and concentration of the oxidized species is denoted as c(x,y,z) in cartesian coordinates. The hemispherical diffusion equation can be described with the following equation.

$$\frac{\partial c}{\partial t} = D\left(\frac{\partial^2 c}{\partial x^2} + \frac{\partial^2 c}{\partial y^2} + \frac{\partial^2 c}{\partial z^2}\right) \qquad \text{Equation 4.7}$$

Where D is the diffusion coefficient, c = the concentration, and t is the time. It is assumed that the oxidized form ($Ru(NH_3)_6^{3+}$) and reduced form ($Ru(NH_3)_6^{2+}$) of the redox couple have the same diffusion coefficient of 7.5 x 10^{-6} cm^2 s^{-1} [23]. The diffusion equation can be expressed as shown below considering a steady-state current, since the diffusion current at a microelectrode rapidly reaches the steady-state value as described in section 2.1.1.

$$\frac{\partial c}{\partial t} = D\left(\frac{\partial^2 c}{\partial x^2} + \frac{\partial^2 c}{\partial y^2} + \frac{\partial^2 c}{\partial z^2}\right) = 0 \qquad \text{Equation 4.8}$$

For solving this equation, the following boundary conditions were taken into account. The concentration of the bulk solution is the same as the initial concentration of oxidized species; the concentration of the reduced species is set to zero at a time t = 0. In addition, the concentration gradient at the insulation surface is zero since there is no flux through the surface of the insulator. The concentration of the oxidized species is zero at the surface of electrode at $t \neq 0$, as species arriving at the surface of the electrode are immediately reduced.

Simulations for approach curves and also for line scans were obtained taking into account the influences of a substrate in close proximity to the AFM-SECM probe. Following boundary conditions were established for the substrate. The concentration of oxidized species at the conductive substrate is the same as the concentration in bulk solution as the reduced species generated at the electrode surface is immediately oxidized. Again, the concentration gradient is set to zero for any insulating parts of the surface.

The steady-state current was obtained by integrating the concentration gradient at the electrode surface, multiplied with the diffusion coefficient and the Faraday constant (**Equation 4.9**).

$$i_{T,\infty} = nFD\int\left(\frac{\partial c_x}{\partial x} + \frac{\partial c_y}{\partial y} + \frac{\partial c_z}{\partial z}\right)dA \qquad \text{Equation 4.9}$$

The concentration of the oxidized species is normalized with respect to the bulk concentration and the current is normalized with respect to the steady-state current (the probe is far away from the substrate). The solution of the diffusion equation and the

steady-state current is derived using the COMSOL Multiphysics 3.4 module, a commercial finite element modeling software. To simplify the simulation, the geometry of tip is cut in half in respect to the plane of symmetry.

4.3.1.1 Influence of RG value on steady-state current

The RG value is defined as the ratio of the radius of the insulating sheath to the radius of the electroactive surface as described in section 2.2.2. As shown in **Figure 4.22**, RG values for the AFM tip-integrated disk nanoelectrode is altered depending on the milling depth from the apex of the tip.

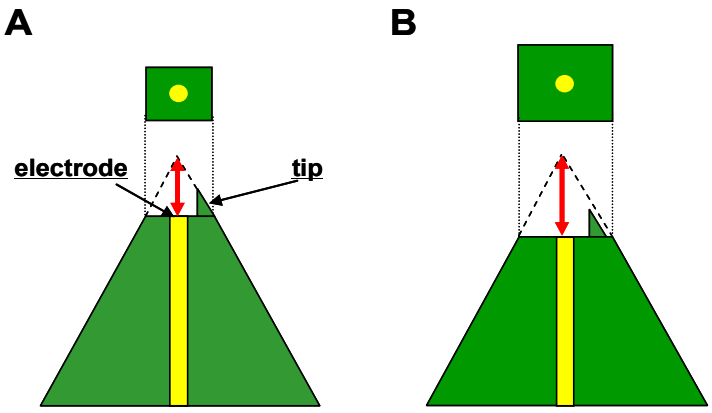

Figure 4.22 Schematic of the side view of AFM-SECM probes, which show different milling depths from the apex of the probe. RG values are different; (A) has a smaller RG value compared to (B).

The influence of RG value on the steady-state current response was investigated by simulation. For the simulation, the layout of probes had the same dimensions as the fabricated probes with a pyramidal shape of the tip having a base of 4 x 4 μm^2 and a slope of 54.74º. The AFM tip was not considered to simplify the simulations, as it was calculated that the diffusion to the tip is blocked by less than 5 % of the total diffusion towards the electrode. **Figure 4.23** shows the relationship between RG value and steady-state current obtained from the simulations. It is apparent from this figure that a smaller RG value leads to a larger steady-state current. This can be explained using the concentration profiles shown in **Figure 4.24.** The probes with smaller RG value have a larger diffusion area due to additional fractions of diffusion from behind the plane.

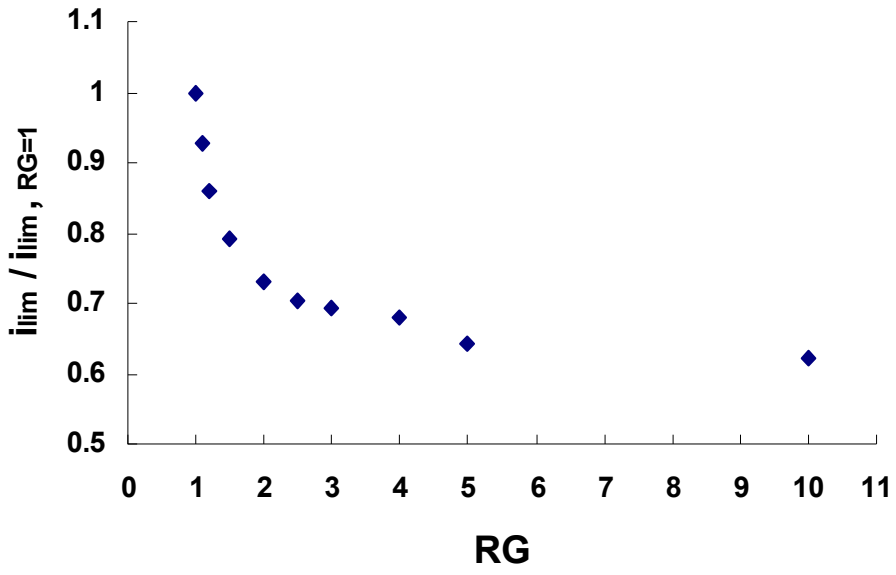

Figure 4.23 The relationship between RG value and steady-state current. The steady-state current is normalized to the current obtained at RG = 1.

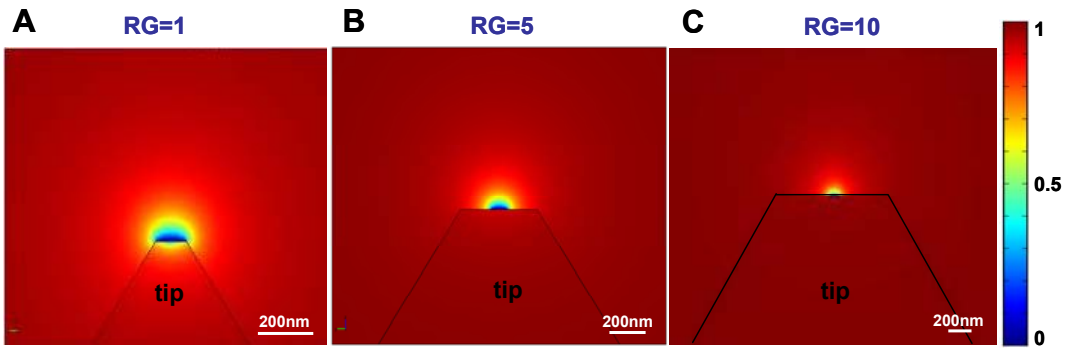

Figure 4.24 Side views of normalized concentration profiles for an oxidized species at AFM-SECM probes with (A) RG = 1, (B) RG = 5 and (C) RG = 10. The diameter of the electrodes was defined at 100 nm for all probes.

Derived from **Figure 4.23,** there is only a small influence of the RG value on the steady-state current in the range of RG = 5 to RG = 10. However, there is a significant increase of the current in the range of RG = 1 to 5. Therefore, it can be assumed that the probes with RG = 5 have a similar electrochemical characteristic as probes with a RG = 10. With a similar electrochemical response, a smaller RG value is preferential since a thin insulation layer has a lower probability to touch the sample surface. The following simulation results were obtained with RG values in the range of 1 to 5.

4.3.1.2 Simulations of approach curves

Simulations of approach curves for AFM tip-integrated disk nanoelectrode were performed. For the approach curves, the normalized diffusion-limited currents were calculated in respect to variations of the normalized distances. **Figure 4.25** shows examples of concentration profile when the AFM tip is in contact with an insulating and

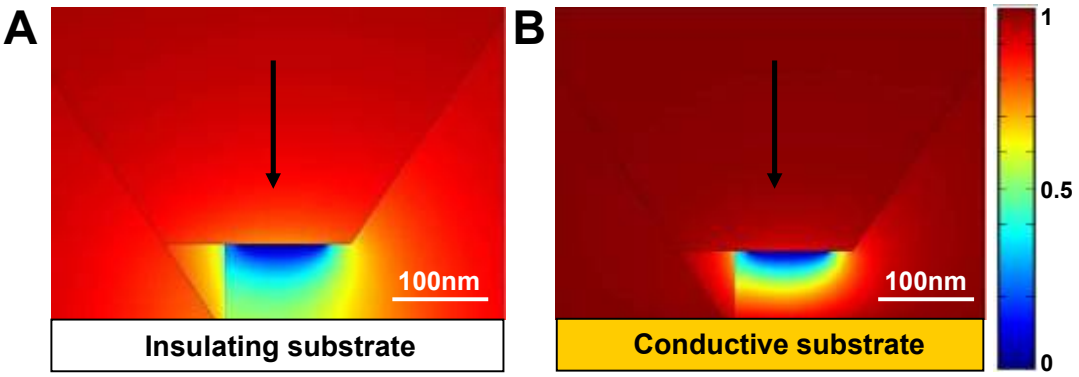

Figure 4.25 Side views of normalized concentration profiles of an oxidized species at an AFM-SECM probe. (A) The tip contacts an insulating substrate. (B) The tip contacts a conductive substrate.

a conductive surface, respectively. When the probe is approached in close vicinity to an insulating substrate, the current decreases since the hemispherical diffusion of the redox mediator towards the electrode is hindered. In contrast, the current increases if the probe is approached in close vicinity to a conductive substrate as the redox mediator is recycled at the surface of the substrate.

Figure 4.26 shows simulated approach curves for RG = 2 and RG = 5, respectively. This RG values have been chosen as the fabricated AFM-SECM probes presented in this thesis have RG values in this range. The distance (d) is normalized to the radius of the electrode (a) and the minimum normalized distance is determined by the length of the AFM tip, which equals the radius of electrode in this simulations. Again, the current is normalized to the steady-state current in bulk solution. From the graphs, it is

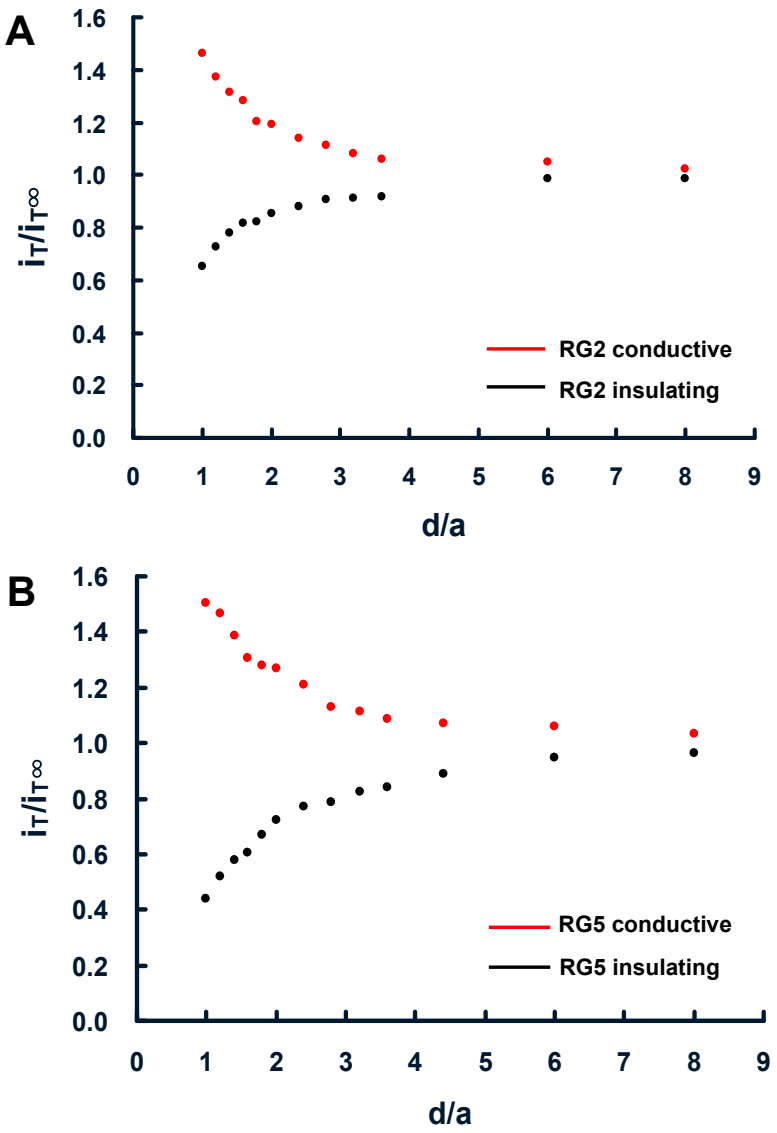

Figure 4.26 Simulated approach curves for (A) RG = 2 and (B) RG = 5. For both curves, the red curve corresponds to the normalized current as the probe is approaching a conductive substrate and the black curves refer to approaches towards an insulating substrate.

apparent that a probe with RG = 5 shows a more distinct negative approach curve (insulating substrate). The diffusion is blocked more efficiently with a larger size of the insulation sheath, which was modeled for microelectrodes by Bard and coworkers in the early days of SECM[24]. However, it has to be noted that larger RG values, in the range of 1 to 5, do not guaranty a better contrast between insulating and conductive surfaces in imaging experiments, if normalized values are displayed. Since the steady-state current in the bulk solution increase with decreasing RG values (**Figure 4.23**), the discrepancy of obtained currents at insulting and conductive surfaces can be larger with small RG values when displayed as normalized current values, which is typically done for approach curves.

4.3.1.3 Simulations of line scans at steady-state condition

The steady-state current response for a line scan was simulated using following conditions. As shown in **Figure 4.27**, the probe is scanned across a flat surface consisting of two conductive islands in an insulating plane. The distance between the electrode and the surface of the sample (d) was normalized to the radius of electrode (a) and set to 1. The AFM tip was not accounted to simplify the simulation. The distance between the islands was set to 2a and the width of islands was also set to 2a. Also, the length of the scan (L) was normalized in respect to the radius of the electrode and the center point between the two islands was set to zero. Therefore, scanning from the center point to the right direction is marked as positive direction and to the left as negative direction. **Figure 4.28** shows the changes of the steady-state current according to the scan distance along

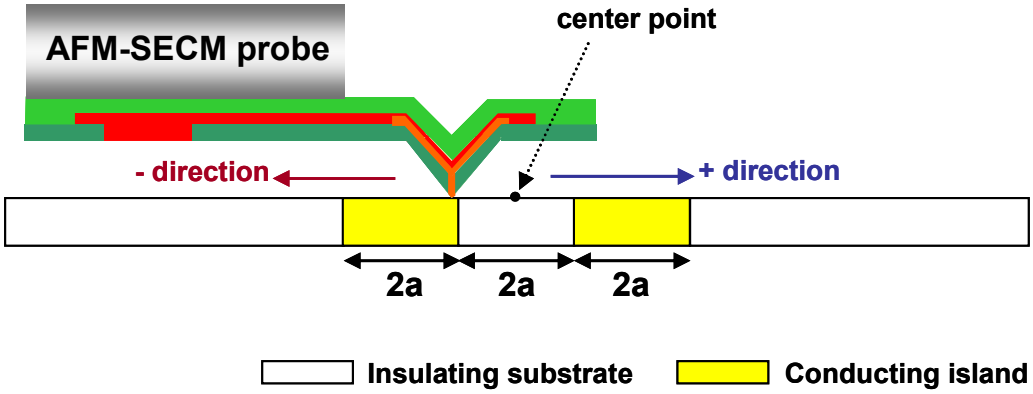

Figure 4.27 Schematic of simulating a line scan. The distance between conductive islands and width of the islands were set to 2a (a is the radius of electrode).

the electrode to the sample surface for probes with RG = 1 and RG = 5, respectively. The currents were normalized to the steady-state currents in bulk solution. The maximum change in the normalized current between the two conductive islands is indicated in the figure and it is larger for RG = 5 than RG = 1.

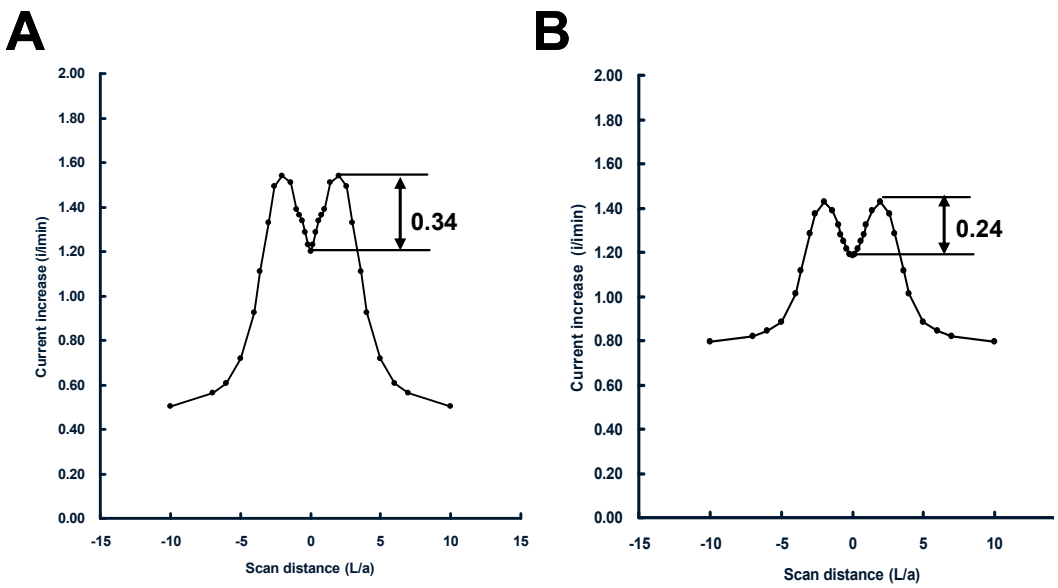

Figure 4.28 Simulated relative current profiles for probes with (A) RG = 5 and (B) RG = 1 for line scans consisting of two conductive islands. The maximum change of current between the two conductive islands were 0.34 and 0.24 for RG = 5 and RG = 1, respectively.

However, the steady-state current for RG = 1 is approx. 1.5 times larger than for RG = 5 as shown in **Figure 4.23**. Consequently, the relative current between the highest current values marking the conductive islands and the minimum current marking the insulating part between the islands is larger for RG = 1 than for RG = 5. For example, if the steady-state current is 100 pA for a probe with RG = 1, then the steady-state current would be 64 pA for a probe with RG = 5 assuming the same electrode size. Therefore, the maximum current change would be 24 pA and 21 pA for RG = 1 and RG = 5, respectively. Consequently, the sensitivity is better for larger RG value based on the influence of the RG value on approach curves; however the ability to resolve two

conductive island separated by an insulating area maybe improved with small RG values in the range of RG 1 to 5.

4.3.2 Scanning electron microscopy

FIB milling the batch-fabricated AFM-SECM probes resulted in AFM probes with integrated disk nanoelectrodes, showing a charging current less than 10 pA determined by CV. **Figure 4.29** shows SEM images of combined AFM-SECM tips after exposure of the electroactive area. Milling steps were performed as described in section 4.2.3.8. The targeted radius of the integrated electrodes was 100 nm, however as shown in **Figure 4.29**, there were small deviations from the targeted value; the electrode shown in **Figure 4.29A** has approx. a radius of 110 nm and a radius of approx. 90 nm was obtained for the electrode shown in **Figure 4.29B**. The length of the tip was designed to be in the range of 150 − 200 nm to obtain an AFM tip length, which is shorter than the diameter of the integrated electrode.

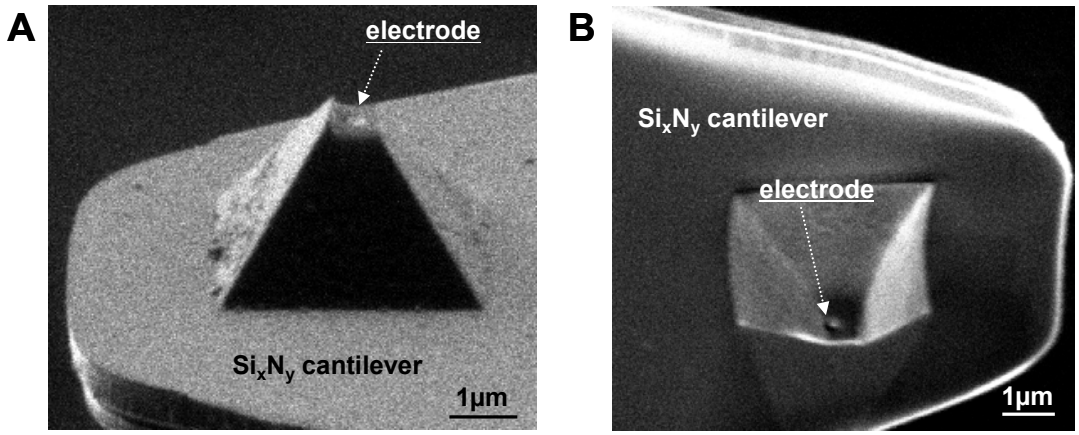

Figure 4.29 SEM images of AFM-SECM probes with integrated disk nanolectrodes. The radii of electrodes were determined as approx. 110 nm and 90 nm for (A) and (B), respectively. Tip height was approx. 180 nm for the both probes.

4.3.3 Electrochemical characterization

Cyclic voltammetry was used to evaluate the quality and electrochemical behavior of tip-integrated disk nanoelectrodes after exposure of the electroactive area by FIB milling. **Figure 4.30** shows CVs, which correspond to probes A and B shown in **Figure 4.29,** respectively. The experimentally obtained steady-state currents are in good agreement with the theoretically determined values, based on modeling using a

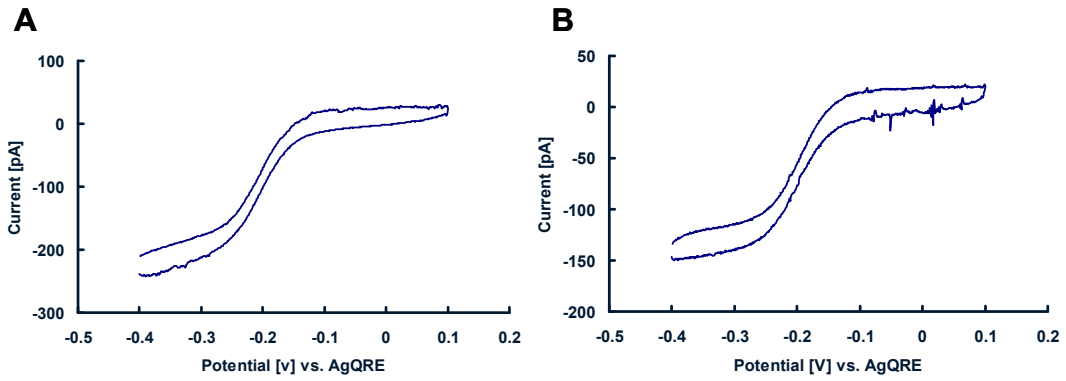

Figure 4.30 CVs obtained in 5 mM $Ru(NH_3)_6^{3+}$ solution containing 0.5 M KCl as supporting electrolyte. CVs were recorded with a scan rate of 0.1 V s^{-1}. The CVs correspond to probes (A) and (B) in Figure 4.29.

commercially available software package (COMSOL multiphysics 3.4). A value of approx. 130 pA was calculated for a disk nanoelectrode with a radius 100 nm and a RG value of 3. The deviation observed may be related to slight deviation of thickness of insulation sheath and the actual size of the exposed electroactive area.

4.3.4 Approach curves

The faradaic current and deflection of AFM-SECM probe were simultaneously monitored when the tip was approached to a conductive and insulating surface, respectively. Test substrates were prepared by deposition of Au or Si_xN_y films on silicon substrates. **Figure 4.31** shows representative approach curves. The measured currents were normalized in respect to the steady-state currents derived from recorded CV in bulk solution. The cantilever deflection typically displayed in volts was converted to distance (nm) signal using the cantilever sensitivity. The cantilever sensitivity was obtained from

the deflection-distance curve measured in the contact region at the Au-coated substrate prior to the approach curve measurements. The x-scale of tip-sample distance is approximated from the time-signal curve and the total traveled distance. The distance "zero" on the x-scale represents the point where the tip was in physical contact with the sample surface and the cantilever approach was stopped as the AFM feedback loop was activated. The probe was held at a potential of -0.5 V (vs. AgQRE) for reduction of 5 mM $Ru(NH_3)_6^{3+}$ in aqueous solution containing 0.5 M KCl.

Positive feedback was observed when the probe was approaching a conductive substrate due to the recycling of the redox mediator (**Figure 4.31A**). On the other hand, negative feedback is observed as the probe was approaching an insulating substrate due

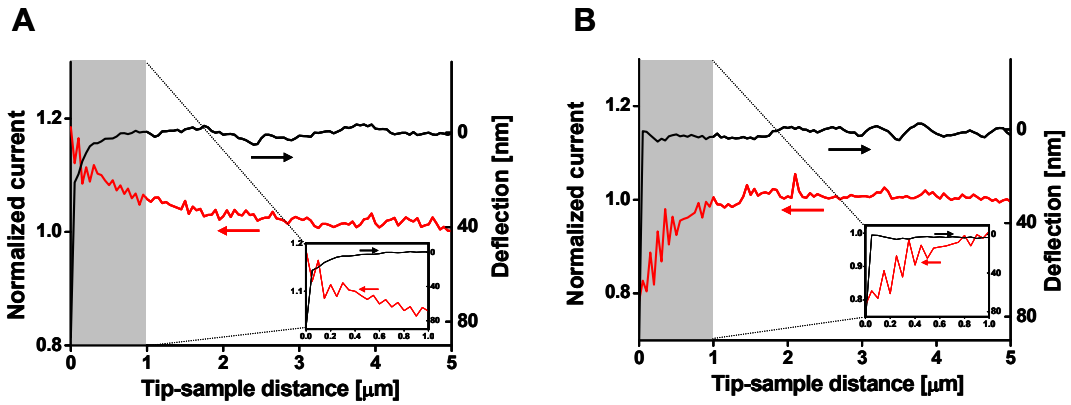

Figure 4.31 The AFM-SECM approach curves towards (A) a conductive surface (Au) and (B) an insulating surface (Si_xN_y). The probe was biased at -0.5 V (vs. AgQRE) in aqueous solution containing 5 mM $Ru(NH_3)_6^{3+}$ and 0.5 M KCl. The gray-marked sections are shown in the insets (A) and (B) as magnified views. The AFM-SECM tip had a radius of electrode of approx. 100 nm and a tip height of approx. 180 nm.

to the hindered hemispherical diffusion of the mediator towards the integrated electrode (**Figure 4.31B**). This result is in good agreement with the simulated approach curve shown in **Figure 4.26**. It should be again noted that the distance zero represents the point where the tip was in physical contact with the sample surface and the distance between the electrode and the surface is determined by the tip height. Since the tip height was approx. 180 nm, this corresponds to approx. twice of the normalized distance (d/a) in the simulated approach curve shown in **Figure 4.26**.

4.3.5 Combined AFM-SECM imaging

Simultaneously AFM-SECM imaging was performed at the substrates described in section 4.2.2.

Figure 4.32 shows simultaneously acquired topographical and electrochemical images of a 50 nm Au strip patterned at a Si_xN_y substrate. AFM imaging was performed in contact-mode and the simultaneously recorded SECM image was obtained in feedback mode biasing the tip-integrated disk nanoelectrode at a potential of -0.6 V (vs. AgQRE) in an aqueous solution containing 5 mM $Ru(NH_3)_6^{3+}$ and 0.5 M KCl. For the electrochemical images (displayed in **Figure 4.32B** and **D**), an increase in current was observed on the conductive Au strip based on a positive feedback effect, whereas the current is decreased when the combined tip is scanned over the Si_xN_y surface showing the expected negative feedback effect. A dirt particle on the Au strip, which is clearly visible in the topography, could be also resolved in the electrochemical image. Due to the insulating nature of this particle, the current was decreased by the lack of recycling of redox mediator at this spot.

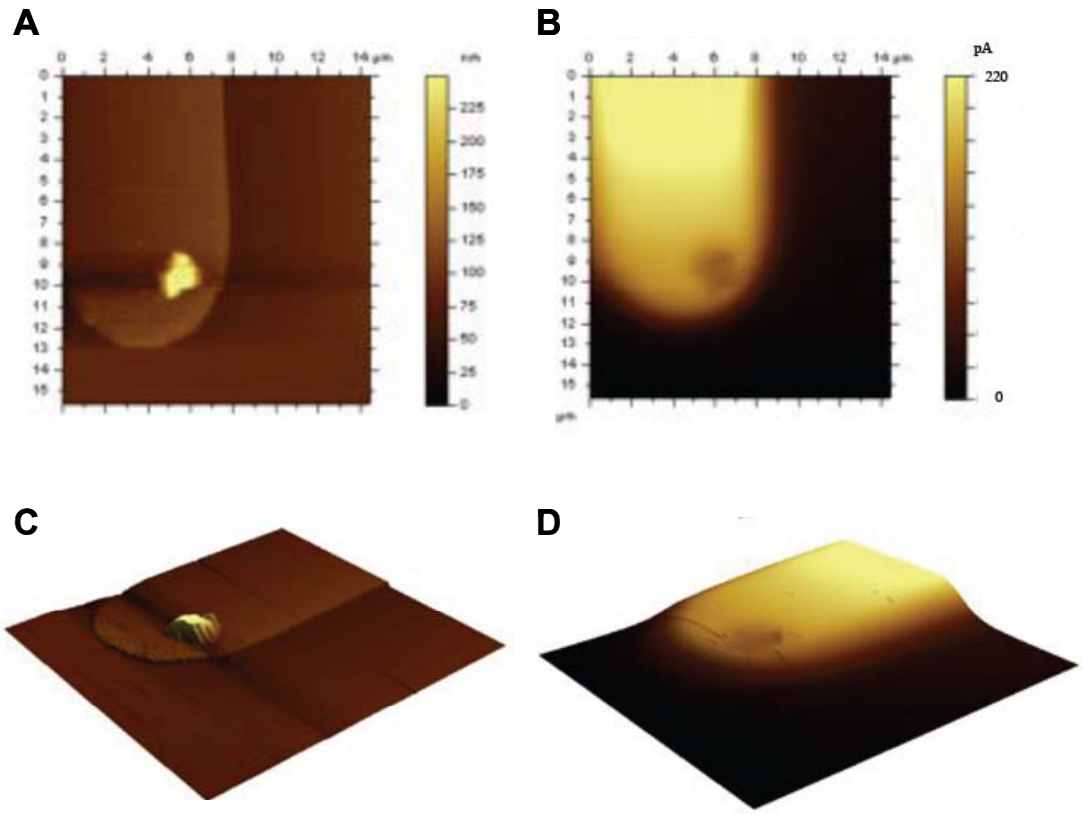

Figure 4.32 Simultaneously recorded (A) topography and (B) electrochemical images in 5 mM $Ru(NH_3)_6^{3+}$ / 0.5 M KCl. The AFM-SECM probe was scanned in contact mode with 0.25 lines s^{-1} and the integrated electrode was biased at -0.6 V (vs. AgQRE). (C) and (D) are 3D views of (A) and (B), respectively. The electrode had a radius of approx. 90 nm and a tip height of approx. 150 nm.

Figure 4.33 shows the zoomed images for topography and electrochemical image of the dirt particle, respectively. The electrochemical image still shows well resolved particle image even in higher magnification. However, it was observed that the electrochemical image is broader compared to topographical image. Due to the signal generation

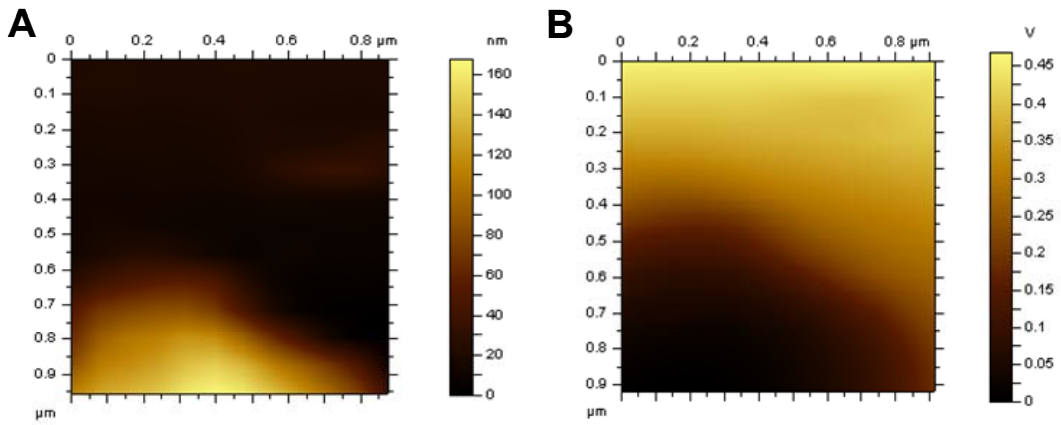

Figure 4.33 Zoomed area showing detail of the dirts particle depicted in figure 4.32. Simultaneously recorded (A) topography and (B) electrochemical images in 5 mM $Ru(NH_3)_6^{3+}$ / 0.5 M KCl.

mechanism of SECM in dependence of the distance of the electrode to the sample surface, the obtained electrochemical image shows broadened features compared to the topography resulting from the simultaneously obtained AFM data. This effect scales with the size of the electrode and the distance from the sample surface. AFM is only sensing the interacting force between the sharp apex of the tip and sample surface. However, SECM is sensing electrochemical characteristics within the hemispherical diffusion area. For the AFM-SECM probe used in this experiment, the electrode radius is larger than the apex of the AFM tip. Secondly, the elevated particle makes the electrochemical image broader. From the topography, it is shown that the height of particle is maximum approx. 170 nm. This height is comparable to the length of tip (approx. 150 nm) and the steep edge of feature can prevent the electrode scans in close vicinity near the edge. Thirdly, the distance offset between the tip and electrode can contribute to the broadening of the electrochemical image. As shown in **Figure 4.19**, there is a distance offset between tip

and electrode. Typically, this offset is in the range of 100 – 200 nm. This offset is also visible when scanning a sample with alternating conductive and insulating features, as shown at the second example, which was used in the imaging experiments. **Figure 4.34** shows simultaneously acquired topographical and electrochemical images of an alternating pattern of conductive and insulating stripes consisting of 120 nm thick Au stripes and insulating Si_xN_y stripes. The width of the conductive Au lines was approx. 300 – 400 nm and distances between conductive lines were approx. 600 nm (**Figure 4.1**). Again, images were recorded in AFM contact-mode at a rate of 0.23 lines s^{-1} (original scan size: 15 x 15 μm^2) and the integrated electrode was biased at -0.5 V (vs. AgQRE) in an aqueous solution containing 5 mM $Ru(NH_3)_6^{3+}$ and 0.5 M KCl as supporting electrolyte.

The conductive lines were clearly resolved in both the topography and electrochemical image. A slight offset was observed between the most elevated point of topography and the maximum current in the electrochemical image. This deviation may be related to the fact that the tip and electrode are not perfectly parallel to the conductive lines and/or that cantilever was tilted and not perfectly perpendicular to the substrate.

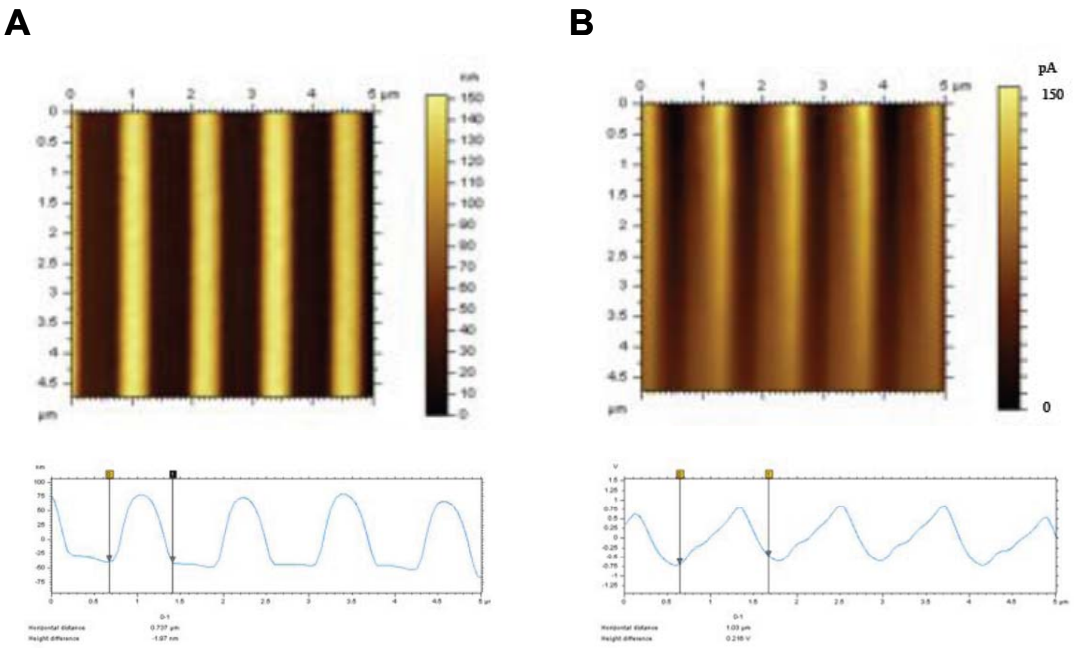

Figure 4.34 Simultaneously acquired (A) topography and (B) electrochemical image (showing a cross-sectional scan, bottom). The AFM-SECM probe was scanned in AFM contact-mode and a bias of -0.5 V (vs. AgQRE) in 5 mM $Ru(NH_3)_6^{3+}$/0.5 M KCl was applied at the integrated electrode. The electrode had a radius of approx. 100 nm and the tip height was approx. 180 nm.

Figure 4.35 shows the zoomed images of conductive lines of **Figure 4.34**. Clearly resolved electrochemical image are visible. The deviation seems to be contributed by the offset distance between the tip and electrode.

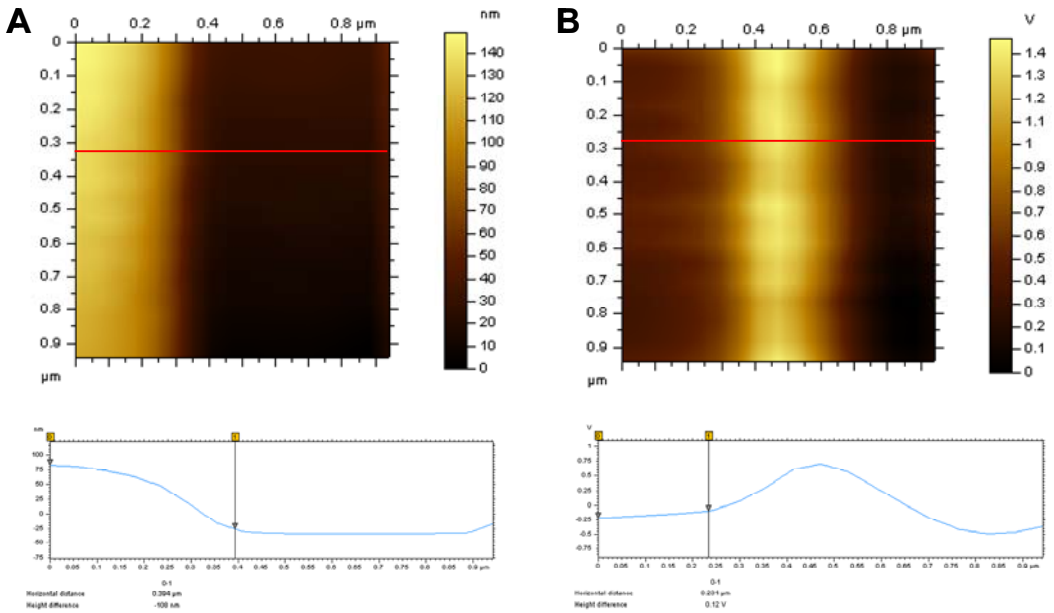

Figure 4.35 Zoomed images of conductive lines in figure 4.34. Simultaneously recorded (A) topography and (B) electrochemical images (showing a cross-sectional scan, bottom) in 5 mM $Ru(NH_3)_6^{3+}$ / 0.5 M KCl.

4.4 Final remarks

AFM tip-integrated disk nanoelectrodes were batch-fabricated and evaluated as advanced probes for high resolution simultaneous topographical and electrochemical imaging. Since the fabrication scheme is based on a reproducible semi batch-fabrication process at a wafer level, significantly reduced time and cost for the fabrication are additional the advantageous aspects. The radii of the electrodes were design to have radii in the range of 50 – 100 nm for high resolution combined AFM-SECM measurements.

Simulation studies were performed for the electrochemical characteristics of AFM tip-integrated disk nanoelectrodes. The simulation dealt with influence of RG value on steady-state current, approach curves and line scans of modeled substrate. Based on the

simulation results, a small RG value approaching unity is advantageous showing increased steady-state current when the electrode is close to the tip apex.

The fabricated AFM-SECM probes were electrochemically characterized by CV and approach curve were recorded, which were in good agreement with the simulation results. Also, the performance of the probes was demonstrated by simultaneous topographical and electrochemical imaging using model samples consisting of patterns of conductive and insulating features. In this imaging experiment, high resolution of the electrochemical imaging capability was demonstrated by imaging small size of a dirt particle and approx. 300 – 400 nm width of conductive line patterns.

The lateral resolution can be further improved with this approach since the radii of electrodes can be further reduced by FIB milling of the hole. It is expected that electrodes with 25 nm radius are feasible given the nominal beam diameter of the ion beam. However, the FIB milling needs to be deliberately performed since the length of the tip determines the working distance, which is as critical as the size of the electrode. Also, the tip needs to be formed as close as possible to the electrode to prevent the offset between the topography and electrochemical information.

4.5 References

1. P. G. Nicholson, S. Zhou, G. Hinds, A. J. Wain, A. Turnbull, Electrocatalytic activity mapping of model fuel cell catalyst films using scanning electrochemical microscopy. *Electrochimica Acta* 2009, *54*. 4525-4533.

2. L. Niu, Y. Yin, W. Guo, M. Lu, R. Qin, S. Chen, Application of scanning electrochemical microscope in the study of corrosion of metals. *Journal of Materials Science* 2009, *44*. 4511-4521.

3. P. R. Roberge, Handbook of Corrosion Engineering; McGraw-Hill: New York. 2000.

4. A. Schulte, W. Schuhmann, ChemInform Abstract: Single-Cell Microelectrochemistry. *ChemInform* 2008, *39*. no-no.

5. M. A. Alpuche-Aviles, D. O. Wipf, Impedance Feedback Control for Scanning Electrochemical Microscopy. *Analytical Chemistry* 2001, *73*. 4873-4881.

6. D. P. Burt, N. R. Wilson, J. M. R. Weaver, P. S. Dobson, J. V. Macpherson, Nanowire Probes for High Resolution Combined Scanning Electrochemical Microscopy − Atomic Force Microscopy. *Nano Letters* 2005, *5*. 639-643.

7. E. N. Ervin, H. S. White, L. A. Baker, C. R. Martin, Alternating Current Impedance Imaging of High-Resistance Membrane Pores Using a Scanning Electrochemical Microscope. Application of Membrane Electrical Shunts To Increase Measurement Sensitivity and Image Contrast. *Analytical Chemistry* 2006, *78*. 6535-6541.

8. A. Hengstenberg, C. Kranz, W. Schuhmann, Facilitated Tip-Positioning and Applications of Non-Electrode Tips in Scanning Electrochemical Microscopy Using a Shear-Force-Based Constant-Distance Mode. *Chemistry – A European Journal* 2000, *6*. 1547-1554.

9. P. I. James, L. F. Garfias-Mesias, P. J. Moyer, W. H. Smyrl, Scanning Electrochemical Microscopy with Simultaneous Independent Topography. *Journal of The Electrochemical Society* 1998, *145*. L64-L66.

10. B. B. Katemann, A. Schulte, W. Schuhmann, Constant-distance mode scanning electrochemical microscopy (SECM)-part 1: Adaptation of a non-optical shear-force-based positioning mode for SECM tips. *chemistry a european journal* 2003, *9*. 2025-2033.

11. C. Kranz, G. Friedbacher, B. Mizaikoff, A. Lugstein, J. Smoliner, E. Bertagnolli, Integrating an Ultramicroelectrode in an AFM Cantilever: Combined Technology for Enhanced Information. *Analytical Chemistry* 2001, *73*. 2491-2500.

12. M. Ludwig, C. Kranz, W. Schuhmann, H. E. Gaub, Topography feedback mechanism for the scanning electrochemical microscope based on hydrodynamic forces between tip and sample. *Review of Scientific Instruments* 1995, *66*. 2857-2860.

13. J. V. Macpherson, P. R. Unwin, Combined Scanning Electrochemical−Atomic Force Microscopy. *Analytical Chemistry* 2000, *72*. 276-285.

14. K. Maruyama, H. Ohkawa, S. Ogawa, A. Ueda, O. Niwa, K. Suzuki, Fabrication and Characterization of a Nanometer-Sized Optical Fiber Electrode Based on Selective Chemical Etching for Scanning Electrochemical/Optical Microscopy. *Analytical Chemistry* 2006, *78*. 1904-1912.

15. D. Oyamatsu, Y. Hirano, N. Kanaya, Y. Mase, M. Nishizawa, T. Matsue, Imaging of enzyme activity by scanning electrochemical microscope equipped with a feedback control for substrate-probe distance. *Bioelectrochemistry* 2003, *60*. 115-121.

16. T. H. Treutler, G. Wittstock, Combination of an electrochemical tunneling microscope (ECSTM) and a scanning electrochemical microscope (SECM): application for tip-induced modification of self-assembled monolayers. *Electrochimica Acta* 2003, *48*. 2923-2932.

17. J. P. Cleveland, S. Manne, D. Bocek, P. K. Hansma, A nondestructive method for determining the spring constant of cantilevers for scanning force microscopy. *Review of Scientific Instruments* 1993, *64*. 403-405.

18. A. R. Hodges, K. M. Bussmann, J. H. Hoh, Improved atomic force microscope cantilever performance by ion beam modification. *Review of Scientific Instruments* 2001, *72*. 3880-3883.

19. M. J. Madou, Fundamentals of Microfabrication: The Science of Miniaturization, 2nd ed., Boca Raton, FL: CRC Press. 2002.

20. M. J. Loboda, J. A. Seifferly, Chemical influence of inert gas on the thin film stress in plasma-enhanced chemical vapor deposited a-SiN :H films. *Journal of materials research* 1996, *11*. 391-398.

21. S. Deladi, et al., Fabrication of micromachined fountain pen with in situ characterization possibility of nanoscale surface modification. *Journal of Micromechanics and Microengineering* 2005, *15*. 528.

22. G. W. Hsieh, T. Ching-Hsiang, L. We-Chih, L. Chao-Chiun, L. Yu-Wen, Bond-and-transfer scanning probe array for high-density data storage. *Magnetics, IEEE Transactions on* 2005, *41*. 989-991.

23. J. Wiedemair, N. Menegazzo, J. Pikarsky, K. S. Booksh, B. Mizaikoff, C. Kranz, Novel electrode materials based on ion beam induced deposition of platinum carbon composites. *Electrochimica Acta* 2010, *55*. 5725-5732.

24. A. J. Bard, M. V. Mirkin, P. R. Unwin, D. O. Wipf, Scanning electrochemical microscopy. 12. Theory and experiment of the feedback mode with finite heterogeneous electron-transfer kinetics and arbitrary substrate size. *The Journal of Physical Chemistry* 1992, *96*. 1861-1868.

5 AFM tip-integrated potentiometric sensors (sub-micro pH electrode)

Within this chapter, AFM tip-integrated potentiometric sensors based on sub-micro solid-state electrodes will be introduced as imaging pH sensors. Antimony/antimony oxides and iridium/iridium oxides were used, as these materials can be integrated in AFM probes by standard cleanroom processes. The fabricated sensors were thoroughly characterized.

5.1 Motivation

In 1909 Soren P.L. Sorenson introduced the pH scale[1]. Mapping pH changes plays a significant role in a variety of research fields such as corrosion science, surface modifications, clinical, environmental, and food industry[1-7]. Particularly, the role of pH and mapping minute changes of pH in living systems including the human body has attracted extensive interests. In life sciences, hydrogen plays a key role as fuel in living systems[4]. For example, cells must communicate with each other to multiply or grow from a fertilized egg, which is a process where hydrogen acts as a source for electrons to be delivered for cell-to-cell communication[8]. Also, metabolic processes involve the regulation of intra- and extracellular pH, as protons react rapidly with species producing dissociated anions, and undissociated acid forms of metabolites[6]. Proteins such as enzymes show a pH-dependent activity. Changes in pH frequently induce alterations in

the 3-dimensional structure and charge of an enzyme or its substrate, which affects the rate of catalytic reactions[6]. Furthermore, it has been reported that the release of neurotransmitters is accompanied by pH changes in the brains extracellular space[3]. pH changes are also a critical parameter in corrosions sciences including the deterioration of coatings and degradation mechanism of metal and alloys. Besides, electrochemical deposition of metal layers from aqueous solution are greatly affected by the hydronium concentration[5]. It is known that the initial stage of corrosion includes critical information on corrosion mechanisms; hence, techniques providing pH information at the micro- or nanoscopic scale are required[2, 7]. For all of the listed examples, pH measurements in close vicinity to the area of interest with high spatial resolution may provide further information on the reaction mechanism, the reaction rate or the involved species themselves.

5.1.1 Localized pH measurements

As mentioned in section 2.1.3, the pH glass electrode is by far the most widely used pH sensor. However, it is intrinsically fragile in nature, which usually prevents *in vivo* applications. In addition, miniaturization appears difficult in respect to the internal reference electrodes. For this reason, alternative pH sensing approaches applicable to the microscopic regime with the capability of precise positioning at the sample surface is a prerequisite. Solid-state metal/metal oxide electrodes have been considered among the most promising candidates for miniaturized pH sensors[9-13].

Several approaches of miniaturized pH sensing schemes and their application for localized pH measurements using metal/metal oxide electrodes have been described[14-19].

Among them, the most promising approaches are based on metal/metal oxide microelectrodes in combination with SECM experiments[15-19] providing localized pH mapping at the sample surface. Antimony/antimony oxide electrodes, which are fairly easy to prepare, and iridium/iridium oxide[9] are considered the most promising material combinations among the metal/metal oxides reported to date.

Further miniaturization and precise positioning along with complementary topographical information may be achieved by integrating the metal/metal oxide electrode into an AFM tip. As described for integrated amperometric electrodes, AFM provides a precisely controlled working distance independent of the properties of the sample surface along with high resolution of the topographical information.

5.2 Experimental

5.2.1 Fabrication of AFM tip-integrated pH microsensors

Antimony oxide or iridium oxide based solid-state electrodes integrated into AFM tips were prepared by adapting the multi-step procedures similar to the fabrication method of AFM-SECM probes described in chapter 3. **Figure 5.1** shows a schematic outline of the fabrication process. Triangular-shaped conventional cantilevers (Veeco, Woodbury, NY) were used as basis for the tip-integrated pH microsensors. As the first step (**Figure 5.1A**), the reflective coating of the commercial silicon nitride cantilevers was removed by Au (GE-8110, Transene, Danvers, MA) and Cr etchant (CR7-S, Cyantek, Fremont, CA), respectively. After removing the backside metal layer, the cantilevers were cleaned in piranha solution (H_2SO_4 from Fisher Scientific, Pittsburgh, PA; 30 % H_2O_2 from JT Baker, Phillipsburg, NJ; ratio 4:1) at 120 ºC for 10 min prior to the metal

deposition. Subsequently, antimony or iridium metal layers were deposited using a RF sputter system (PVD75, Kurt J. Lesker, Pittsburgh, PA) equipped with a 3-inch target of antimony or iridium, respectively. For both metallizations, a shadow mask was used for patterning the connecting line between the contact pad and the integrated electrode.

Since the sputtered antimony and iridium films have high intrinsic stress in comparison to conventional Au electrode layers, the cantilevers showed bending once a film thickness of approx. 70 nm for antimony, and of approx. 40 nm for iridium was deposited (**Figure 5.2**). However, if pH measurements were performed at these thin film electrodes the pH response was not stable and varied significantly over time, which will be described in more detail in section 5.3. Multiple depositions were applied to increase the thickness of the pH-sensitive layer, as shown in **Figure 5.3**. Using this approach, a thin metal layer of Sb, Ir or Au was first deposited using a shadow mask, and then - in a second metallization step - a metal layer was locally deposited only at the tip area using a glass shadow mask. The purpose of the first metallization is to form an electrical

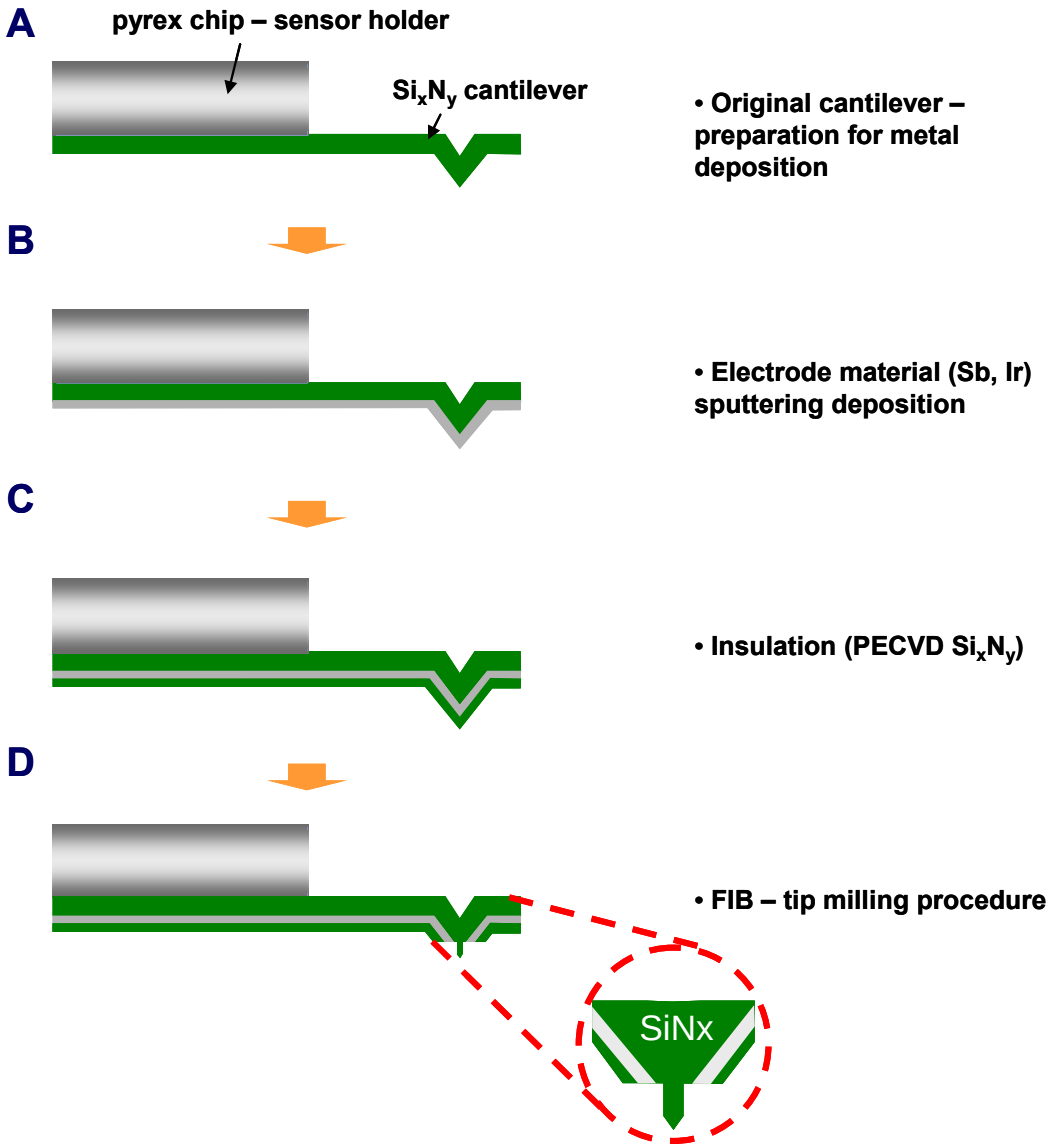

Figure 5.1 Schematic of the fabrication procedure for tip-integrated pH microsensors.

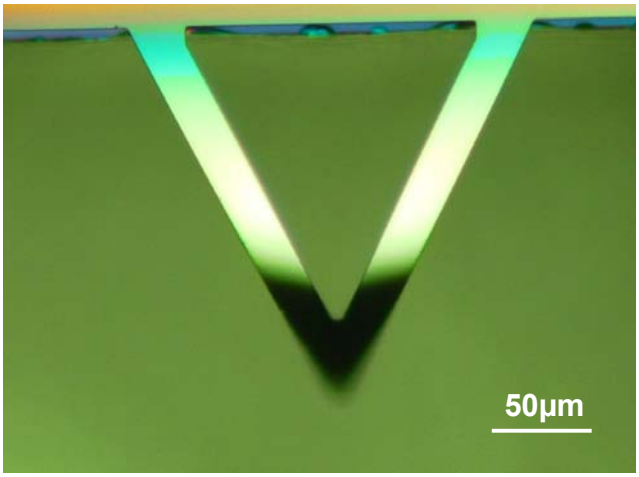

Figure 5.2 Optical micrograph of an AFM tip-integrated pH microsensor. The end of the cantilever is out of focus due to bending after sputtering deposition of a 130 nm thick iridium layer.

connection between the tip-integrated electrode and the contact pad avoiding bending of cantilevers by depositing only a thin layer of metal. In case of the antimony pH microsensor, the first metallization step deposited a layer with a thickness of 70 nm antimony using RF sputtering (PVD75 RF sputterer; power = 30 W, pressure = 5 mTorr, reaction gas was Ar) or alternatively a layer of 50 nm Au using DC sputtering (CVC DC sputterer; power = 2500 W). As the first metallization step when fabricating iridium-based pH microsensors, a layer of 30 nm iridium was deposited by RF sputtering (PVD75 RF sputterer; power = 45 W, pressure = 5 mTorr, reaction gas was Ar). Subsequently, the second metal deposition was deliberately located at the tip area using the glass shadow mask. The glass (Pyrex 7740) was diced into a rectangular shape of 18 x 15 μm^2 using a dicing saw (Kulick, San Jose, CA). After cleaning the shadow mask with piranha solution (H_2SO_4 from Fisher Scientific, Pittsburgh, PA; 30 % H_2O_2 from JT Baker, Phillipsburg,

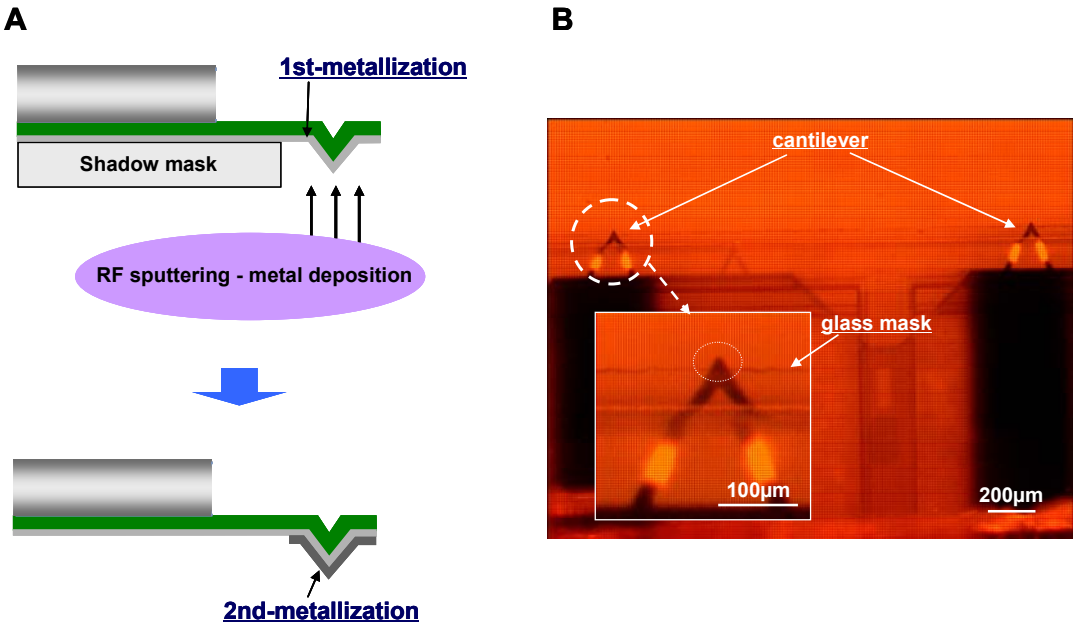

Figure 5.3 (A) Schematic of the metal deposition executed in two individual steps. In the first metallization step, the cantilever and tip were coated with a thin layer. Subsequently, the deposition was repeated localized at the tip area using a glass shadow mask. (B) Optical micrograph of the aligned glass mask for the second metallization step.

NJ; ratio 4:1), the second metal deposition was performed. For the antimony pH microsensor, the second metallization consisted of the deposition of 100 – 350 nm antimony using RF sputtering (PVD75 RF sputterer; power = 30 W, pressure = 5 mTorr, reaction gas was Ar).

For each deposition, the lowest possible power was selected, which was 30 W for the antimony deposition, and 45 W for iridium; this allows executing the process at the slowest possible deposition rate of approx. 48 Å/min, and approx. 8 Å/min, respectively. If films were deposited at faster rates - for example with a deposition rate of 25 Å/min for

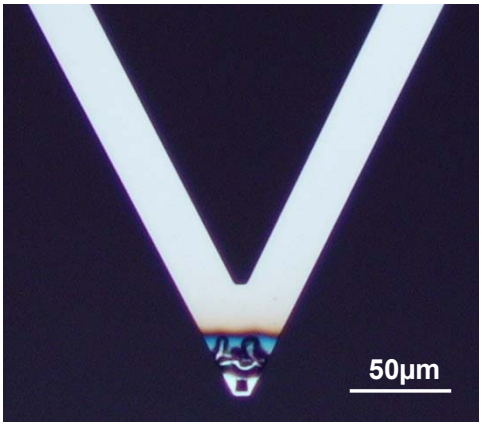

Figure 5.4 Optical micrograph of an iridium-coated AFM tip. 1400 Å of iridium was deposited at 25 Å/min in the second metallization step. As evident in the image, the film started peeling off after deposition.

iridium - the films have revealed the tendency to peel off or crack, as shown in **Figure 5.4**. In addition to the slow deposition rate, it was observed that a 30 min cooling period prior to venting the chamber assists in avoiding cracks, and for reducing the peeling problem. **Figure 5.5** shows an optical and a SEM image of an iridium-based pH microsensor after two metallization steps. 1800 Å iridium was deposited as the second metallization step, and no significant bending of the cantilever is evident after the deposition. Only the very end of the cantilever is slightly bent due to the localized thick film of iridium, however, this is not a practical problem, as the laser of the AFM system could still be focused at the cantilever. After the metallization step, the cantilevers were

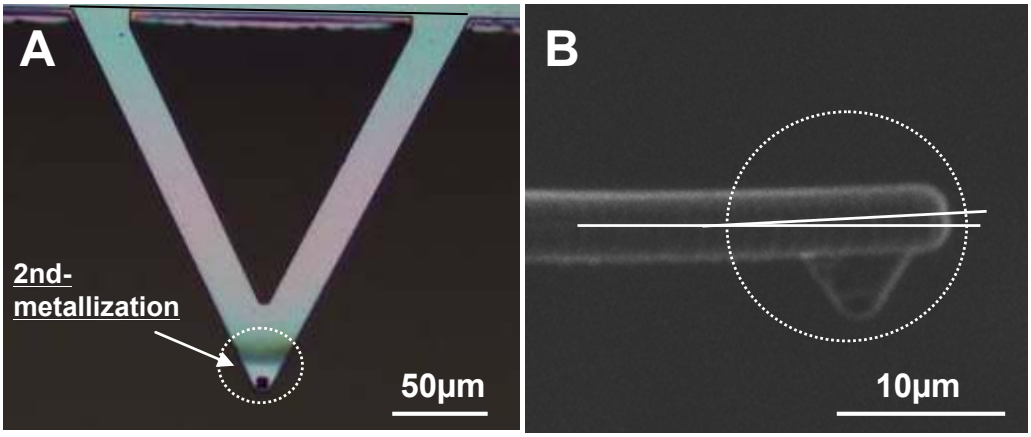

Figure 5.5 (A) Optical micrograph of the cantilever after second iridium deposition. A 1800 Å iridium layer was deposited as the second metallization step. (B) SEM image side view of circled area in A. The end of cantilever is slightly bent, though not critically for affecting AFM imaging.

insulated via PECVD Si_xN_y deposition. Details on the insulation conditions and the following FIB milling steps have been described in chapter 3.

Figure 5.6 shows SEM images of an antimony and an iridium pH microsensor after the electroactive area was exposed via FIB milling.

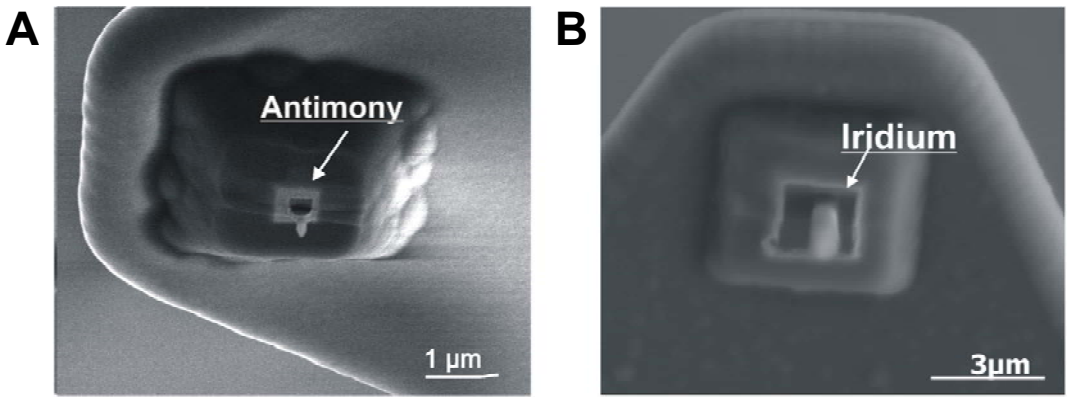

Figure 5.6 SEM images of (A) antimony pH microsensor, and (B) iridium pH microsensor after the electroactive area was exposed via FIB milling.

5.2.2 Characterization of the pH response

Electrochemical oxidation of the sputtered iridium electrode to form an anodic iridium oxide film (AIROF) and recording the potentiometric pH response of AFM tip-integrated pH microsensors was performed using a (bi)potentiostat (CHI842B, CH instrument, Austin, TX) .

For the formation of AIROF as pH sensitive layer, the potential applied to the iridium-modified cantilever was cycled in 0.5 M H_2SO_4 solution (Fisher Scientific, Pittsburgh, PA) between -0.25 and 1.25 V vs. SCE with a scan rate 0.1 V s^{-1}. Typically, 500 - 1000 cycles were applied at room temperature. The potentiometric pH responses of both the antimony and iridium pH microsensors were calibrated by open circuit potential (OCP) measurements as a function of the pH of the buffer solutions against an Ag/AgCl electrode. **Figure 5.7** shows a schematic of the set-up used for the pH response calibration. The pH microsensors were immersed in the electrochemical cell, and the measurement was performed in a series of pH buffered solutions within a pH range of 2 -

12. The buffered solutions with different pH values were pumped through the cell using a flow injection pump, and the OCP of the pH microsensors was measured. The measurement was paused during the solution exchange and resumed again after the solution was completely replaced with a new buffer at different pH. A digital pH meter (555A, Thermo Fisher Scientific Inc., Worcester, MA) was used to determine the pH values of the buffered solutions prior to the calibration experiment. When exchanging the solution within the cell, extended pump times were allowed to ensure that the solution was completely exchanged, which was monitored using a commercial stopwatch.

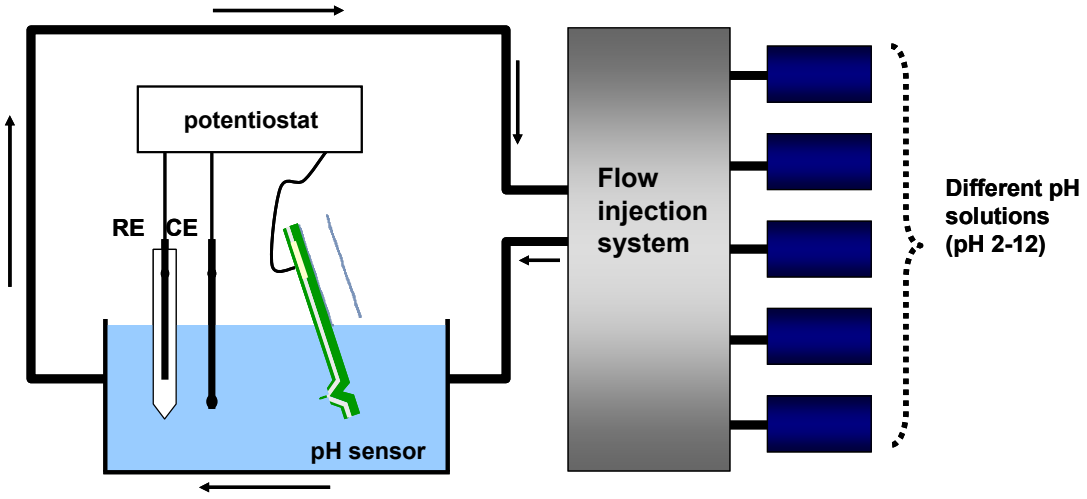

Figure 5.7 Schematic of the pH response calibration set-up.

pH response calibrations of antimony pH microsensors were performed in a 0.05 M Tris buffer solution[10-11]. 0.1 M universal buffer solution[9, 20] composed of 0.01 M H_3PO_4-H_3BO_3-CH_3COOH and 0.1 M KCl was used for calibrating the iridium pH microsensors. The pH value of all solutions was determined using a digital pH meter.

5.2.3 pH imaging

pH imaging experiments were performed using an AFM-SECM setup similar to the one described in chapter 3, except for minor modifications. The measurement was performed in the AFM liquid cell equipped with three electrodes, with the AFM tip-integrated pH microsensor serving as the working electrode (WE); a AgQRE and a platinum wire were used as reference electrode and counter electrode, respectively. A (bi)potentiostat (CHI842B, CH Instrument, Austin, TX) was utilized for OCP measurement and the output signal was logged via an AD channel of the AFM controller for correlating the potentiometric data with the topographical image. The AFM tip-integrated pH microsensors were mounted on conventional nose cone assemblies (Agilent Technologies, Chandler, AZ). The electrical connection of the pH microsensor to an external potentiostat was established using shielded cables (New England Wire Technologies, Lisbon, NH) with SMA connectors (Pasternack, Irvine, CA).

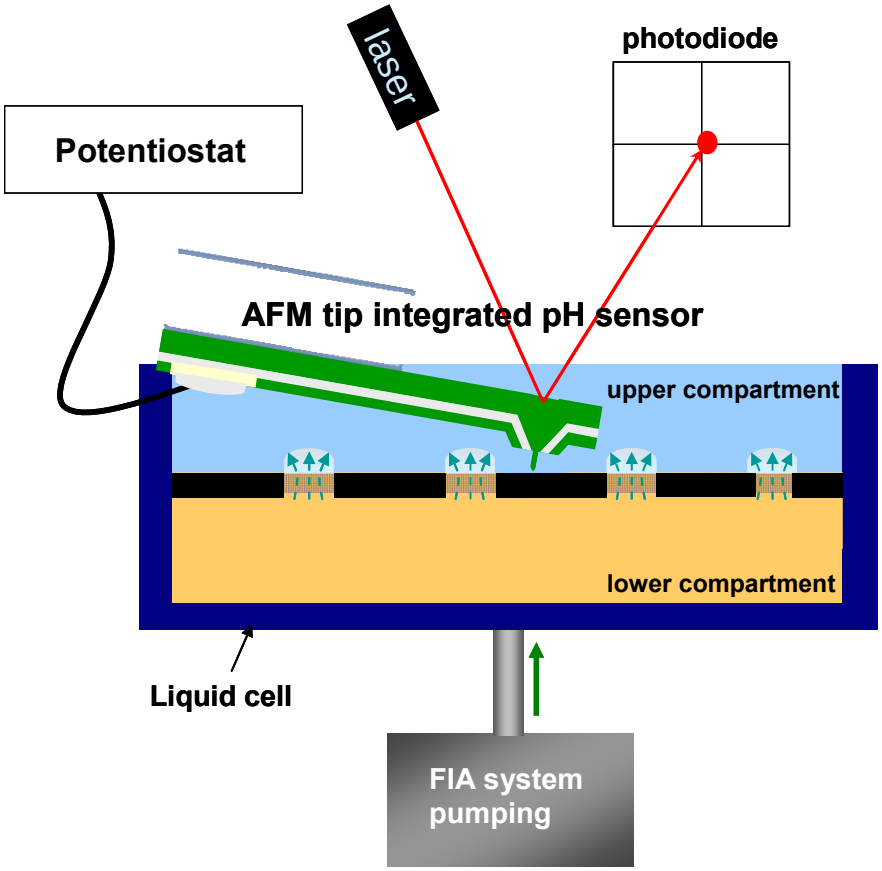

Figure 5.8 Schematic of the experimental set-up for pH imaging at a porous membrane substrate.

Two types of substrates have been tested to verify local pH measurements with the pH microsensors at the surface of the substrate. The first substrate was a porous membrane. An AFM liquid cell was designed to provide two separated compartments; an upper and a lower compartment, as shown in **Figure 5.8**. A soft polycarbonate membrane (Osmonics, Minnetonka, MN) or a rigid silicon membrane was used as separator between the two compartments.

The imaging experiment was designed such that the pH microsensor was scanned across the surface of the membrane in the upper compartment, which was filled with a

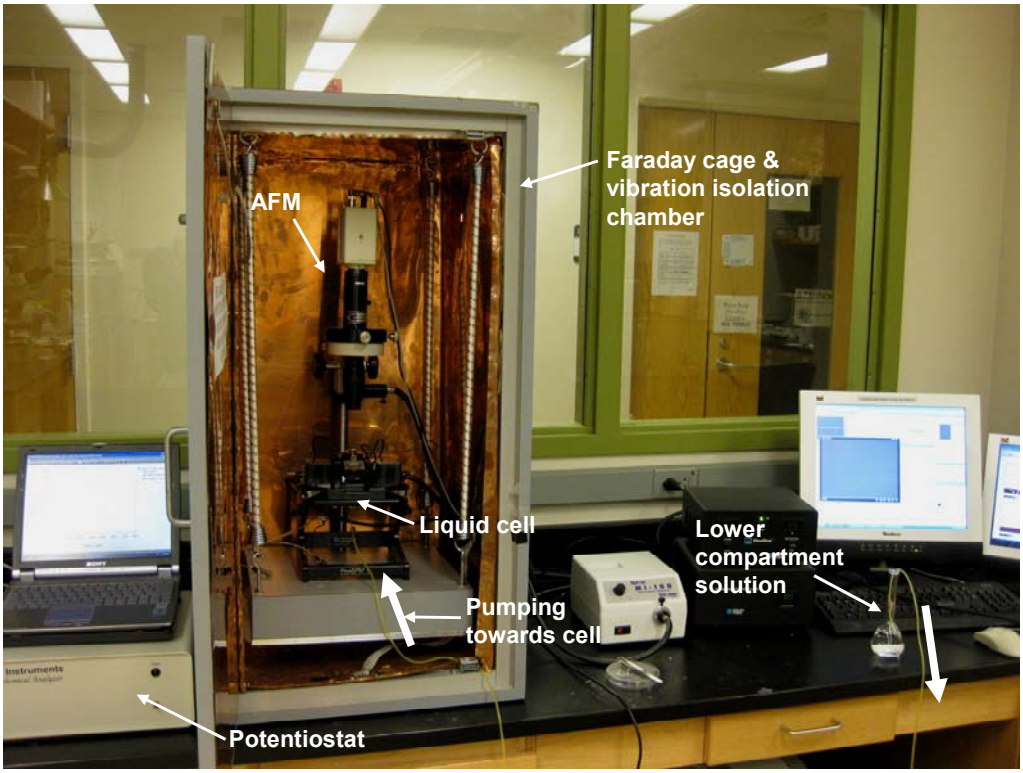

Figure 5.9 Image of the pH imaging set-up.

buffered solution of certain pH value. A solution with significantly different pH value was pumped through the pores from the lower into the upper compartment; thereby, the local pH value at the pores was changed. **Figure 5.9** shows an image of the pH imaging set-up.

The second sample used for pH imaging experiments was a glass-embedded microelectrode with a diameter of approx. 25 µm[19]. Potentials of -0.2 to -0.4 V vs. Ag/AgCl were applied to the microelectrode in 0.5 M KCl or phosphate buffer solution. Protons are depleted at the surface of the microelectrode due to the reduction of protons in this potential region. At a potential range of -0.2 to -0.4 V applied to the electrode the

reaction given in **Equation 5.1** occurs. **Figure 5.10** shows a schematic of the pH imaging set-up using a microelectrode as the test substrate.

$$Pt + H^+ + e^- \rightarrow Pt\text{-}H \qquad \text{Equation 5.1}$$

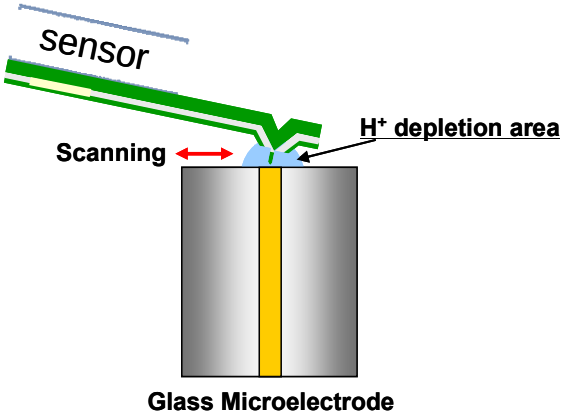

Figure 5.10 Schematic of a pH imaging set-up using a glass-embedded microelectrode as the test substrate.

5.3 Results and discussion

5.3.1 Potential response of AFM tip-integrated pH microsensors

5.3.1.1 Antimony pH microsensors

The pH response of the antimony pH microsensors was calibrated as described in section 5.2.2. **Figure 5.11** shows the measured pH response at different pH values of a buffered solution. The potential response was measured against changing the pH in steps of two pH units in the range pH 2 - 12. The pH changes were perfromed in both directions, i.e. from increasing pH 2 to 12 and vice versa. The pH values of the test

solution shown in the graph were determined with a pH meter prior to the calibration. Based on the calibration data, it is apparent that the response of the pH microsensor revealed adequate reproducibility. The mean difference of potential responses between the forward direction and the reverse direction was determined at approx. 7 mV. **Figure 5.12** shows the potential-pH relation. A linear response in the pH range of 2 - 10 pH units was obtained, and the slope of the potential vs. pH is approx. -53 mV/pH. This matches well with a Nernstian behavior, and with literature values of -52 mV/pH for antimony

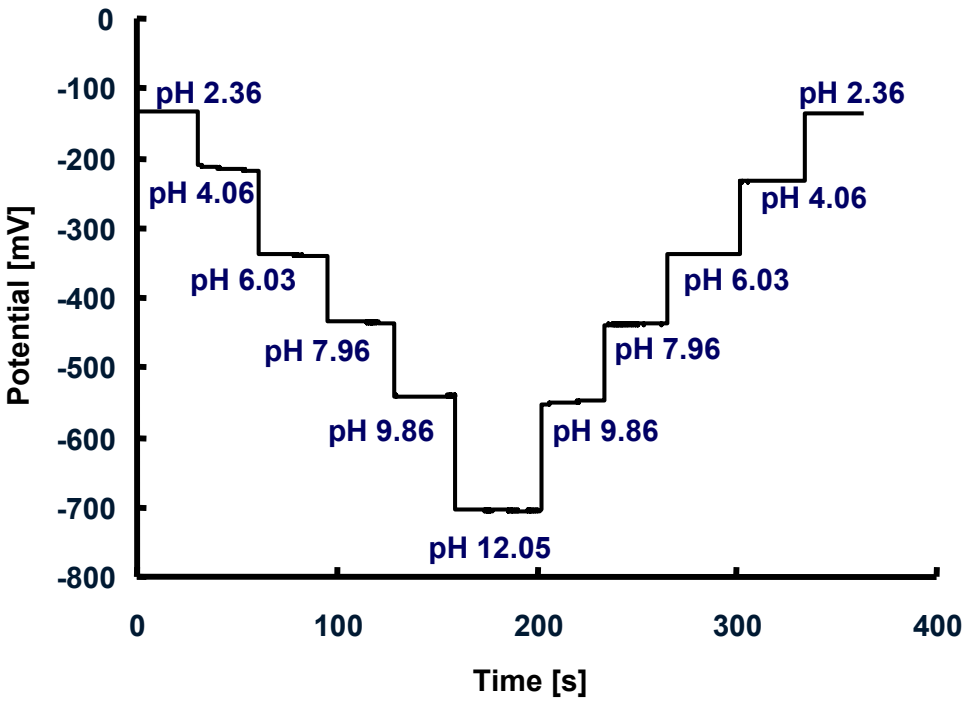

Figure 5.11 pH response of an antimony pH microsensor to a series of solutions with varying pH in the range of 2 - 12.

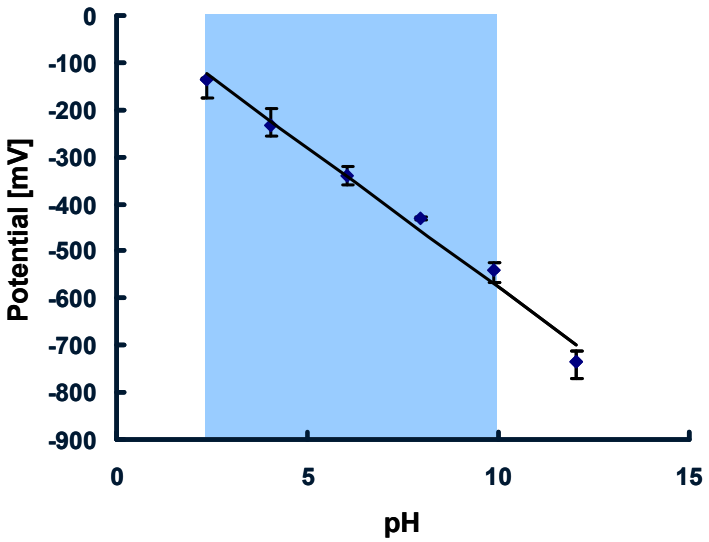

Figure 5.12 Calibration function of an antimony pH microsensor in response to a series of solutions varying the pH in the range of 2 - 12.

macroelectrodes[10]. The reason for the relatively large deviation at pH 12 is the fact that antimony oxide dissolves at high pH values forming antimonite ions (SbO_2^-) via the hydroxide ions[13,21]. In literature, a linear pH response range for antimony macroelectrodes is reported in the range of pH 2 - 11[10,12].

Furthermore, the relationship between the slope (mV/pH) of the pH response and the thickness of the deposited antimony films was investigated. The thickness of the obtained electrode layer (**Figure 5.1B**) is correlated with the width of the frame-shaped electrode, as the electrode is exposed by FIB milling (**Figure 5.1D**). For better understanding, **Figure 5.13** shows a schematic top view of the pH microsensor probe.

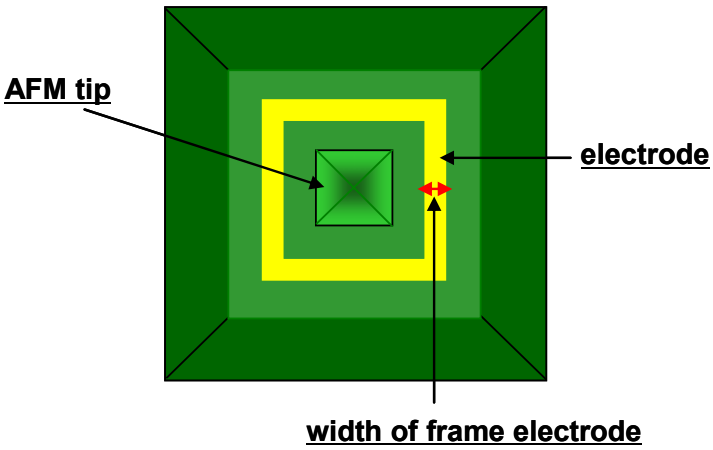

Figure 5.13 Schematic top view of the pH microsensor probe. The width of the frame-shaped pH electrode is correlated with the thickness of the deposited antimony layer.

Figure 5.14 shows the relationship between the slope (mV/pH) of the calibration curve, and the thickness of the deposited antimony. Layers were deposited in a range of 1000 – 3500 Å, and there was no significant influence on the response observed in this thickness range. In **Figure 5.15**, the variation of the slope of the pH response is shown as a percentage with respect to the thickness of the deposited antimony. There was no significant change of the slope in the calibration curves in the deposition range of 1000 – 3500 Å observed. The influence of film thickness on the response of iridium pH microsensors will be described in the next section.

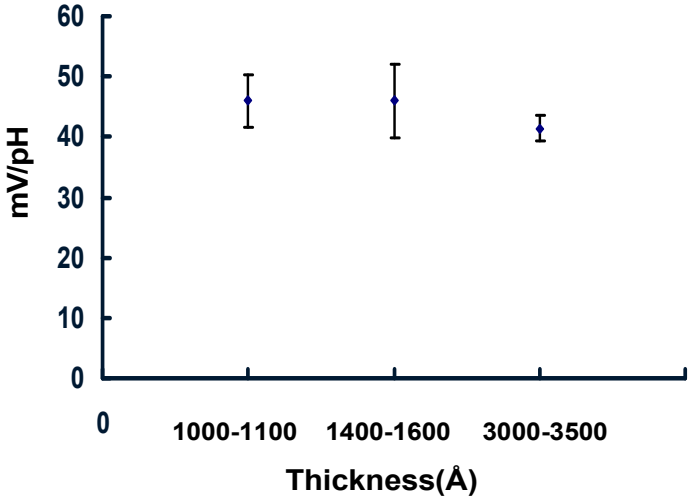

Figure 5.14 Relationship between the slope of the pH response (mV/pH) characteristics and the thickness of the antimony electrodes. Error bars correspond to the standard deviation (n = 17).

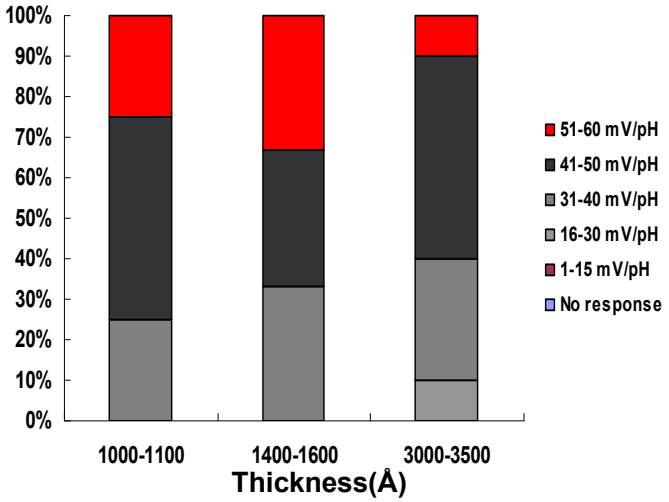

Figure 5.15 Variation of the slope of the pH response (in %) with respect to the thickness of the antimony electrode.

5.3.1.2 Iridium pH microsensor

5.3.1.2.1 pH microsensor based on anodic iridium oxide film (AIROF)

The pH response of iridium pH microsensors was determined following the procedure described in section 5.2.2. **Figure 5.16** exemplarily shows the pH response of an iridium-based pH microsensor when changing the pH in steps of four pH units in the range pH 3 - 11. Again, the pH changes were determined in both directions, i.e. from pH 3 - 11 and vice versa. As shown in **Figure 5.16**, the response was less stable and less reproducible in comparison to antimony pH microsensors; however, the slope of the potential response (approx. -63 mV/pH) was linear in the range of pH 3 – 11, and shows super-Nernstian behavior comparable to literature results (-62 − -76 mV/pH) for AIROF macroelectrodes[11-12], as shown in **Figure 5.17**.

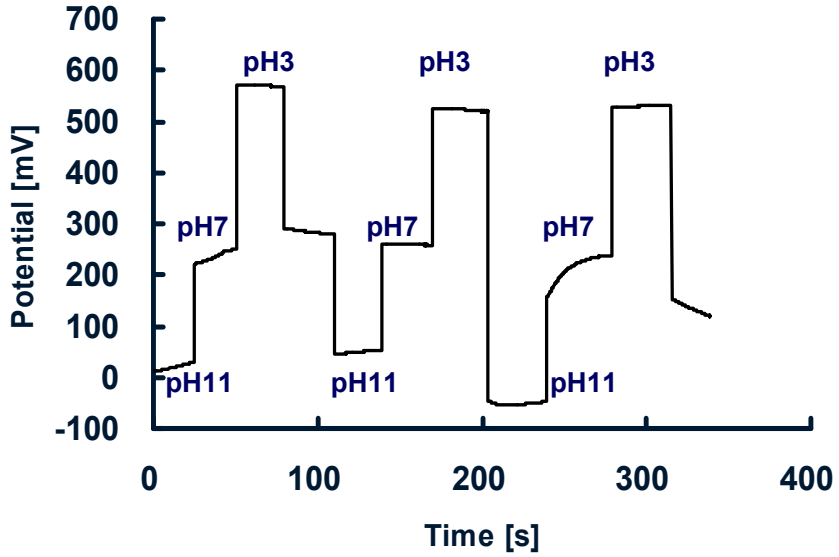

Figure 5.16 pH response of an iridium pH microsensor in solutions with different pH values raging from 3 to 11.

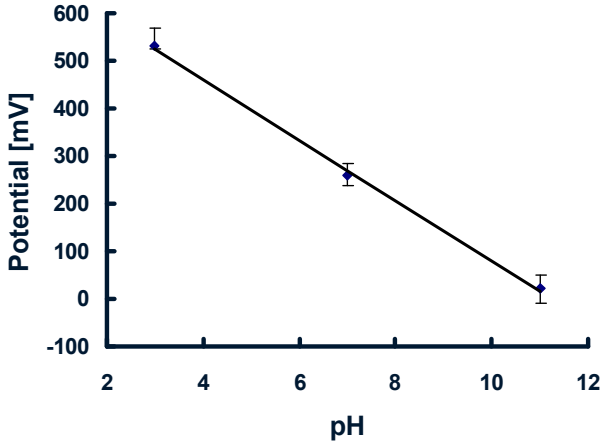

Figure 5.17 Calibration function of an iridium pH microsensor to a series of solutions in the pH range of 3 - 11.

Based on results published by Hitchman et al.[22], the insufficient stability and reproducibility is related to the low charge storage capacity of AIROF, which is correlated with the thickness of the metal oxide layer[23]. Therefore, the electrochemical oxidation process is critical to achieve a sufficiently thick layer of the pH responsive oxide layer to ensure a reproducible pH response. **Figure 5.18** shows exemplarily a cyclic voltammogram of the oxidation of the AFM tip-integrated iridium electrode. The potential of the iridium electrode was cycled between -0.25 and 1.25 V vs. SCE with a scan rate of 0.1 V s^{-1} in 0.5 M H_2SO_4. At the first couple of cycles, no oxidation peaks are visible due to the noble metal character of the iridium electrode. However, both the anodic peak (A) and cathodic peak (B), which are attributed to the redox transition reaction between Ir(III) and Ir(IV)[24] appear after a few tens of cycles, and the peak currents are increasing as the number of cycles is increased. Subsequently, an oxide layer is growing, as the net cathodic current increases vs. the net anodic current, since the

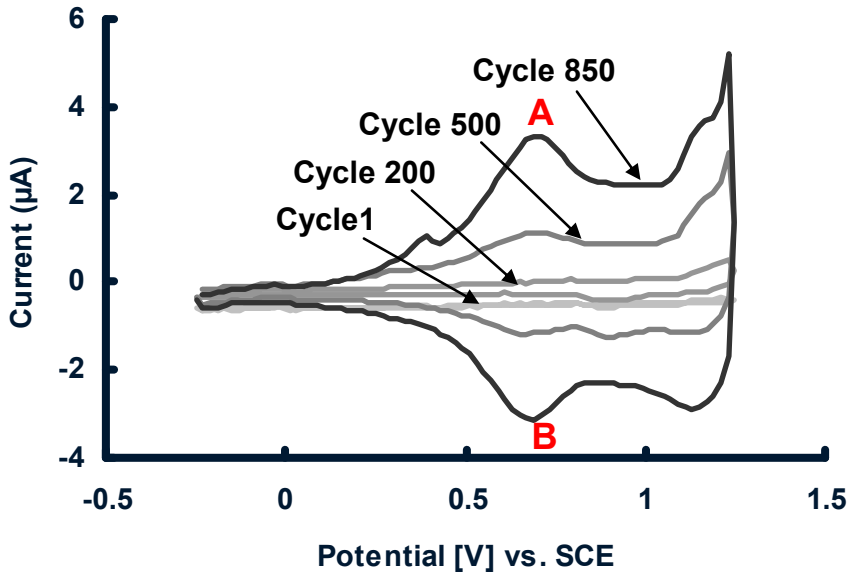

Figure 5.18 Cyclic voltammogramms recorded in 0.5 M H_2SO_4 at an iridium pH microsensor cycled 850 times between -0.25 and 1.25 V vs. SCE with 0.1 V s^{-1} scan rate.

transition reaction is becoming irreversible. **Figure 5.19** exemplarily shows the relationship between the number of oxidation cycles and the obtained pH response characteristics. For both cyclic voltammograms A and B shown in **Figure 5.19**, the potential of the iridium electrode was cycled 850 times between -0.25 and 1.25 V vs. SCE with a scan rate of 0.1 V s^{-1} in 0.5 M H_2SO_4 (only the final cycle is presented). Electrode A does show noticeable transition reaction peaks and an increase of net currents indicating the growth of oxide layer, which corresponds to the pH response. The response is shown, even though the slope of the pH response function (mV/pH) does not appear ideal. As shown in **Figure 5.19B**, the iridium pH microsensor, which does not

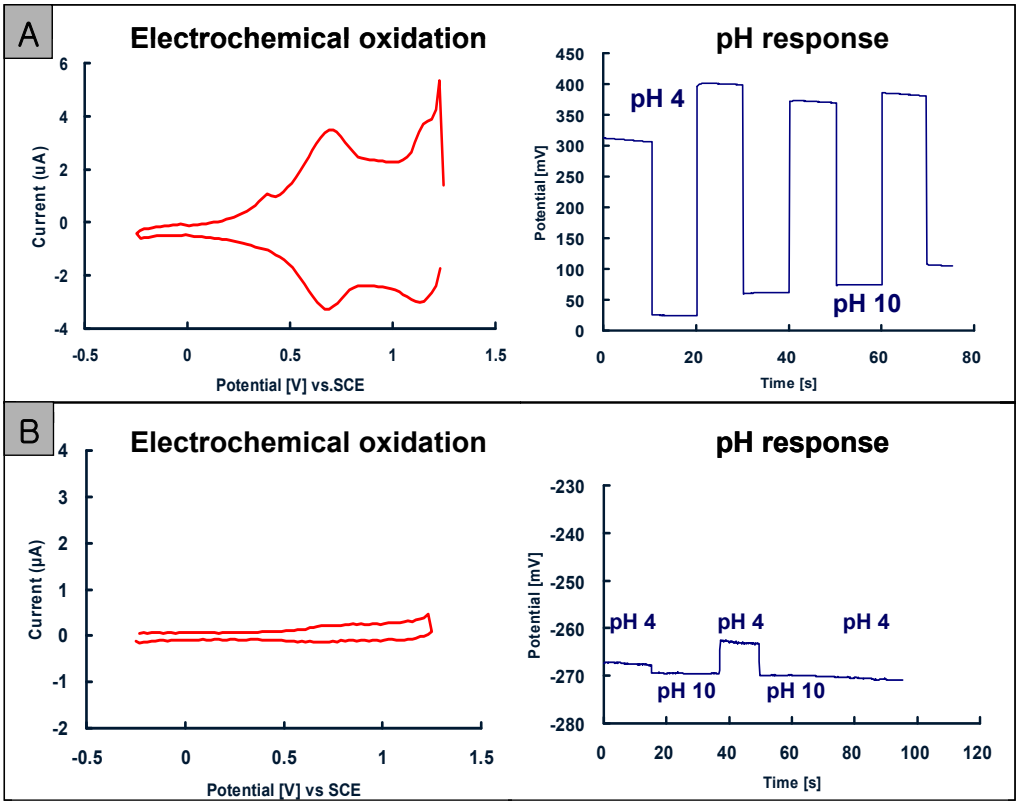

Figure 5.19 Representative relationships between the formation of an iridium oxide layer, and the obtained pH response.

have a sufficiently thick oxide layer reveals a minimal response to varying pH values. Also, the pH response is correlated with the thickness of the iridium electrode layer, as shown in **Figure 5.20** and **Figure 5.21**. From the graphs shown in these figures it is apparent that with an iridium electrode layer thickness less than 1000 Å, in most cases no response was obtained. Hence, the iridium layer needs to be thicker than approx. 3000 Å to obtain a slope of the pH response curve close to the typical value of -62 – -76 mV/pH, as reported for AIROF macroelectrodes[11]. Summarizing, there insufficient oxide layer

growth is apparent, if the deposited layers are below 3000 Å in thickness, which consequently leads to poor pH response of the iridium-based pH microsensors.

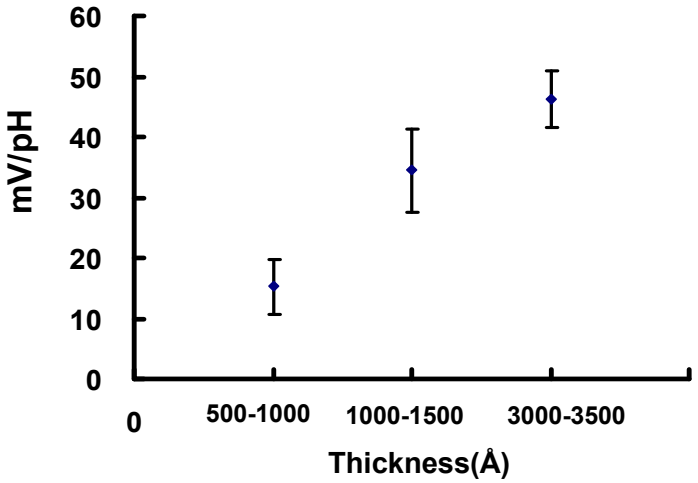

Figure 5.20 Relationship between the slope of the response curve (mV/pH), and the thickness of the sputtered iridium layer. Error bars correspond to the standard deviation with (n = 25).

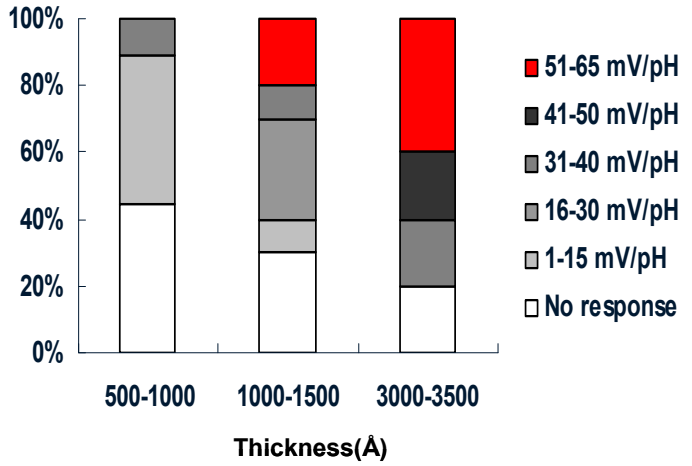

Figure 5.21 Variation of the slope of the pH response curve (in %) in relation to the thickness of the iridium electrode.

5.3.1.2.2 pH microsensors based on sputtered iridium oxide films (SIROF)

SIROF pH microsensors have also been prepared in the course of this study. SIROF is known to provide a more reproducible slope behavior (mV/pH) compared to AIROF[25]. However, the sputtering conditions are critical since they affect critical sensing characteristics including drift or redox interferences[25]. The conditions of sputtering deposition have been well established in the corresponding literature[26-27]. For test purposes, approx. 1500 Å of SIROF were deposited at a 2 x 3 mm^2 sized glass substrate using RF sputtering (PVD75 RF sputterer; power = 45 W, pressure = 7 mTorr, gas was Ar). This macroscopic electrode revealed a pH response of approx. -50 mV/pH. However, pH microsensors based on SIROF, which were prepared using the same conditions, did not respond to pH changes at all, which has to be further investigated during future studies.

5.3.2 pH imaging experiments

Attempts to demonstrate laterally resolved pH mapping were performed with pH microsensors featuring a pH response slope of at least -30 mV/pH. The set-up for pH imaging experiments was described in the experimental section 5.2.3. One of the major challenges during conducting imaging experiments was to establish a micro-sized localized pH diffusion zone at the surface of the porous substrates, which may then be spatially resolved with the AFM tip-integrated pH microsensor, as the maximum scan range is limited by the piezoelectric AFM scanner. All imaging experiments described in this section were conducted in contact mode AFM.

5.3.2.1 pH imaging using a Pt microelectrode as substrate

Unfortunately, imaging experiments at Pt microelectrodes failed due to electrical interferences between the AFM tip-integrated pH microsensor and the microelectrode substrate. If a potential pulse was applied to the microelectrode to generate protons, the potential change was directly detected by the pH microsensor. This problem was significantly reduced after electrically further isolating the microelectrode by removing the ground connection. However, perfect isolation could not be obtained, thus maintaining the electrical interferences and noise peaks during the pH measurement at the AFM tip-integrated pH microsensor at a level such that pH images could not be obtained.

5.3.2.2 pH imaging at porous membranes

5.3.2.2.1 pH imaging at a soft membrane

pH imaging experiments at soft porous membranes were performed as described in section 5.2.3, and as shown in **Figure 5.8**. A polycarbonate membrane with pores of approx. 0.2 µm in diameter was used to separate two compartments, which were filled with phosphate buffer solution each at different pH values. The upper compartment was filled with a solution of pH 10, and the lower compartment was filled with a solution of pH 2, respectively. No additional flux such as e.g. using a mechanical pump was applied, as it was observed that a slight bending of the soft membrane caused by pumping interferes with AFM imaging (i.e. loss of the deflection signal). OCP measurement was simultaneously performed during scanning the combined probe across the surface of the membrane. **Figure 5.22** shows the topographical and deflection AFM images, which

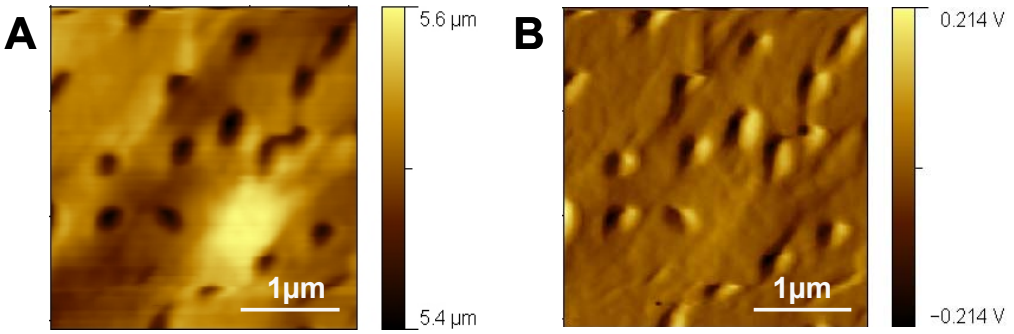

Figure 5.22 (A) Topographical and (B) deflection AFM images of a polycarbonate membrane acquired with an AFM tip with integrated antimony pH microsensor in contact mode operation. The scan rate was 0.599 line s^{-1}. The tip length of the re-shaped AFM tip was approx. 1.8 µm, and the frame electrode edge length was approx. 1.8 µm.

were recorded with a combined probe comprising a recessed pH microsensor. The combined probe could clearly resolve the topography of the membrane imaging the 0.2µm diameter sized pores. However, the simultaneously recorded OCP measurement revealed no useful pH images. I is hypothesized that the pH change was not sufficient at the orifice of the pores, as only natural diffusion through the 11 µm deep pore has occurred. Another reason may be the timing of the experiment. The lower and upper compartment have to be filled prior to starting the experiment; hence, the solutions may already mix given the density of the pores until the AFM measurements may be performed (after approx. 1 min). Therefore, in in a next set of experiments the solution was actively pumped from the lower compartment into the upper compartment to ensure forced diffusion. Also, the pH value in the lower solution should have a high acidity to significantly perturb the local pH at the orifice of the pores; otherwise, the pH change may rapidly be buffered by the solution in the upper compartment. In order to actively pump the solution, the soft membrane was replaced by a rigid silicon membrane, thus avoiding issues of bending during AFM imaging.

5.3.2.2.2 pH imaging at a rigid membrane

Prior to the imaging experiments, the potential response of the pH microsensor to additions of an acid or base solution was evaluated with a set-up shown in **Figure 5.23A**. An AFM tip-integrated iridium pH microsensor was immersed in a liquid cell filled with approx. 10 ml of 0.1 M universal buffer solution of pH 4, and 0.1 M of KOH solution was added using a pipette. Potentials were recorded in an OCP measurement. As shown in **Figure 5.23B**, additions of small volumes (approx. 40 µl) did not change the potential

measured at the pH microsensor, as the solution seemed to be buffered prior to perturbing the pH in the vicinity of the probe. An increase in volume of 100 µl of 0.1 M KOH added

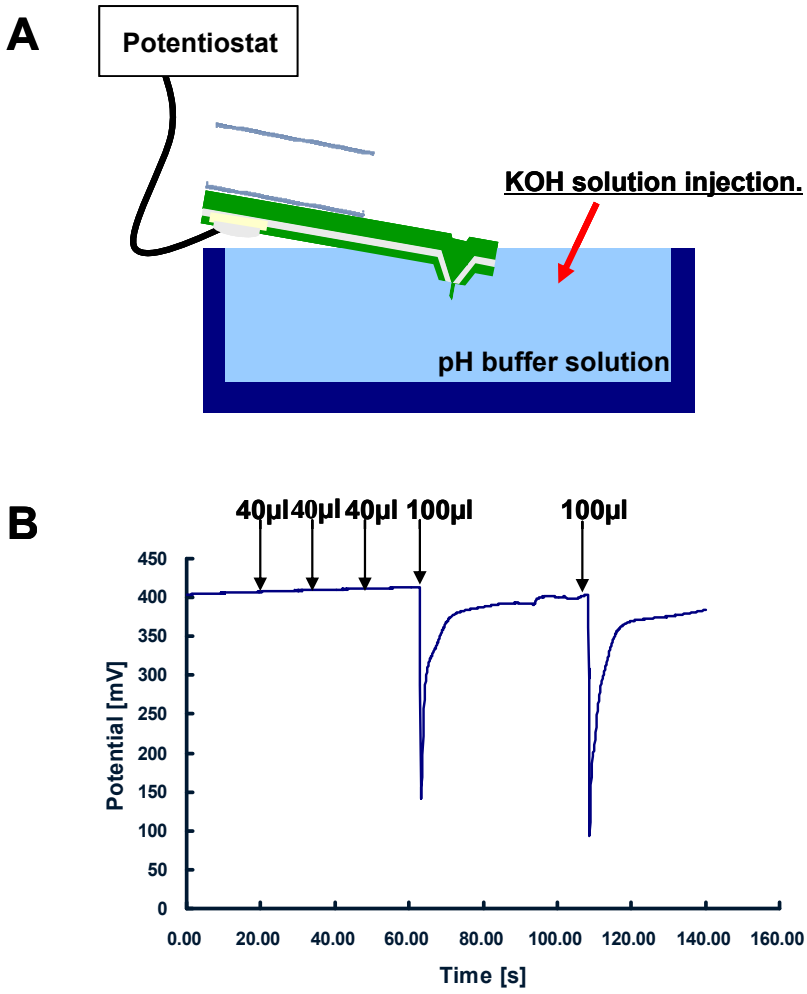

Figure 5.23 Potential response of an AFM tip-integrated iridium/iridium oxide pH microsensor. (A) Schematic: the sensor was immersed in 0.1 M universal buffer solution (pH 4), and the potential response was measured vs. Ag/AgCl in OCP measurement. (B) Induced potential response obtained as shown in A. Numbers above arrows correspond to the volume of added 0.1 M KOH solution.

to the solution induced an immediate potential drop, as shown in **Figure 5.23B**. The potential then recovered to the initial value due to the buffer activity.

A similar test was performed in the set-up designed for the imaging experiments. The antimony pH microsensor was immersed in the AFM liquid cell filled with a volume of approx. 0.8 ml of 0.1 M Tris buffer solution at pH 8. The measured potential response to the addition of 0.1 M KOH solution is shown in **Figure 5.24**. Portions of 10 µl added to solution lead to significant potential drops, as the volume of buffer solution is relatively small. Consequently, immediate potential responses of pH microsensor and buffer reaction were visualized in the AFM liquid cell.

For localized pH measurements, the AFM tip-integrated pH microsensor has to be positioned in close vicinity to the surface of the membrane. The set-up with the silicon membrane is described in section 5.2.3, and is shown in **Figure 5.8.** In order to map the local pH change near the pores (diameter approx. 15 µm), the pH microsensor was positioned above the center a pore. **Figure 5.25** shows a schematic and an

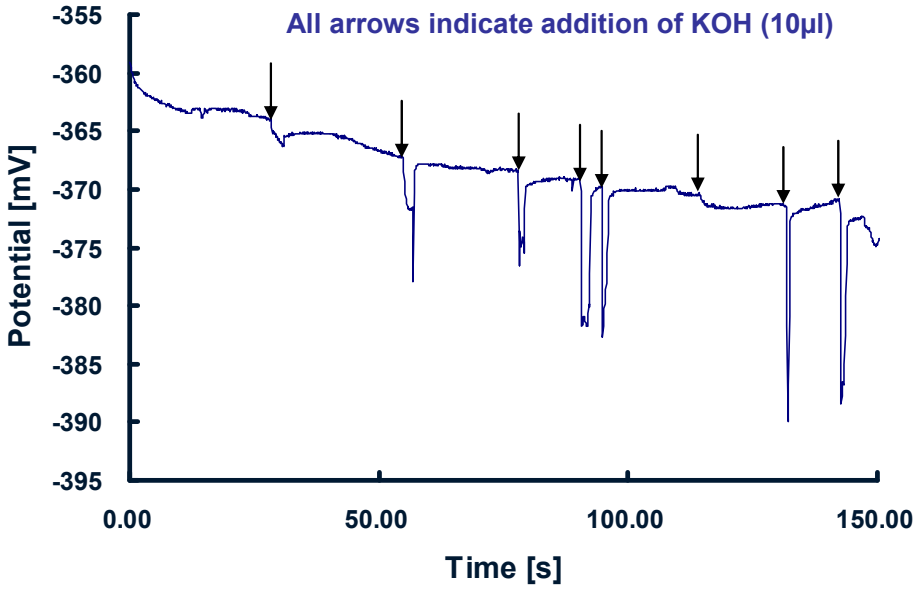

Figure 5.24 OCP measurement using an AFM tip-integrated antimony pH microsensor. The sensor was immersed in 0.1 M Tris buffer solution (pH 8) and OCP was measured vs. Ag/AgCl. Arrows correspond to addition of 10 µl of 0.1 M KOH increments.

optical image of a silicon membrane with an array of pores (diameter approx. 15 µm diameter). The silicon membrane was cleaned in piranha solution (H_2SO_4 from Fisher Scientific, Pittsburgh, PA; 30% H_2O_2 from JT Baker, Phillipsburg, NJ; ratio 4:1) for 10 min prior to the imaging experiments, and the presence of open pores was confirmed by light penetration using an optical microscope, as show in **Figure 5.25B**.

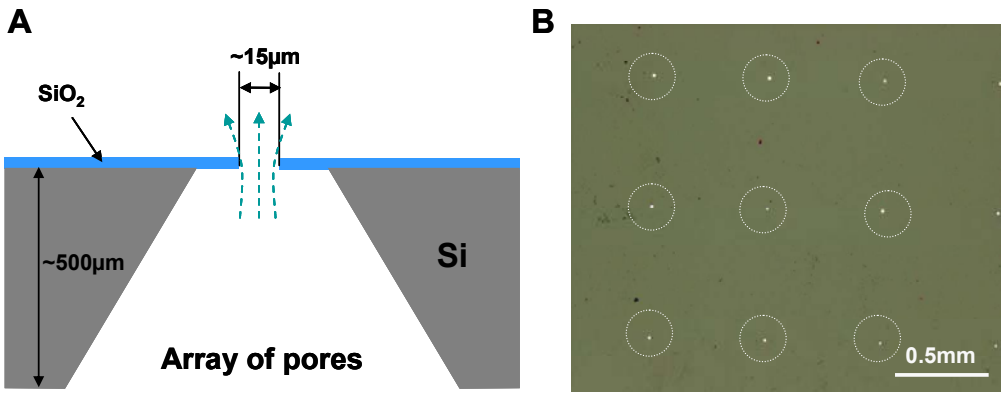

Figure 5.25 Silicon membrane with an array of approx. 15 µm diameter pores. (A) Schematic illustration of cross-sectional view of a pore. (B) Optical image showing the front view of the pore array with light penetrating through pores (encircled).

For combined topography-pH mapping experiments, the AFM liquid cell was filled with 0.1M Tris buffer solution (pH 8) in the upper compartment, and separated with the porous silicon membrane from the lower compartment, which was filled with 0.1 M HCl or 0.1 M KOH solution, respectively. The AFM tip-integrated antimony pH microsensor was positioned above one of the pores, which was randomly selected after an AFM image of the membrane surface was recorded. Either 0.1 M HCl or 0.1 M KOH solution was then pumped into the upper compartment, and the OCP was measured against AgQRE, as shown in **Figure 5.26**. The measured potential response once the tip was positioned above a pore is shown in **Figure 5.27**. The pumping rate was 12.8 µl s^{-1}, which corresponds to an estimated flow of 0.045 µl s^{-1} through a single pore considering a total number of 280 pores assuming the same flow rate through all pores.

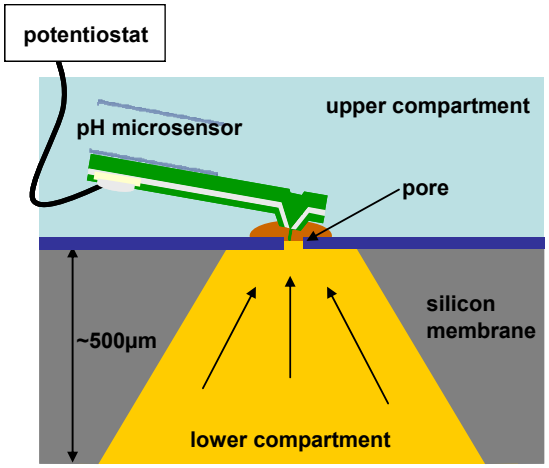

Figure 5.26 Schematic of an antimony pH microsensor positioned above an individual pore. Either acidic or alkaline solution was pumped into the upper compartment, which was filled with 0.1 M Tris buffer solution (pH 8).

The arrows in the corresponding figures indicate the start of the experiment when the solution is pumped through. In **Figure 5.27A**, a potential curve is shown corresponding to the experiment where 0.1 M HCl was pumped through the pores. An increase in potential is observed due to the local change in pH in the vicinity of the pore. In **Figure 5.27B**, the potential curve represents an experiment where 0.1 M KOH alkaline solution is pumped through the pore, and a decrease in potential is observed. For both experiments, a slow potential change was observed for approx. 10 - 20 s once the pump was started; then, a significant potential change occurred. The slow change at the beginning of the

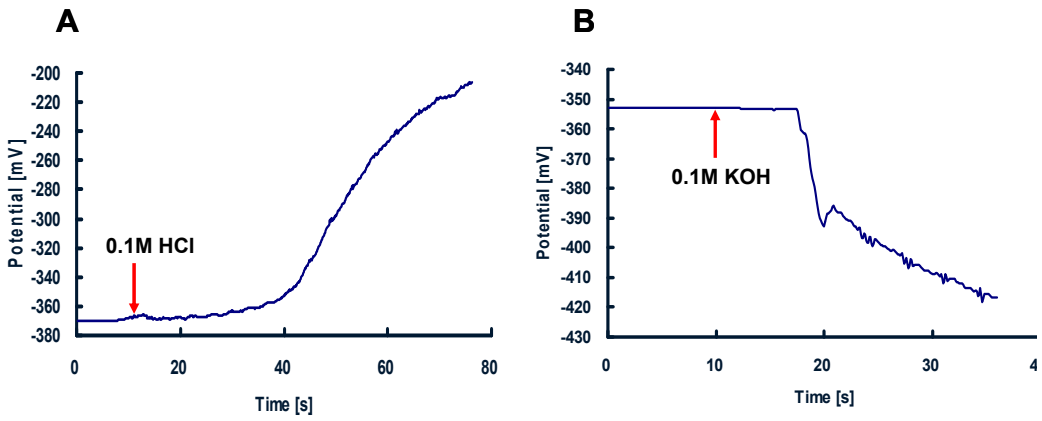

Figure 5.27 Potential response measured at an AFM tip-integrated antimony pH microsensor. The antimony pH microsensor was positioned above an individual pore, and 0.1 M HCl solution was pumped through the pore with rate of 12.8 µl s^{-1}. A) 0.1 M HCl and B) 0.1 M KOH solution was pumped into upper compartment, which was filled with 0.1 M Tris buffer solution (pH 8). The potential was measured vs. AgQRE.

pumping may be related to the fact that the solutions from the upper and lower compartment are mixed inside the pore prior to pumping the solution. Secondly, the local buffer reaction rate near the pore is rapid in the beginning, and becomes significantly slower as solution is continuously added. This may be related to the change of local buffer capacity. The buffer capacity (β) is defined as the quantity of strong acid or base that must be added to change the pH of one liter of solution by one pH unit, and numerically expressed in **Equation 5.2**[28].

$$\beta = -\frac{dn}{d(pH)} = 2.303\left(\frac{K_w}{[H^+]} + [H^+] + \frac{C_{buf} K_a [H^+]}{(K_a + [H^+])^2}\right) \qquad \text{Equation 5.2}$$

Here, n is the number of equivalents of added strong base, K_w is the dissociation constant of water, K_a is the dissociation constant of the acid, and C_{buf} is the concentration of buffer solution. From this equation, the change of buffer capacity for the 0.1 M Tris buffer solution depending on its pH values may be calculated, as depicted in **Figure 5.28**. The buffer capacity has a maximum at approx. pH 8; however, a sharp decrease is observed as the pH is changed to lower and higher values. Based on these considerations it is evident that the slow potential response at the beginning of pumping shown in **Figure 5.27** may be related to the location of the maximum buffer capacity, and the significant change in

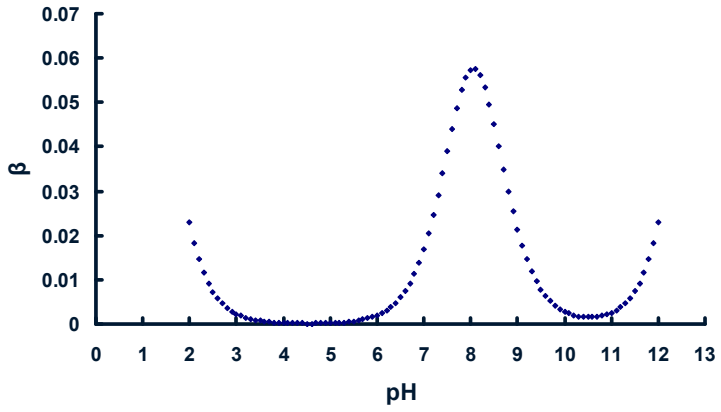

Figure 5.28 Relationship between buffer capacity (β) and pH value in 0.1 M Tris buffer solution.

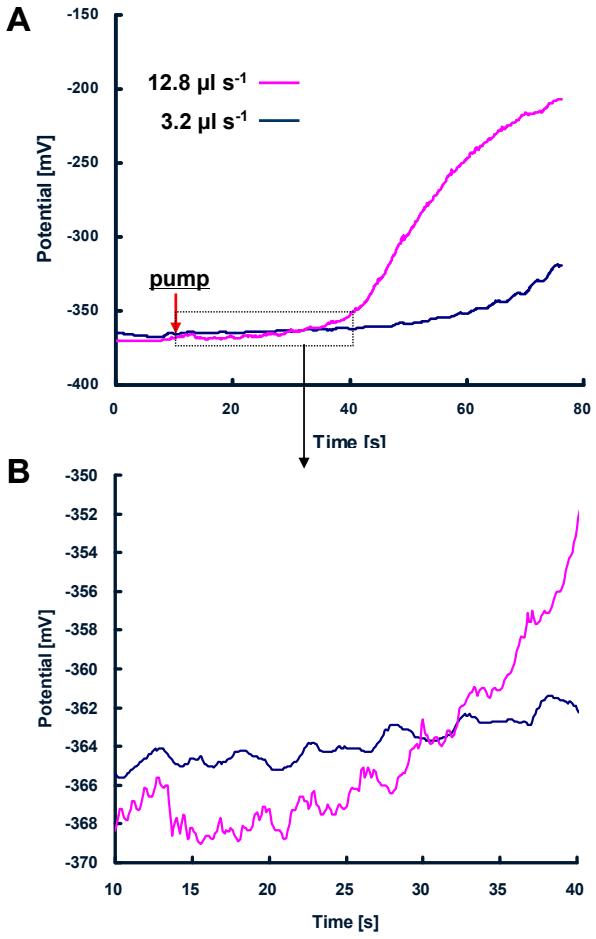

Figure 5.29 Potential response recorded at an antimony pH microsensor in dependence of the pump rate. (A) The antimony pH microsensor was located above an individual pore, and 0.1 M HCl solution was pumped through the pore at a rate of 12.8 µl s^{-1} and 3.2 µl s^{-1}, respectively. The upper compartment was filled with 0.1 M Tris buffer (pH 8) and the potential was measured vs. AgQRE. The arrow indicates the starting point of pumping solution. (B) gives a magnified view of the boxed area in (A).

potential response may be caused by the sharply decreased buffer capacity as the solution is continuously added in close vicinity to the pores. In **Figure 5.29**, the potential response

in respect to the different pumping rates is shown for 0.1 M HCl in the lower compartment. Hence, a faster pumping speed results in a more significant potential response. These experiments fundamentally demonstrate the capability of localized pH measurements using AFM tip-integrated potentiometric sensors, although in this thesis only a sequential measurement of topography and stationary measurements of pH is shown. However, such studies confirm the capability that the local proton concentration and/or the rate of local proton gradients or consumption of protons at defined of localized surface reactions may be studied with the developed bifunctional SFM-pH probes.

5.4 Final remarks

AFM tip-integrated antimony or iridium pH microsensors were developed an fabricated in this thesis. Their potential response to pH changes was calibrated via OCP measurements using a flow injection system. Antimony pH microsensors revealed a linear response of -53 mV/pH. Iridium pH microsensors also reveal promising results as providing a linear response with a slope of -63 mV/pH. However, the potential response was typically less stable and less reproducible compared to antimony pH microsensors. Furthermore, it was shown that the pH response characteristics of iridium pH microsensors depend on the thickness of the iridium electrode layer. A stable response may only be obtained at a minimum thickness of 3000 Å for the Ir layer. Due to fabrication challenges resulting from intrinsic stress of the iridium layer, the focus was shifted to AFM tip-integrated antimony electrodes. However, iridium pH microsensor may be improved by optimizing the oxidation process, which is a critical step determining the characteristic of AIROF.

The potential response of antimony pH microsensors was evaluated using an AFM liquid cell. The pH microsensors revealed immediate response to the addition of acidic or alkaline solutions. Also, the capability of pH microsensor to determine localized pH values was demonstrated using a two-compartment AFM liquid cell separated by a porous silicon membrane. The localized pH change was measured in sequence to topographical imaging rather than simultaneous experiments during these first studies, after positioning the combined probe above an individual pore. For simultaneous topographical and pH mapping new test samples with a controlled steady-state-like proton or hydroxide diffusion area have to be established in lieu of the transient pH changes, which were achieved in the present set-up. One critical aspect is the dimension and distribution of the pores across the silicon membrane, as the total scan size of the piezoelectric AFM scanner is limited to 90 μm. In addition, the concentration of the buffered solution in the upper compartment, the concentration of acidic or alkaline solution in the lower compartment, and the pumping rate need to be tightly controlled.

5.5 References

1. H. Galster, pH measurement-Fundamentals, Methods, Applications, Instruments, VCH publishers,; New York. 1991.

2. A. Bastos, O. Karavai, M. Zheludkevich, K. Yasakau, M. Ferreira, Localised Measurements of pH and Dissolved Oxygen as Complements to SVET in the Investigation of Corrosion at Defects in Coated Aluminum Alloy. *Electroanalysis* 2010, *22*. 2009-2016.

3. J. C. Chen, M. Chesler, pH transients evoked by excitatory synaptic transmission are increased by inhibition of extracellular carbonic anhydrase. *Proceedings of the National Academy of Sciences of the United States of America* 1992, *89*. 7786-7790.

4. R. J. Gillies, N. Raghunand, M. L. Garcia-Martin, R. A. Gatenby, pH imaging. *Engineering in Medicine and Biology Magazine, IEEE* 2004, *23*. 57-64.

5. T. Honda, K. Murase, T. Hirato, Y. Awakura, pH measurement in the vicinity of a cathode evolving hydrogen gas using an antimony microelectrode. *Journal of Applied Electrochemistry* 1998, *28*. 617-622.

6. V. Kalyan, L. K. Melissa, J. K. Martin, Dynamics of Muscle Glycogenolysis Modeled with pH Time Course Computation and pH-Dependent Reaction Equilibria and Enzyme Kinetics. *Biophysical Journal* 2006, *91*. 1264.

7. L. Niu, Y. Yin, W. Guo, M. Lu, R. Qin, S. Chen, Application of scanning electrochemical microscope in the study of corrosion of metals. *Journal of Materials Science* 2009, *44*. 4511-4521.

8. J. E. Trosko, R. J. Ruch, Cell-cell communication in carcinogenesis. *Frontiers in Bioscience* 1998, *3*. 208-236.

9. A. Fog, R. P. Buck, Electronic semiconducting oxides as pH sensors. *Sensors and Actuators* 1984, *5*. 137-146.

10. S. Glab, G. Edwall, P.-A. Jöngren, F. Ingman, Effects of some complex-forming ligands on the potential of antimony pH-sensors. *Talanta* 1981, *28*. 301-311.

11. S. Glab, A. Hulanicki, G. Edwall, F. Ingman, Metal-Metal Oxide and Metal Oxide Electrodes as pH Sensors. *Criticla Reviews In Analytical Chemistry* 1989, *21*. 29-47.

12. P. Kurzweil, Metal Oxides and Ion-Exchanging Surfaces as pH Sensors in Liquids: State-of-the-Art and Outlook. *Sensors (14248220)* 2009, *9*. 4955-4985.

13. J. T. Stock, W. C. Purdy, L. M. Garcia, The Antimony-Antimony Oxide Electrode. *Chemical Reviews* 1958, *58*. 611-626.

14. E. Ammann, C. Beuret, P. F. Indermühle, R. Kötz, N. F. de Rooij, H. Siegenthaler, Local pH-controlled reactivity investigations by thin-layer scanning tunnelling microscopy. *Electrochimica Acta* 2001, *47*. 327-334.

15. E. E.-D. M. El-Giar, D. O. Wipf, Microparticle-based iridium oxide ultramicroelectrodes for pH sensing and imaging. *Journal of Electroanalytical Chemistry* 2007, *609*. 147-154.

16. M. Etienne, P. Dierkes, T. Erichsen, W. Schuhmann, I. Fritsch, Constant-Distance Mode Scanning Potentiometry. High Resolution pH Measurements in Three-Dimensions. *Electroanalysis* 2007, *19*. 318-323.

17. B. R. Horrocks, M. V. Mirkin, D. T. Pierce, A. J. Bard, G. Nagy, K. Toth, Scanning electrochemical microscopy. 19. Ion-selective potentiometric microscopy. *Analytical Chemistry* 1993, *65*. 1213-1224.

18. B. Liu, W. Cheng, S. A. Rotenberg, M. V. Mirkin, Scanning electrochemical microscopy of living cells: Part 2. Imaging redox and acid/basic reactivities. *Journal of Electroanalytical Chemistry* 2001, *500*. 590-597.

19. D. O. Wipf, F. Ge, T. W. Spaine, J. E. Baur, Microscopic Measurement of pH with Iridium Oxide Microelectrodes. *Analytical Chemistry* 2000, *72*. 4921-4927.

20. M. Wang, S. Yao, Carbonate-Melt Oxidized Iridium Wire for pH Sensing. *Electroanalysis* 2003, *15*. 1606-1615.

21. L. R. Parks, H. C. Beard, The Theoretical Limitations of the Stick Antimony Electrode. *The Journal of Physical Chemistry* 1933, *37*. 822-823.

22. M. L. Hitchman, S. Ramanathan, Evaluation of iridium oxide electrodes formed by potential cycling as pH probes. *Analyst* 1988, *113*. 35-39.

23. L. D. Burke, J. K. Mulcahy, D. P. Whelan, Preparation of an oxidized iridium electrode and the variation of its potential with pH. *Journal of Electroanalytical Chemistry* 1984, *163*. 117-128.

24. D. A. J. Rand, R. Woods, Cyclic voltammetric studies on iridium electrodes in sulphuric acid solutions: Nature of oxygen layer and metal dissolution. *Journal of Electroanalytical Chemistry* 1974, *55*. 375-381.

25. S. Yao, M. Wang, M. Madou, A pH Electrode Based on Melt-Oxidized Iridium Oxide. *Journal of The Electrochemical Society* 2001, *148*. H29-H36.

26. K. G. Kreider, M. J. Tarlov, J. P. Cline, Sputtered thin-film pH electrodes of platinum, palladium, ruthenium, and iridium oxides. *Sensors and Actuators B: Chemical* 1995, *28*. 167-172.

27. M. J. Tarlov, S. Semancik, K. G. Kreider, Mechanistic and response studies of iridium oxide pH sensors. *Sensors and Actuators B: Chemical* 1990, *1*. 293-297.

28. A. Hulanicki, Reactions of Acids and Bases In Analytical Chemistry. New York, NY: Ellis Horowood Limited. 1987.

6 Conclusions and outlook

The main goal of this thesis was to develop improved processing strategies for combined AFM-SECM probes enabling high resolution topographical and electrochemical imaging, and to implement novel analytical functionality into combined AFM-SECM probes. A main aspect of this effort was dedicated to improve the reproducibility in fabricating AFM-SECM probes and maximizing the insulation properties for establishing a distinct and localized electroactive area. Furthermore, the selected fabrication processes need to ensure straight cantilevers for enabling appropriate AFM imaging functionality, and small RG values for optimized electrochemical resolution. Moreover, a semi-batch fabrication process for tip-integrated disk nanoelectrodes enabling high resolution AFM-SECM imaging was developed. Finally, combined AFM-SECM probes with tip-integrated pH microsensors based on solid-state materials were developed and for the first time applied for high resolution pH measurements.

The fabrication procedures were optimized in respect to the metallization step and the insulation process for AFM-SECM probes with recessed frame sub-micrometer electrodes. A stainless steel shadow mask was designed and fabricated using IR laser micromachining for the metallization step. This enabled the structured deposition of the metal layer serving as the electrode, and as a conductive path for the electrochemical signal instead of coating the entire probe including the cantilever chip. Consequently, potential electrical leakage currents could be significantly reduced, as the conductive

areas are reduced to the signal pathways and the electroactive surface rather than the entire chip. For an improved electrical insulation of AFM-SECM probes, sandwiched layers of PECVD-deposited Si_xN_y and SiO_2, and plasma-deposited PFE films were implemented, applied, and tested. Resulting, AFM-SECM probes with straight cantilevers and excellent insulation characteristics could be reproducibly obtained utilizing optimized sandwiched layers of PECVD Si_xN_y and SiO_2 insulation. The final insulation thickness was in range of 0.7 - 1.0 μm. For testing the functionality, combined topographical and electrochemical imaging experiments were performed with these bifunctional probes at a Pt-SiO_2 micropatterned substrate serving as a model sample. It was shown that the obtained images are in excellent agreement with the SECM theory. In addition, PFE thin films were implemented for the first time serving as a novel insulation material for AFM-SECM probes. The electrochemical characterization of PFE-insulated AFM-SECM probes was performed via cyclic voltammetry, and revealed excellent insulating properties at a thickness of approx. 400 nm. Finally, it was shown that improved electrical insulation and adhesion of the insulation layers requires optimizing the surface treatment strategy prior to the insulation step.

The disk nanoelectrodes integrated in AFM probes were designed to have radii in the range of 50 – 100 nm for high resolution combined AFM-SECM measurements. This development was achieved by a semi batch-fabrication process so that time and cost for the fabrication could be reduced. Simulation studies were performed for the electrochemical characteristics of AFM tip-integrated disk nanoelectrodes. This simulations help to understand the fabrication requirements in respect to the physical parameters of these microfabricated devices. Moreover, it provides a better understanding

of the electrochemical properties of nanometer-sized AFM-SECM tips and insight in experimental aspects for improving tip milling procedures. The simulation dealt with influence of RG value on steady-state current, approach curves and line scans of modeled substrate. From the simulation results, a small RG value approaching unity is advantageous showing increased steady-state current when the electrode is close to the tip apex. To translate the theoretically obtained results, a cylindrical hole as a mold of nanoelectrode needs to be formed very close to the apex of the pyramidal shape of the desired probe, which was realized by deliberate FIB milling process. The fabricated AFM-SECM probes were electrochemically characterized by CV and approach curve were recorded, which were in good agreement with the simulation results. In addition, simultaneous topographical and electrochemical imaging was performed with model samples consisting of patterns of conductive and insulating features. In this imaging experiment, high resolution of the electrochemical imaging capability was demonstrated by imaging an insulating dirt particle on a Au substrate and by imaging regular patterns of conductive and insulating features with a line width of approx. 300 - 400 nm and 600 nm, respectively. It is expected that the lateral resolution can be further improved by reducing the radii of the electrode, which translates to milling a hole with a smaller diameters. However, the reshaping of the insulating AFM tip, which requires deliberated FIB milling since the length of the tip determines the working distance is a critical step.

Finally, AFM tip-integrated potentiometric sensors based on sub-micro solid-state electrodes was designed, fabricated and tested as imaging pH microsensors. Antimony and iridium oxide films were used as pH sensitive materials, as these materials could be integrated in AFM probes by standard cleanroom processes. For the fabricated antimony

and iridium pH microsensor, the pH response was characterized. Antimony-based pH microsensors showed linear response of -53 mV/pH. However, iridium-based pH microsensors showed less stable and less reproducible pH responses in comparison to antimony pH microsensor. The sputtering of iridium films and electrochemical oxidation process to form anodic iridium oxide films needs to be further studied and optimized. The potential responses of the pH microsensors were also evaluated in an AFM liquid cell and a fast response to the addition of acidic or alkaline solutions was observed. In addition, the capability of pH microsensor to measure localized pH was demonstrated with a set-up using two compartments, where the compartments were separated by a silicon membrane. The localized pH measurement so far could only be performed in sequential steps. First the topography was recorded and then the combined probe was deliberately stopped over the orifice of a pore through which consecutively acidic or alkaline solution was pumped through. However, the capability of simultaneous topographical and 2D pH mapping could not be demonstrated, yet. It is expected that a controlled steady-state like proton or hydroxide diffusion area has to be established as a model sample instead of the transient pH changes, which were investigated in the described experiments. In addition, the parameters include size of pores, concentration of the buffered solution in the upper compartment, concentration of acidic or alkaline solution in the lower compartment and the pumping rate need to be carefully controlled.